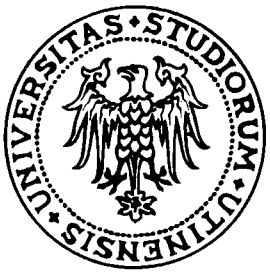

UNIVERSITÁ DEGLI STUDI DI UDINE

Dottorato di Ricerca in Ingegneria Industriale e dell'Informazione

Dipartimento Politecnico di Ingegneria e Architettura

Stefano VENICA

Modeling and Simulation of Graphene–Based Devices for RF Applications

Advisor:

Prof. Francesco DRIUSSI

Co-advisor

Prof. Pierpaolo PALESTRI

External reviewers:

Prof. Gianluca FIORI
Prof. Mirko POLJAK

Ph.D. Thesis

Ciclo XXIX

Abstract

The first experimental preparation and characterization of a monolayer graphene in 2004 has triggered the interest of the scientific community because of the peculiar graphene properties (e.g. structural, electrical). The two–dimensional (2D) structure with monoatomic thickness and the incredible high carrier mobility of graphene have created widespread expectations that it could be the perfect material for future nanoelectronic devices. Graphene–Field–Effect–Transistors (GFETs) have been extensively investigated, but the absence of an energy bandgap in monolayer graphene (which heavily hampers its use in digital electronics which requires high I_{ON}/I_{OFF} ratios) leads to non–saturated output characteristics, hence in poor intrinsic voltage gains. For this reason, vertical graphene–based architectures, as the Graphene–Base–Transistor (GBT), have been proposed as alternative solution for THz RF electronics. Unluckily, the technological difficulties related to the fabrication processes have slowed–down the improvement of these transistor concepts. Because of the early stage of the technology, the modeling and simulations play a major role, in order to understand the physical mechanisms involved in the graphene–based device operation and to provide useful guidelines to support the design of optimized devices.
This thesis is positioned in this framework, and it is focused on the development of physics–based models and simulators for GFETs and GBTs, with the aim to support the design of fast transistors and to reliably predict the device performance limits. Concerning GFETs, in this work we mostly focused on the drawbacks related to the series resistances associated to the metal/graphene contact, both from modeling and experimental perspectives. For GBTs, instead, we developed an electrical model and a single–particle Monte Carlo simulator able to predict the RF performance and the impact of electron scattering on the device operation, respectively. The developed simulators represent an important set of tools to support future investigations on the use in electronic devices of graphene and other 2D materials, e.g. semiconducting transition metal dichalcogenides, which show properties that can overcome the limits of graphene.

Contents

1 Introduction **1**

2 Graphene in Nanoelectronics **5**
2.1 Graphene . . . 5
2.1.1 Crystal and reciprocal lattice . . . 5
2.1.2 Band structure and energy-dispersion relation . . . 8
2.1.3 Density of states and carrier concentration . . . 10
2.1.4 Main characteristics of graphene . . . 11
2.2 State–of–the–art of graphene–based devices . . . 12
2.2.1 Graphene–Field–Effect–Transistor . . . 12
2.2.2 Vertical transport graphene transistors . . . 13

3 The Metal/Graphene Contact in Graphene–Field–Effect–Transistors **15**
3.1 Introduction . . . 15
3.2 Monte Carlo simulator for GFETs . . . 16
3.3 Modeling of electrostatic doping of source and drain regions in GFETs . . . 20
3.3.1 Modeling of the metal/graphene interface . . . 21
3.3.2 GFETs with electrostatic doping of graphene . . . 23
3.4 Modeling of the series resistances . . . 27
3.5 Characterization of metal/graphene contact resistance . . . 32
3.5.1 End–contact method applied on TLM structures . . . 32
3.5.2 TLM samples . . . 35
3.5.3 Measurement results and failure of the transmission line model . . . 36
3.6 Conclusion . . . 40

4 Physics–Based Models for the Graphene–Base–Transistor **43**
4.1 Introduction . . . 43
4.2 GBT structure and operation . . . 43
4.3 Electrical model for GBT devices . . . 45
4.3.1 Modeling of the GBT with silicon emitter . . . 45
4.3.2 Modeling of the GBT with metal emitter . . . 49
4.3.3 Comparison between GBTs with silicon and metal emitter . . . 50
4.3.4 Modeling of the GBT under high current regime . . . 52
4.3.5 Impact of high current effects on GBT characteristics . . . 56
4.3.6 Impact of the series resistance on the unity power gain of the GBT . . . 60
4.3.7 Verification of the tunneling model . . . 61
4.4 Compact model for the GBT . . . 63
4.5 Monte Carlo simulator for the electron transport through the GBT . . . 64
4.5.1 Scattering model for the dielectric materials . . . 66

4.5.2 Electron transport in the GBT 68
4.6 Optimization of GBT devices exploiting realistic dielectric materials 71
4.7 Comparison with experiments 74
4.7.1 First GBT prototypes 75
4.7.2 GBT devices with bilayer EBI 78
4.8 Conclusion 85

Conclusion and Future Work **87**

Bibliography **91**

Publications of the Author **103**

Chapter 1

Introduction

For decades, the market of Integrated Circuits (ICs), e.g. microprocessors and memory elements, has been guided by the well—known *Moore's law*, which predicts the doubling of the number of transistors per chip every 18 month with a simultaneous exponential decrease of the prices of the single transistor [1]. The key factor of this fast evolution has been the continuous shrink of the geometrical dimension of the Metal Oxide Semiconductor Field Effect Transistor (MOSFET), at the base of the Complementary–MOS (CMOS) technology. In the recent years, the extreme reduction of the MOSFETs size has led to a strong enhancement of the short channel effects [2, 3], which results in a significant reduction of the device performance, mostly due to the quantum tunneling leakage between the source and drain regions of the device. Consequently, the transistor performance must be supported by alternative scaling strategies, like material and structure engineering, in addition to the simple geometrical shrink. Since the state–of–the–art IC technology is still based on Silicon (Si), a first step in this direction has been the introduction of the strain in the Si crystal to enhance the carrier mobility in the channel [3, 4]. However, because of the limits of the carrier mobility increase for large strain levels, new strategies have been later introduced, e.g. the use of high–k material as top dielectric that allows the reduction of the equivalent oxide thickness [3, 5] and the further scaling of the device. These approaches to further improve the CMOS technology are internationally recognized part of the *More Moore* domain. Additional and alternative strategies, that are not related to the dimension scaling and are based on the diversification of the integrated circuit functionalities, are known as *More than Moore*, which includes technologies combining digital electronics with analog Radio Frequency (RF)/high–voltage modulus, sensors, biochips, etc. In the More than Moore domain, the possibility of alternative FET channel materials featuring high carrier mobility, as additional semiconductor compounds (e.g. GaAs, InP, GaN) or two dimensional (2D) materials, is largely explored.

In particular, the interest of nanoelectronic community on 2D materials has started in 2004, when two works regarding the realization of graphene–based devices have been published [6, 7]. From the beginning, the incredibly high carrier mobility and the two–dimensional nature of the monolayer graphene have created the expectation that it could be the perfect channel material for high speed FETs [6, 8, 9, 10]. Indeed, in short times, the scientific community was able to develop *Graphene–FETs* (*GFETs*) with cutoff frequencies above the GHz limit [11] and comparable to that ones obtained by well–established technologies. Despite its rapid development and the amazing properties, graphene presents strong and impacting drawbacks, and the absence of an energy bandgap is the most limiting one. First, the missing bandgap strictly prevents the proper switch–off of the graphene channel, making GFETs not suitable for digital logic circuits, because of the resulting large leakage current during the off–state. Second, it results in the ambipolar behavior of graphene, that causes the non–saturated output characteristics during the on–state

and a strong decay of some analog figures of merit, as the intrinsic voltage gain of the device [12, 13]. Last but not least, the series resistance associated to the metal/graphene contact at the Source (S) and Drain (D) terminals of GFETs are currently very large if compared to those achievable in conventional MOSFETs [14]. Hence, the optimization of the metal/grapehne contact represents, nowadays, a fundamental issue for the GFETs technology [15, 16].
In this framework, different strategies are explored to solve these severe issues. As an example, the possibility to form an energy bandgap by the fabrication of narrow graphene nanoribbons [17, 18, 19] or the use of bilayer graphene [20, 21] represent possible solutions to improve the GFET operation. Alternatively, the investigation of new device architectures not prone to the lack of the energy bandgap may be a viable way for graphene–based electronics. In this latter scenario, vertical graphene device concepts have risen special interest in the last years; in particular, the *Graphene–Base–Transistor* (*GBT*, [22]), suited for RF application, shows very high–performance potential, at least at simulation level [23, 24, 25, 26].
In this context, the modeling and simulation of graphene–based devices are of fundamental importance, in order to support the fabrication of the experimental prototypes. Indeed, the simulation activity can provide realistic guidelines on the best materials and structure options to maximize the device performance and can help in the comprehension of the physical mechanisms involved in the device operation [27, 28]. Of course, since the early stage of the technology of the graphene–based devices, the physics–based models must be continuously benchmarked against experimental measurements, in order to realistically predict the device performance. This thesis is positioned in this framework and it is focused on the development and integration of models/simulators dedicated to graphene–based devices, especially related to GFET and GBT architectures, with the aim to explore the performance limits of these devices.

The thesis is organized as follows. In Chapter 2 we discuss the material properties of graphene, providing the basic concepts behind the theory describing the graphene honeycomb lattice. Later, we illustrate the most interesting properties of this 2D material, from the electrical to the thermal ones. Then, we briefly describe the state–of–the–art of graphene–based devices and, in particular, of GFET and GBT devices, mostly focusing on RF application.

Chapter 3 is focused on one of the most impacting issues for GFET devices, the already mentioned resistance related to the metal/graphene contact, which seriously contributes to the increase of device access resistance. First, we introduce the Monte Carlo (MC) simulator developed at the University of Udine [29], which solves the semi–classical transport in GFET devices. We show how the metal/graphene stack is modeled in order to be included in the simulator. Furthermore, we discuss how to include directly in the MC simulator the detrimental effect of the series resistance at the source and drain terminals.
The end of the chapter is instead focused on the experimental characterization of the metal/graphene contact resistance, based on a specific experimental technique. Indeed, the modelling of the series resistance requires an in–depth understanding of the physical mechanisms occurring at the metal/graphene interface, hence, proper extraction methods are required to characterize the metal/graphene contact and to calibrate the corresponding models.

Chapter 4 is mostly dedicated to the modelling of the GBT. First, we describe the developed electrical model for GBT devices, that includes also secondary effects as the space charge effects. The model is able to predict the maximum achievable cutoff frequency, considering all of the most important contributions impacting the RF performance. The validation of the electrical model has been made by comparison against alternative simulation approaches and experimental results [30].
Once calibrated, the electrical model allows us for an exploration of the GBT design space, considering realistic insulator materials and trying to optimize the device structure in terms of the principal RF figures of merit.

We also developed a Monte Carlo simulator to investigate the electron transport in GBTs, capable to estimate the contribution of electron scattering to the base current, which is very large in the first experimental GBT prototypes.
Finally, the last section is dedicated to the simulation of the most recent and advanced GBT structures [31], with the aim to assess the final RF performance of the GBT.

Chapter 2

Graphene in Nanoelectronics

Because of its extraordinary high carrier mobility and large velocity saturation, from its discovery graphene has created large expectations as possible material for the replacement of Si in the conventional Metal–Oxide–Semiconductor–Field–Effect–Transistor. Furthermore, its monoatomic thickness due to its two–dimensional structure should ensure a good electrostatic control of the channel by the gate terminal, partially solving the short channel effects in ultra–scaled devices. In this context, this chapter first introduces the monolayer graphene structure in Sec. 2.1, discussing its honeycomb crystal lattice, the gapless energy dispersion relationship, as well as its limited density of states. Then, a summary of the most interesting properties of graphene (i.e. electrical, mechanical, optical and thermal) is provided, mainly keeping the focus on the possible electronic devices applications. Section 2.2 finally presents the state–of–the–art of graphene–based devices, starting from the most conventional architecture, namely the Graphene–Field–Effect–Transistor (GFET), to more exotic ones featuring perpendicular transport across the graphene plane.

2.1 Graphene

As stated above, in this section we briefly present the monolayer graphene in terms of crystal lattice and band structure. The section starts with the description of a general three–dimension (3D) crystal lattice, that will be a useful guide toward the understanding of the two–dimensional (2D) graphene crystal lattice and the corresponding energy dispersion relation. Finally we provide a summary of the most interesting properties of graphene.

2.1.1 Crystal and reciprocal lattice

In general, the crystal structure is an ordered state of matter that can be represented by the combination of a *Bravaix lattice* and a *basis* [32]. Concerning the former, it is a periodic set of discrete points, the so–called *points of symmetry*, which features the property to see around itself exactly the same pattern with respect to any other symmetry point. The basis, instead, denotes the arrangement of the atoms in a *Bravaix lattice* period.
A Bravaix lattice for a 3D crystal can be mathematically described as:

$$\mathbf{R_n} = \sum_{k=1}^{3} n_k \mathbf{a}_k, \tag{2.1}$$

where n_k is an integer number, while $\mathbf{a}_k$ are the *primitive vectors*. The choice of the latter ones is totally arbitrary and consequently not unique.
Let us define now the *primitive unit cell*, a volume that could be placed periodically in the lattice

structure without create either overlaps or empty regions by a translation of vectors in the form of Eq. 2.1, expressible by the set of the points satisfying:

$$\mathbf{R} = \sum_{k=1}^{3} x_k \mathbf{a}_k, \tag{2.2}$$

where x_k can assume values between 0 and 1. A common way to form a *primitive cell* is the *Wigner–Seitz–cell* structure, which is created intersecting the perpendicular planes to the segment that joins one lattice point with the closest neighbors.
The periodic structure described so far is also called *direct lattice*. The *reciprocal lattice*, defined in the wave-vectors space, is instead:

$$\mathbf{G_m} = \sum_{k=1}^{3} m_k \mathbf{b}_k, \tag{2.3}$$

where $\mathbf{b}_k$ are the primitive vectors in the reciprocal space, while m_k are integers numbers satisfying the relation:

$$\exp\left(i\mathbf{G_m} \cdot \mathbf{R_n}\right) = 1, \tag{2.4}$$

which is valid when:

$$\mathbf{b}_i \cdot \mathbf{a}_j = 2\pi\delta_{ij}, \tag{2.5}$$

where the δ_{ij} is the Kronecker's delta, while $\mathbf{a}_j$ and $\mathbf{b}_i$ are again the primitive vectors of the direct and reciprocal lattice, respectively (see Eqs. 2.2 and 2.3). It can be demonstrated that Eq. 2.5 is verified when:

$$\mathbf{b}_1 = \frac{2\pi}{\Omega_{cell}}(\mathbf{a}_2 \times \mathbf{a}_3), \quad \mathbf{b_2} = \frac{2\pi}{\Omega_{cell}}(\mathbf{a}_3 \times \mathbf{a}_1), \quad \mathbf{b_3} = \frac{2\pi}{\Omega_{cell}}(\mathbf{a}_1 \times \mathbf{a}_2), \tag{2.6}$$

where Ω_{cell} is the volume of the primitive cell defined above, namely $\Omega_{cell} = \mathbf{a}_1 \cdot (\mathbf{a}_2 \times \mathbf{a}_3)$.

We can now apply the above mathematical representation of the crystal lattice to describe the direct and reciprocal lattice of graphene. *Graphene* is a planar allotrope of carbon, composed by a monolayer of carbon atoms arranged in a honeycomb structure forming a 2D lattice (Fig. 2.1), in which atoms form covalent bonds with each other on the plane [34]. By looking to Fig. 2.2, which shows the arrangement of carbon atoms in the graphene lattice in real space, we define the distance between two adjacent atoms as $L_b = 1.42\ \mathring{A}$. We can identify the primitive cell for

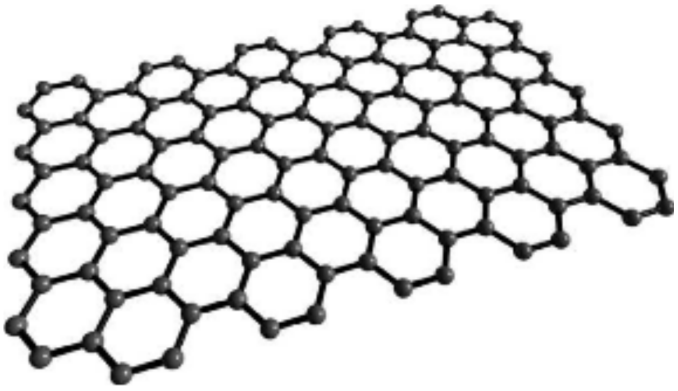

Figure 2.1: Atomic structure of graphene monolayer, showing the hexgonal honeycomb pattern (adapted from [33]).

graphene as composed by a basis of two carbon atoms (blue circle, note the periodicity of the cell in Fig. 2.2). Because of the 2D lattice of graphene, Eq. 2.1 becomes [34]:

$$\mathbf{R} = n_1\mathbf{a}_1 + n_2\mathbf{a}_2, \tag{2.7}$$

where (n_1, n_2) is a couple of integer numbers, while $\mathbf{a}_1$ and $\mathbf{a}_2$ are the primitive vectors of graphene, expressed as:

$$\mathbf{a}_1 = a\hat{\mathbf{x}} + b\hat{\mathbf{y}} \tag{2.8}$$

$$\mathbf{a}_2 = a\hat{\mathbf{x}} - b\hat{\mathbf{y}}. \tag{2.9}$$

The terms a and b are:

$$a = \frac{\sqrt{3}}{2}a_0 \tag{2.10}$$

$$b = = \frac{a_0}{2}, \tag{2.11}$$

respectively, where a_0 is the distance between two adjacent lattice points (lattice constant), namely:

$$a_0 = 2\cos(\frac{\pi}{6})L_b = \sqrt{3}L_b = 2.46, \tag{2.12}$$

expressed in $\mathring{A}$.

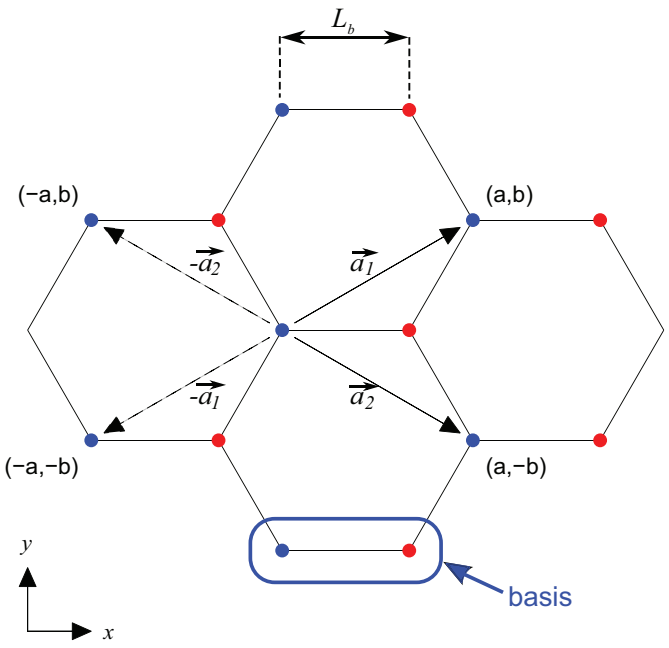

Figure 2.2: Sketch of the graphene direct lattice in real space. In blue is circled the two-atoms basis while the blue atoms represent the lattice points. $\mathbf{a}_1$ and $\mathbf{a}_2$ are the primitive vectors. Image adapted from [33].

Concerning the reciprocal lattice of graphene, the primitive vectors of the reciprocal lattice are defined following Eq. 2.6, so that:

$$\mathbf{b}_1 = 2\pi\frac{\mathbf{a}_2 \times \hat{\mathbf{z}}}{\mathbf{a}_1 \cdot (\mathbf{a}_2 \times \hat{\mathbf{z}})} = \hat{\mathbf{k}_x}\left(\frac{\pi}{a}\right) + \hat{\mathbf{k}_y}\left(\frac{\pi}{b}\right) \tag{2.13}$$

$$\mathbf{b}_2 = 2\pi\frac{\mathbf{a}_1 \times \hat{\mathbf{z}}}{\mathbf{a}_1 \cdot (\mathbf{a}_2 \times \hat{\mathbf{z}})} = \hat{\mathbf{k}_x}\left(\frac{\pi}{a}\right) - \hat{\mathbf{k}_y}\left(\frac{\pi}{b}\right), \tag{2.14}$$

where $\hat{\mathbf{k}_x}$ and $\hat{\mathbf{k}_y}$ coincide with the unit vectors $\hat{\mathbf{x}}$ and $\hat{\mathbf{y}}$ of Eqs. 2.8 and 2.9, respectively. At this stage, it is possible to construct the entire reciprocal lattice and identify the First Brillouin Zone (FBZ), defined as the primitive cell in the reciprocal lattice, by means of the Wigner–Seitz–cell, whose vertices, normally noticed with K–points but known as *Dirac Points* for graphene, are:

$$\begin{aligned} &\left(0, +\frac{2\pi}{3b}\right), \quad \left(+\frac{\pi}{a}, +\frac{\pi}{3b}\right), \quad \left(+\frac{\pi}{a}, -\frac{\pi}{3b}\right), \\ &\left(0, -\frac{2\pi}{3b}\right), \quad \left(-\frac{\pi}{a}, -\frac{\pi}{3b}\right), \quad \left(-\frac{\pi}{a}, +\frac{\pi}{3b}\right), \end{aligned} \tag{2.15}$$

positioned in a hexagonal shape as shown in Fig. 2.3.

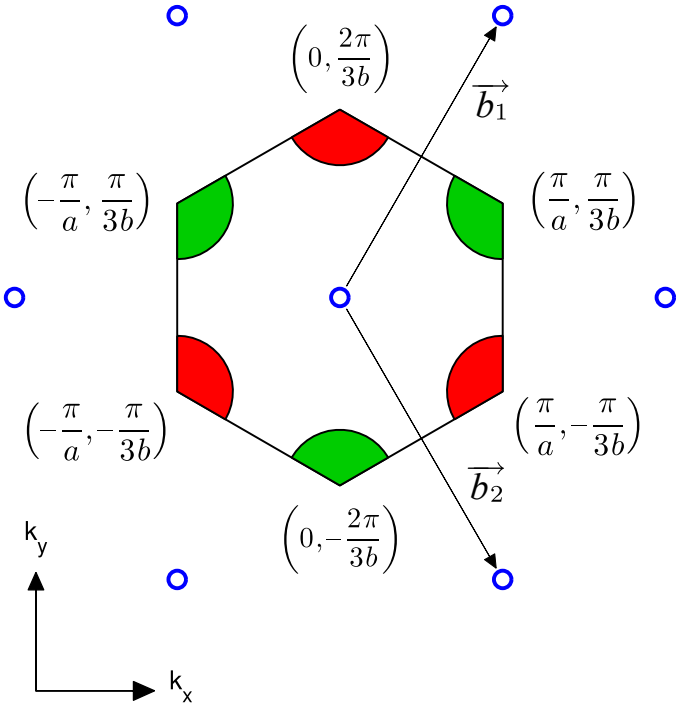

Figure 2.3: Graphene reciprocal lattice (blue empty points) and first Brillouin zone (black solid line). $\mathbf{b}_1$ and $\mathbf{b}_2$ are the reciprocal lattice vectors. Vertices belonging to the same degenerate valley are highlighted with the same color (green or red). Figure adapted from [33].

2.1.2 Band structure and energy-dispersion relation

The band structure of graphene can be determined by solving the Schrödinger equation by means of a tight–binding approach, namely:

$$E(\mathbf{k}) = [h(\mathbf{k})](\psi), \tag{2.16}$$

where $h(\mathbf{k})$ $[s \times s]$ is the Hamiltonian operator. By getting the eigenvalues of the latter we are able to obtain the energy-dispersion relation $E(\mathbf{k})$ (giving the energy level for every wave-vector), which presents a number of branches equal to s, corresponding to the dimension of the Hamiltonian matrix or equivalently the number of eigenvalues. By considering the 4 orbitals (namely $2s$, $2p_x$, $2p_y$ and $2p_z$) for each carbon atom, we can assert that there are 8 orbitals for every primitive cell, since it is inclusive of two atoms. Furthermore, it can be shown that the energy levels close to the Fermi energy are determined by the $2p_z$ orbitals only, while the $2s$,

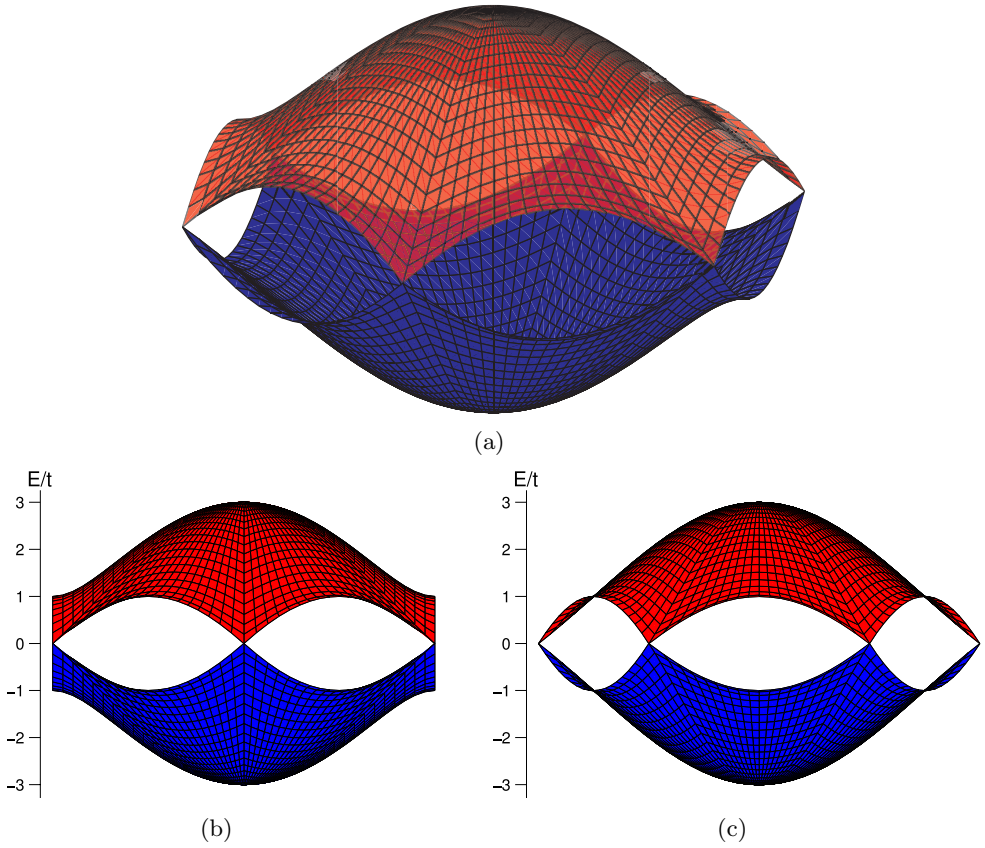

(a) (b) (c)

Figure 2.4: Graphene band structure (a) and corresponding projection along k_x (b) and k_y (c). The conduction band is colored in red, while the valance band in blue. Adapted from [33].

$2p_x$ and $2p_y$ can be neglected in the calculation since their energy levels are too far with respect to the Fermi energy, resulting in s=2. When the closest–neighbors are considered, the matrix $[h(\mathbf{k})]$ can be expressed as:

$$[h(\mathbf{k})] = \begin{bmatrix} 0 & h_0^* \\ h_0 & 0 \end{bmatrix}, \tag{2.17}$$

where

$$h_0 = -t[1 + 2\exp(ik_x a)\cos(k_y b)], \tag{2.18}$$

where $t = 2.7$ eV is the hopping integral between two nearest–neighbors [17]. As a result, the branches of the energy dispersion relation can be now expressed as

$$E = \pm t\sqrt{1 + 4\cos(k_y b)\cos(k_x a) + 4\cos^2(k_y b)}. \tag{2.19}$$

Figure 2.4(a) shows the band structure of graphene (the red and blue surfaces are the conduction and valance band, respectively), while in Fig. 2.4(b) and Fig. 2.4(c) are reported the corresponding projections along the $\mathbf{k}_x$ and $\mathbf{k}_y$ directions, respectively. As visible, the conduction band and the valance band are touching each other in the six hexagonal shaped vertices of the FBZ (Dirac Points), resulting in a gapless energy dispersion relation. Furthermore, the profile of the energy surfaces at the Dirac Points is symmetric for the conduction and valance band, leading to the well–known ambipolar behavior of graphene.

Focusing in the proximity of the Dirac Points, the energy dispersion relation in Eq. 2.19 can

be approximated with a linear equation, namely:

$$E(\mathbf{k})^{\pm}_{linear} = \pm\hbar v_f |\mathbf{k}_{DP}| = \pm\hbar v_f \sqrt{k^2_{x,DP} + k^2_{y,DP}}, \tag{2.20}$$

where $\hbar$ is the reduce Planck's constant, $k_{x,DP}$ and $k_{y,DP}$ are the k_x and k_y components refereed to the Dirac Point, respectively, while v_f is the *Fermi velocity*, defined as:

$$v_f = \frac{\sqrt{3}}{2} \cdot \frac{a_0 tq}{\hbar}, \tag{2.21}$$

and, consequently, the group velocity v_g corresponds to the Fermi velocity in proximity of the Dirac Point:

$$v_g = \frac{1}{\hbar}\frac{\partial E}{\partial k} = v_f. \tag{2.22}$$

The linear energy-dispersion relation in Eq. 2.20 is representative of the massless particles (massless Dirac fermions), that are particles with zero effective mass, responsible of the very high carrier mobility in graphene [10] (see Sec. 2.1.4). The linear dispersion relationship has been demonstrated up to 0.6 eV from the Dirac Point by experimental spectroscopic measurements [35]. Hereafter we will assume that $k_x = k_{x,DP}$ and $k_y = k_{y,DP}$.
The eigenvectors, obtained by solving Eq. 2.16, are [36]:

$$\boldsymbol{\psi}_k = \frac{1}{\sqrt{2}} \begin{bmatrix} \exp(-i \cdot a_k/2)) \\ \pm \exp(i \cdot a_k/2) \end{bmatrix}, \tag{2.23}$$

where $a_k = k_y/k_x$ and the plus and minus signs are referred to conduction and valance band, respectively. Finally, the spinor–overlap $F_{\boldsymbol{k}}$ between two states $\boldsymbol{k}$ and $\boldsymbol{k'}$, both belonging to the conduction band is defined as:

$$F_{\boldsymbol{k},\boldsymbol{k'}} = \boldsymbol{\psi}^{\dagger}_{\boldsymbol{k}} \cdot \boldsymbol{\psi}_{\boldsymbol{k'}} = \frac{1 + \cos\theta}{2}, \tag{2.24}$$

where θ is the angle between $\boldsymbol{k}$ and $\boldsymbol{k'}$ and $\dagger$ is the conjugate transpose.

2.1.3 Density of states and carrier concentration

The density of states (DoS) of graphene at low energies can be estimated as [17]:

$$DoS(E) = \frac{2n_\nu n_s}{(2\pi)^2} \int_{\mathbf{k}} \delta[E - E(\mathbf{k})] d\mathbf{k} = \frac{2}{\pi} \left(\frac{q}{v_f \hbar}\right)^2 E, \tag{2.25}$$

where q is the modulus of the electron charge, while n_s and n_ν are the number of the spin and of the degenerate valleys, respectively. Concerning the latter and looking to Fig. 2.3, the six minimum of the FBZ are contributing to a third of a single degenerate valley, finally resulting in two degenerate valleys (n_ν=2, grouped in green and red, respectively). Furthermore, the properties of symmetry and linearity of the energy dispersion relation in the proximity of the Dirac Point (Eq. 2.20) lead to a symmetric and linear DoS in the conduction and valance bands. Equation 2.25 shows that the DoS of graphene is finite and very low in the proximity of the Dirac Point; as a consequence, the effect of the resulting limited quantum capacitance must be necessary taken into account in the electrostatics determination of the graphene–based devices (see Secs. 3.3.1 and 4.3).
Electrons and holes concentrations (n and p, respectively) are generally expressed as:

$$n = \int_0^{\infty} DoS(E) \cdot f(E)\ dE \tag{2.26}$$

$$p = \int_{-\infty}^{0} DoS(E) \cdot [1 - f(E)]\ dE, \tag{2.27}$$

where $f(E)$ is the occupation probability described by the Fermi–Dirac statistics, namely:

$$f(E) = \frac{1}{1 + \exp\left[\frac{q(E-E_F)}{k_B T}\right]}, \tag{2.28}$$

where E_F is the Fermi level, k_B is the Boltzmann's constant and T the temperature. By using Eq. 2.28, the electron and holes concentration in Eqs. 2.26 and 2.27 become [37]:

$$n = \frac{2}{\pi\hbar^2 v_f^2}\mathcal{F}_1(E_F/k_B T) \tag{2.29}$$

$$p = \frac{2}{\pi\hbar^2 v_f^2}\mathcal{F}_1(-E_F/k_B T), \tag{2.30}$$

where $\mathcal{F}_1(E_F/k_B T)$ is the first order Fermi integral of $E_F/k_B T$.

2.1.4 Main characteristics of graphene

The particular crystal structure of graphene results in unique properties. Among them, we recall:

- **Electrical characteristics** - Graphene exhibits very high *carrier mobility*, mainly due to the low effective mass of carriers (see Sec. 2.1.2). Electron mobility up to 10^6 cm^2/(Vs) [10, 38] has been reached for suspended monolayer graphene in vacuum, which is more than 100 times higher than in Silicon (Si). However, remote phonon scattering have a strong impact on the carrier transport in graphene when deposited on insulator substrates, drastically reducing the carrier mobility [39, 40]. Indeed, mobility of 15000 cm^2/(Vs) has been measured for Chemical Vapor Deposited (CVD) graphene transferred on SiO_2 substrate [41, 42] that is, anyway, much larger than in the Si channel of MOSFETs. Furthermore, the *velocity saturation* in graphene has been estimated to be ∼5 times larger than in Si [43] leading, as a consequence, to very low resistivity of the material (about 10^{-8} Ω). Finally, as already anticipated, the symmetric band structure of graphene (see Fig. 2.4) results in the *ambipolarity* of the material, making possible the electrostatical doping of graphene through the simple application of an electric field, influencing the position of the Fermi level (see Sec. 3.3.1). In fact, shifting the Fermi level in the valance band, the graphene could be enriched of holes or, alternatively, electrons when the Fermi level lies in the conduction band. On the other hand, the absence of a energy gap in graphene limits its applications for digital electronics (see Sec. 2.2);

- **Optical characteristics** - Monolayer graphene is *transparent*, with the 97.7% of the radiation crossing the layer [6, 44], which is an essential feature for interesting optical applications (e.g. flexible display [45], light–emitting diodes [46], photodetectors [47, 48], etc.);

- **Mechanical characteristics** - Despite its atomic thickness, graphene shows an *extraordinary strength* (it exhibits a Young's modulus in the range of 0.5–1 TPa), due to the σ–bonds occurring between the electrons of the carbon atoms arranged in the plane. On the contrary, by considering vertically stacked graphene layers (namely graphite), the weak π–bonds formed in the perpendicular direction make possible the mechanical exfoliation of graphite in singles monoatomic layers. Furthermore, monolayer graphene is extremely *bendable*, being stretchable up to 20% [49]. These mechanical characteristics make graphene an excellent candidate for the implementation of Nano–ElectroMechanical Systems (NEMS) [50], as well as for flexible–electronic applications [51];

- **Thermal characteristics** - Experimental data confirm that, at room temperature, the *thermal conductivity* values of graphene can vary in the range 4800–5300 W/mK [52], much better than those of diamond (1000–2200 W/mK). This is a paramount characteristic for electronic applications, since it demonstrates the capability of the material to quickly dissipate the heat.

2.2 State–of–the–art of graphene–based devices

From its discovery, graphene has been considered a possible candidate in the semiconductor industry for the post–Si age. Besides its incredible high carrier mobility, the atomic thickness of graphene is one of the most attractive characteristics from the point of view of electronic devices. Indeed, devices featuring graphene as alternative channel material may be down–scaled without facing the short channel effects strongly impacting the conventional MOSFETs, hence possibly overcoming the state–of–the–art of the semiconductor–based devices [53, 54]. Moreover, as mentioned above, the good thermal properties (Sec. 2.1.4) further motivate the integration of graphene in CMOS technology. The current section presents the state–of–the–art of the graphene–based devices mainly focusing on the Radio Frequency (RF) applications, starting from the largely investigated Graphene–Field–Effect–Transistors, and later moving to more recent and alternative vertical device concepts, which exploit perpendicular charge transport with respect to the graphene plane.

2.2.1 Graphene–Field–Effect–Transistor

As already stated, the use of alternative channel material replacing silicon (Si) in conventional Si Metal–Oxide–Semiconductor Field–Effect–Transistors (MOSFTEs) represents a possible way to overcame the physical limits imposed to the scaling and keep the progress of the integrated circuit technology. In this framework, graphene has been widely investigated as channel material, in the so–called Graphene–Field–Effect–Transistor (GFET), which is nowadays the most mature and studied architecture among the graphene–based devices [11, 42, 55, 56, 57, 58, 59, 60].

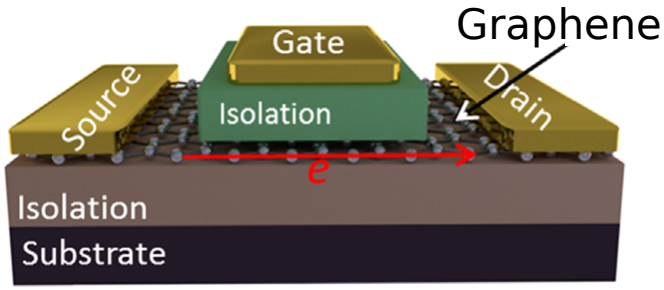

Figure 2.5: Sketch of a Graphene–Field–Effect–Transistor (GFET). Adapted from [61].

Figure 2.5 shows a generic GFET structure, consisting in an insulator substrate with a large–area graphene channel on the top, the metal source and drain contacts at the sides of the graphene channel and a thin–dielectric separating the graphene from the gate. The use of monolayer graphene allows to exploit its incredible high carrier mobility and, moreover, should ensure an excellent electrostatic control of the device by the gate terminal, because of the graphene monoatomic thickness. Concerning RF performance and the achievable cutoff frequencies (f_T), experimental GFETs (claiming a record of f_T=427 GHz [11]) can well compete with the state–of–the–art nanoscale RF devices, see Fig. 2.6, even though the unity power gain is still limited (f_{max} slightly above than 100 GHz [67]).

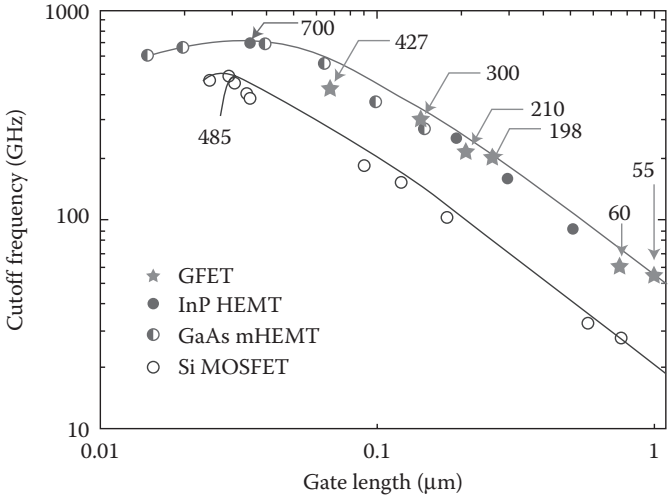

Figure 2.6: Experimental cutoff frequency as a function of the gate lenght achieved by GFETs (stars, taken from [11, 51, 59, 62, 63, 64]) and by other RF devices (i.e. InP HEMTs, GaAs mHEMTs [12, 65] and RF Si MOSFETs [12]). The solid lines are guides for the eyes showing the general trend of the cuttoff frequency as a function of the gate length. Adapted from [66].

Nevertheless, there are still some critical issues limiting GFETs performance, which must necessarily be overcome in order to make GFETs truly competitive with conventional semiconductors–based devices. For instance, the lack of a bandgap in graphene is also responsible of the non–saturated output characteristics of GFETs, causing the increase of the output conductance, thus limiting the intrinsic gain of the device [12]. Furthermore, the carrier mobility is strongly impacted both by the dielectrics sandwiching the graphene monolayer, as mentioned in Sec. 2.1.4, and by the fabrication process. Finally, the contact resistance associated to the metal/graphene interface at the source and drain of GFETs still represents a fundamental limit (see Chap. 3). On the other hand, GFETs are really promising candidates for flexible–electronics, showing the capability to reach f_T and f_{max} in the order of 200 GHz and 28 GHz, respectively, when flexible substrates are used [51, 66].
Briefly discussing also the possible application of GFETs in digital logic gates, the zero bandgap of monolayer graphene is a kind of roadblock. In fact, the gapless energy dispersion relation results in very poor I_{ON}/I_{OFF} ratios, showing values laying order of magnitudes below the ITRS (International Technology Roadmap for Semiconductors) requirements. To solve this critical issues intrinsically related to the nature of graphene, different techniques have been proposed to induce a bandgap, namely the use of graphene strips (creating a bangap through quantization by cutting the graphene in narrow nanoribbons [17, 18, 19, 40, 68, 69]), graphene bilayer (obtained stacking two graphene sheets according to Bernal approach [20, 21]) or inducing strain in the graphene [70]. However, this solutions are quite far from a mature technology.

2.2.2 Vertical transport graphene transistors

The concept of vertical graphene–based transistors, that exploits the charge transport perpendicular to the graphene plane, is more recent and less investigated than the GFET architecture, especially at experimental level. In this category of devices, we find the graphene barristors (proposed in [71] and exploiting the modulation of a graphene/semiconductor Schottky barrier to tune the current crossing the device), the vertical field–effect transistor based on graphene reported in [72, 73, 74] (exploiting the tunneling through a thin insulating layer placed between

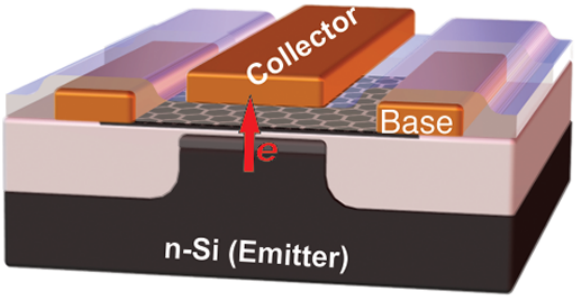

Figure 2.7: Sketch of a Graphene–Base–Transistor (GBT). Adapted from [30].

two graphene layers) and the Graphene–Base–Transistor (GBT), proposed in [22]. Concerning the latter, the GBT structure consists in two insulating layers sandwiching the graphene base and forming a vertical stack that separates the emitter from the collector, as in Fig. 2.7.

The working principle of the GBT is similar to the metallic–base Hot–Electron–Transistor (HET) and it is based on the tunneling of hot electrons through thin–insulating layers [75, 76]. In HETs, a fundamental requirement for the achievement of high performance, is to keep the thickness of the metal–base as thin as possible, in order to ensure (i) quasi–ballistic tunneling transport through the base and (ii) a short base transit time. On the other hand, the extreme shrinking of the base leads to an increase of the base resistance, which limits the RF performance. For this reasons, the use of graphene as base represents an excellent solution to overcome this trade–off, since the atomic–thickness of the layer and the semi–metallic behavior due to its high carrier mobility (that results in low base resistances).
The DC functionality of the GBT has been already proven experimentally [30, 31, 61, 77], but, at the moment, RF performance have been investigated by simulations only. However, these simulation works have shown the great potentialities of GBTs in reaching cutoff frequencies and unity power gains exceeding 1 THz [23, 24, 26, 78] (see Chap. 4).

Also alternative versions of the GBT have been proposed, as the Graphene–Base Heterojunction Transistor (GBHT [79, 80]), obtained by stacking a semiconductor emitter, a monoloayer graphene acting as base and a semiconductor collector. During normal operation, the height of the quasi–triangular barrier formed between the emitter and the collector (because of the difference between the work–functions of the semiconductors and the graphene layer) is controlled by the base–emitter voltage. Differently from the GBT, where the conduction is given by injection from the emitter of electrons able to tunnel the insulating layers, in the GBHT the conduction is governed by thermionic emission over the barrier. The advantage of GBHT with respect to GBT is mainly the absence of insulating layers in the transistor architecture, whose optimization is critical concerning process fabrication. Simulations of ideal GBHTs have confirmed their RF potentialities, showing f_T in the range of THz and an intrinsic voltage gain higher than 10 [79, 80].

Chapter 3

The Metal/Graphene Contact in GFETs

3.1 Introduction

As introduced in Sec. 2.2, the large carrier mobility in graphene can boost the performance of devices for Radio Frequency (RF) electronics. In particular, during the last decade, graphene has been largely investigated as alternative channel material in MOSFETS devices, leading to the Graphene–Field–Effect–Transistors (GFETs). Although nowadays GFETs have reached cutoff frequencies comparable with many well-established technologies (see Sec. 2.2.1), the series resistance still represents one of the major drawbacks of the device [16, 81]. Indeed, the far from ideal metal/graphene contacts induce high series resistances, that strongly limits the performance of GFETs and, in particular, reduce the extrinsic transcoductance. If compared with the contact resistance of transistors exploiting Si or III–V materials, the metal/graphene resistance exhibits values that are much larger, see Tab. 3.1. Furthermore, the characteristics of metal/graphene contacts present several critical points, for instance the strong dependence on the fabrication process, on the measurement conditions (e.g. measurements in air or vacuum) and on the biasing conditions, because of the possibility to electrostatically dope the graphene.

Table 3.1: Comparison of the metal/graphene contact resistance against contact resistance achieved in Si or III-V transistors.

Transistor	R [$\Omega\ \mu m$]	Metal	Ref.
Si-MOSFET	<10		[82]
InP-HEMT	30		[83]
GFET	69	Pd	[84]
	84	Pd	[85]
	100	Ni	[86]
	<100	Ti/Pt/Au	[87]
	110	Pd/Au	[14]

In this framework, accurate models able to realistically predict GFETs performance also including the strongly limiting extrinsic parameters (e.g. the series resistances) are strictly necessary for the development of the GFET technologies. Among other simulation approaches, semi–classical transport models are one of the best options to this purpose; in fact, scattering mechanisms can be easily implemented and the computational cost is less if compared to full–quantum simulators, e.g. based on Non–Equilibrium Green's Functions (NEGF). At this

regard, in Sec. 3.2 we provide an overview of the Monte Carlo (MC) simulator for GFET devices developed at the University of Udine [29]. The model was initially developed to simulate only GFETs with chemically doped Source (S) and Drain (D) regions. However, since the technological difficulties in chemically dope the graphene, there was the need to extend the Monte Carlo model to simulate devices with electrostatically doped S/D regions, which is a technological ready option for GFETs. Hence, in Sec. 3.3, we introduce the modelling of the metal/graphene stack, providing also a comparison between GFET with chemically and electrostatically doped S/D. Furthermore, once evaluated the series resistance value, a common way to include this detrimental effect in the device performance is the use of the look–up–tables approach, based on a post–processing of a large set of simulations [88]. Here, instead, we included the series resistances directly in the self–consistent loop of the Monte Carlo simulator, thus directly accounting for their effect during the device current calculation. The details of the used modelling approach are given in Sec. 3.4.
Furthermore, the modelling of series resistances requires an in-depth understanding of the physical mechanisms occurring at the metal/graphene contact. As a consequence, there is the need of experimental techniques able to characterize the different contributions to the overall access resistance of the device. In this framework, in Sec. 3.5 we revised the concept of the front–contact and end–contact resistance methods applied to the measurements of transfer length method (TLM) structures, which can provide important reference data to verify and calibrate the simulations models.

3.2 Monte Carlo simulator for GFETs

In the current section we make an overview of the Monte Carlo simulator developed at University of Udine, that solves the semi–classical charge transport in GFET devices, including also the main Generation/Recombination (G/R) mechanisms. We summarize the fundamental aspects of the modelling approach and the validation of the model against results of a NEGF-based simulator developed ad the University of Pisa [69] and against experiments. All the details of the Monte Carlo simulator can be found in [29, 89].

Figure 3.1 shows the flow chart of the semi–classical Monte Carlo for GFET devices. The gapless energy dispersion relation $E = \hbar v_f |\mathbf{k}|$ and the translational invariance along the width (W) directions are assumed. The Boltzmann Transport Equation (BTE) for electrons and holes is coupled in a self–consistent loop to the non–linear Poisson equation, implemented as:

$$\begin{aligned} \nabla \cdot \left[\frac{\varepsilon(\mathbf{r})}{q} \nabla \phi(\mathbf{r})^{(k+1)} \right] &= n(\mathbf{r})^{(k)} \exp\left[\frac{\phi(\mathbf{r})^{k+1} - \phi(\mathbf{r})^{(}k)}{k_B T} \right] \\ &\quad - p(\mathbf{r})^{(k)} \exp\left[\frac{\phi(\mathbf{r})^{k+1} - \phi(\mathbf{r})^{(}k)}{k_B T} \right] - N_D(\mathbf{r}) + N_A(\mathbf{r}), \end{aligned} \tag{3.1}$$

where $\phi(\mathbf{r})^{(k+1)}$ and $\phi(\mathbf{r})^{(k)}$ are the potential calculated at the current and at the previous iteration, respectively, $N_D(\mathbf{r})$ and $N_A(\mathbf{r})$ are the donor and acceptor densities, while $\varepsilon(\mathbf{r})$ is the electric permittivity. Particles are steadily injected in the simulation domain following:

$$I_{e,i} = qW \int_0^\infty \frac{2v_f}{\pi} \frac{DoS(E)}{2} \frac{dE}{1 + \exp(\frac{E - qV_i - E_F^i}{k_B T})} \tag{3.2}$$

$$I_{h,i} = qW \int_0^\infty \frac{2v_f}{\pi} \frac{DoS(E)}{2} \frac{dE}{1 + \exp(\frac{E + qV_i + E_F^i}{k_B T})}, \tag{3.3}$$

where $v_f \approx 8.8 \times 10^7$ cm/s is the Fermi velocity (see Eq. 2.21), $DoS(E)$ is the density of states

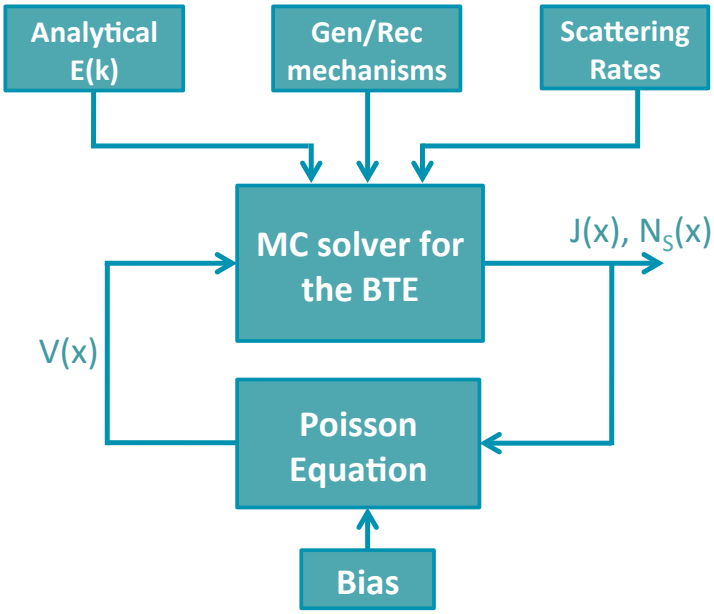

Figure 3.1: Flow chart of the Monte Carlo simulator: the Boltzmann Transport Equation (BTE) is coupled in a self–consistent loop to the Poisson's equation solver, which describes the electrostatics of the GFET.

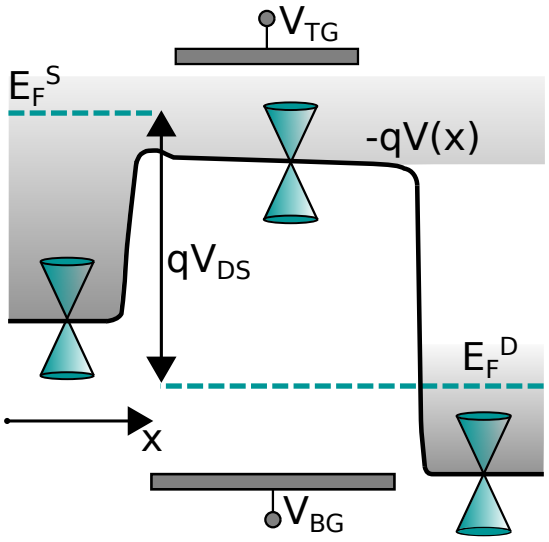

Figure 3.2: Sketch of the profile of the Dirac Point along a GFET with doped S/D regions along the transport direction x. The Fermi level at the source (E_F^S) and at the drain (E_F^D) are separated by qV_{DS}, taking $E_F^S = 0$ as reference level. Notice the flat profile in the S/D regions corresponds to a null electric field, hence with a constant charge concentration that corresponds to the graphene doping.

in graphene (Eq. 2.25), V_i is the potential at the source (if i=S) or at the drain (if i=D) and finally E_F^i is the corresponding Fermi level (see Fig. 3.2).

Concerning the scattering mechanisms, elastic intra–valley acoustic phonons have been in-

cluded following the approach of [17]:

$$S_{AP}(E(k_i)) = \frac{1}{2} \cdot \frac{2\pi k_B T D_{ac}^2}{\rho \hbar v_S^2} \cdot \frac{DoS(E(k_i))}{n_s n_v}, \tag{3.4}$$

where $n_S = 2$ is given by the spin, while $n_v = 2$ represents the number of the degenerate valleys. D_{ac}=14 eV is the deformation potential, ρ=7.6 kg/m^2 is the graphene density [90] and v_s=2 $\times$ 10^6 cm/s is the sound velocity in graphene [91].
Inelastic optical phonons have been modeled again following [17]:

$$S_{OP}(E(k_i)) = \frac{\pi D_{OP}^2}{\rho \omega_{OP}} \left(n_{OP} + \frac{1}{2} \mp \frac{1}{2} \right) \frac{DoS(E(k_i)) \pm \hbar\omega_{OP}}{n_s n_v}, \tag{3.5}$$

where upper and lower sign is for absorption and emission, respectively, $D_{OP} = 10^{11}$ eV/m is the deformation potential [92], $\hbar\omega_{OP}$=152 meV is the energy of the phonon [92] and $n_{OP} = 1/[\exp(\hbar\omega_{OP}/(k_B T)) - 1]$ is the phonon occupation.
Finally, remote phonon scattering originating in the dielectrics sandwiching the graphene layer have been included as in [18]:

$$S_{RP}(\mathbf{k_i}, \mathbf{k_f}) = \frac{2\pi}{\hbar A} |F_{\mathbf{k_i},\mathbf{k_f}}|^2 q^2 \left(n_{RP} + \frac{1}{2} \mp \frac{1}{2} \right) \frac{\hbar\omega_{RP}}{2|\mathbf{q}|\varepsilon} \exp(-2|\mathbf{q}|d) \delta[E(\mathbf{k_i}) - E(\mathbf{k_f}) \pm \hbar\omega_{RP}], \tag{3.6}$$

where A is the normalization area, $\mathbf{k_i}$ and $\mathbf{k_f}$ are the initial and final wave–vectors, respectively, separated each other by the angle θ, $F_{\mathbf{k_i},\mathbf{k_i}} = (1 + \cos\theta)/2$ is the spinor-overlap (see Eq. 2.24), $\mathbf{q} = \mathbf{k_f} - \mathbf{k_i}$ is the exchanged wave–vector ($|\mathbf{q}|^2 = (k_i^2 + k_f^2 - 2k_i k_f \cos\theta)$) and d is the distance between the dielectric and the graphene sheet. In this work d=0, since it has been verified that a change of d up to a few $\mathring{A}$ is not affecting the calculated current [33]. n_{RP} is the phonon occupation function given by $n_{RP} = 1/[\exp(\hbar\omega_{RP}/(k_B T) - 1]$, where $\hbar\omega_{RP}$ is the energy of the remote phonon. In the calculation of the scattering rates only the phonon at lowest frequency is considered and possible couplings between phonons belonging to different dielectrics are neglected.

Because of the gapless energy dispersion relation in graphene, Generation/Recombination mechanisms (G/R) play a substantial role in GFETs operation, leading to the strong ambipolar behavior of these devices. Recently, a local model describing band–to–band tunneling (BBT) phenomenon has been included in the Monte Carlo simulator [29], that can be written in terms of G/R by means of Wentzel–Kramers–Brillouin (WKB) approximation as:

$$\begin{aligned} G_{BBT}(x) - R_{BBT}(x) &\approx \frac{2eF_x(x)(f_v(x) - f_c(x))}{(2\pi)^2\hbar} \int_{-\infty}^{+\infty} \exp\left(- \frac{k_y^2 \hbar v_f \pi}{q F_x(x)} \right) dk_y \\ &= \frac{(f_v(x) - f_c(x))}{\pi^2 \sqrt{(v_f)}} \left(\frac{q F_x(x)}{\hbar} \right)^{3/2}, \end{aligned} \tag{3.7}$$

where $F_x(x)$ is the magnitude of the local electric field along the transport direction x, k_y is the y-component (normal with respect to the transport direction) of the wave–vector, $f_v(x)$ ($f_c(x)$) is the local occupation probabilities of the particles impinging the classical turning points in the valance (conduction) band. More specifically, at the drain side, where a high negative electric field is present (see Fig. 3.3), holes with positive group velocity (f_h^+) are contributing to f_v, while electrons with negative group velocity (f_e^-) contribute to f_c. In this region, the occupation term $(f_v - f_c) = 1 - f_e^- - f_h^+$ becomes quite close to 1, which means an high generation rate following Eq. 3.7. The generated holes move towards the source, where an high positive electric field is present, causing the recombination of a part of them with the electron injected from the source.

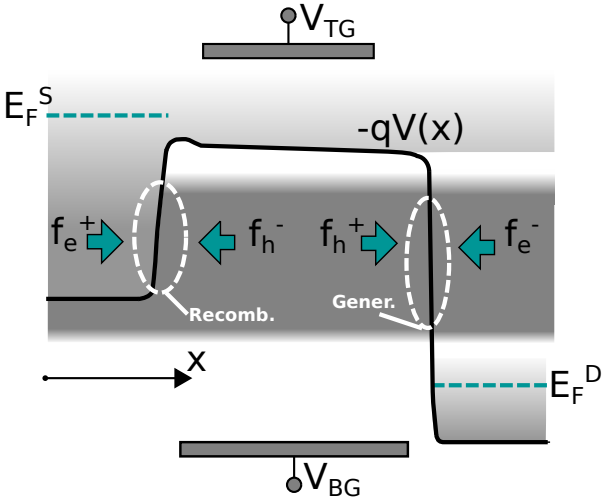

Figure 3.3: In the source region, a part of the holes generated at the drain side and moving toward the source experience recombination with the electron injected from the source. The remaining holes reach the source contact.

Fig. 3.3 reports a sketch of the situation illustrated above. It has been verified that Eq. 3.7 gives, at the maximum net generation rate, i.e. when $(f_v - f_c) = 1$, results similar to the full–quantum simulator NanoTCAD Vides [29].

Another G/R phenomenon included in the Monte Carlo simulator is the interband recombination assisted by phonons, by using the simplified expression [29]:

$$R_{IR}(x) = \frac{\min(n(x), p(x))}{\tau}, \tag{3.8}$$

where $n(x)$ and $p(x)$ are the electrons and holes concentration along x, respectively, while τ is the recombination time, fixed to 1 ps, consistently with [93] that estimates for this τ value a concentration of $n(x) = p(x) \approx 10^{12}$ cm^{-2}.

An important aspect directly correlated to this work is how the boundary conditions for the Poisson equation are treated (Eq. 3.1), namely:

- *Dirichlet conditions*, at top and bottom gates. Consequently, the potential at the mesh–points belonging to the top (V_{TG}) and at the bottom (V_{BG}) gates are directly applied;
- *Neumann conditions*, at the source and drain contacts. In these regions a null derivative of the potential with respect to the spatial variable x is imposed (note the flat profile inside the S/D regions in Fig. 3.3).

Since Neumann boundary conditions are assumed in the S/D regions, only GFETs with chemically doped S/D regions can be simulated, because of the null electric field imposed inside these regions.

Simulation results of nanoscale GFETs obtained by means of the developed Monte Carlo simulator have been compared against NEGF simulation results. The NEGF simulator has been developed at the University of Pisa, more details are reported in [29, 69]. For a fair comparison, all scattering mechanisms have been switched–off. Figure 3.4(a) reports the output characteristics of a GFET with a channel length (L_{CH}) of 30 nm, 1 nm of SiO_2 both as top and bottom dielectric, uniformly doped S/D regions ($N_D = 5 \times 10^{13}$ cm^{-2}) perfectly aligned with the top–gate [29]. The current calculated with the Monte Carlo (full symbols) is in good

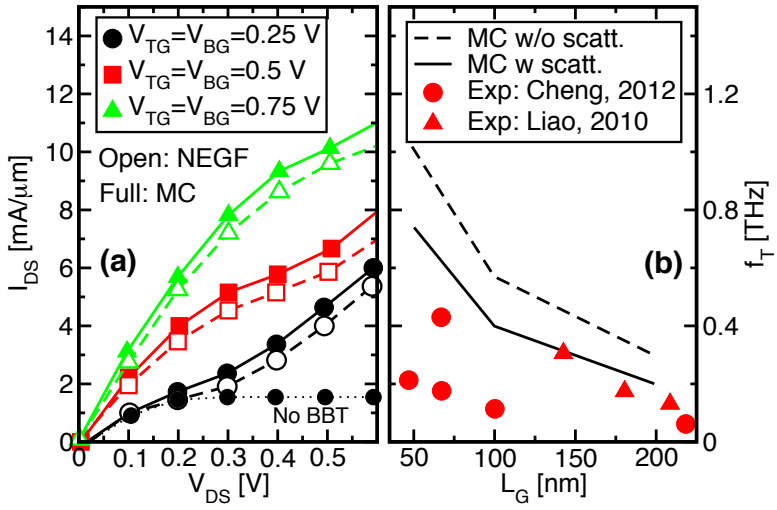

Figure 3.4: (a) Comparison between the simulated output characteristics obtained with the Monte Carlo simulator (full symbols) and by means of the NEGF simulator (empty symbols). For $V_{TG} = V_{BG} = 0.25\ V$, also a simulation without including BBT is reported (dot line). (b) Dependence of f_T as a function of channel length L_G. The inclusion of the scattering mechanisms in MC simulations (solid line) is necessary in order to approach the experimental values (symbols, [11, 59]). Adapted from [29].

agreement with the NEGF simulations (empty symbols), also for different values of the top–gate and bottom–gate biasing ($V_{TG} = V_{BG}$). Note how the Monte Carlo simulator, by accounting for BBT, is able to caught the typical ambipolar behavior of GFETs, which gives rise to the non–null output conductance at high V_{DS} voltages (the dotted line has been obtained non-considering the BBT).
Figure 3.4(b) shows instead the comparison between the cutoff frequency (f_T) extracted from the semi-classical simulations (lines) and from experimental devices reported in the literature (symbols, [11, 59]). The cutoff frequency is calculated using a quasi–static approach, namely:

$$f_T = \left.\frac{\Delta I_{DS}}{2\pi \Delta Q}\right|_{V_{DS}} \tag{3.9}$$

where ΔI_{DS} and ΔQ are the variations of the current and of the total charge in the entire device, respectively, obtained considering two simulations in which slightly different gate voltages are imposed. It can be noticed how the inclusion of the scattering mechanisms (solid line) reduces the simulated f_T, allowing a better agreement with the experimental data, than in the case of the ballistic simulation (dashed lines).

3.3 Modeling of electrostatic doping of source and drain regions in GFETs

In Sec. 3.2 we pointed out that the model of [29] can simulate only GFETs with chemically doped S/D regions. However, as already mentioned, chemical doping of graphene is still challenging for many reasons, as the limited long–term stability (due to the desorption from the graphene of the dopant atoms) or the poor reproducibility and homogeneity of the doped surface (the number of the dopants is difficult to control) [94, 95]. Therefore, in real devices, source and drain metal contacts are normally used to electrostatically dope and control the polarity of

the graphene underneath the metal contacts at the sides of the channel [96, 97]. Clearly, it is fundamental to include the effect of the metal/graphene Schottky contact in the Monte Carlo simulator, extending the model presented in Sec. 3.2.

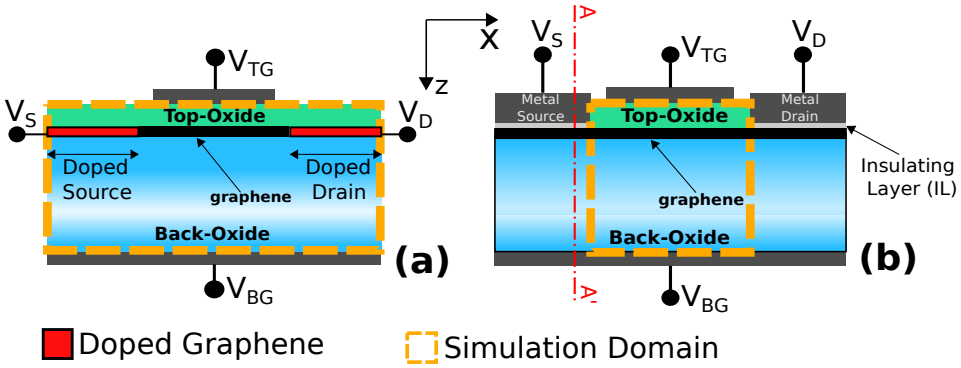

Figure 3.5: Sketch of GFETs with chemical doping (a) and electrostatic doping (b) induced by the S/D metals. V_{TG}, V_{BG}, V_S and V_D are the top–gate, back–gate, source and drain biases, respectively.

Figure 3.5 sketches GFETs with chemical doping (CD, (a)) and electrostatic doping (ED, (b)) in the S/D regions. The dashed orange box is the domain of the Monte Carlo transport simulation. For the case of chemical doping, S/D regions (reported in red) are part of the domain and Neumann boundary conditions are used in the Poisson equation (see Sec. 3.2). For the case of electrostatic doping, instead, S/D regions are external but coupled to the Monte Carlo domain, since they impose Dirichlet boundary conditions to the Poisson's equation, as explained in the following section.

3.3.1 Modeling of the metal/graphene interface

For ED GFETs, before the Monte Carlo transport simulation, the electrostatics of the vertical metal/grafene stack is solved (see section AA' in Fig. 3.5(b)), assuming the presence of an insulating layer (IL) between metal and graphene, acting as a tunnel barrier [98]. The introduction of the insulating layer allows to mimic different phenomena occurring at the metal/graphene interface, as the non–perfect adherence between the two materials, the electrochemical equalization and the resulting charge transfer which leads to the formation of a dipole at the interface. Furthermore, also orbital hybridization might partly be involved in real contacts, with the formation of π–d interactions between metal and graphene. On the other hand, the assumption of an insulating layer of 0.2 nm of vacuum is in line and consistent with previous works [99, 100].

Focusing now to the source contact of a GFET device, Fig. 3.6 shows the band diagram of the considered stack. For the sake of simplicity, Fig. 3.6 omits the back–oxide and the back–gate, reducing the structure to a *metal/IL/graphene* (MIG) capacitor, although the simulator implements the entire *metal/IL/graphene/back–oxide/metal* (MIGIM) structure, as reported in Fig. 3.5(b). Clearly, the tunneling barrier associated to IL can be seen as a tunneling resistance at the contacts, an additional contribution to the series resistance. Nevertheless, we will temporarily neglect this effect, whose role will be addressed in Sec. 3.4, in which we discuss the introduction of the series resistance in the Monte Carlo simulator. For this reason the metal Fermi level ($E_{F,M}$) is perfectly aligned with the Fermi level of graphene underneath the S/D contact ($E_F^{S/D}$), as visible in Fig. 3.6.

The electrostatics of the MIG structure at the source (as well as at the drain) is governed

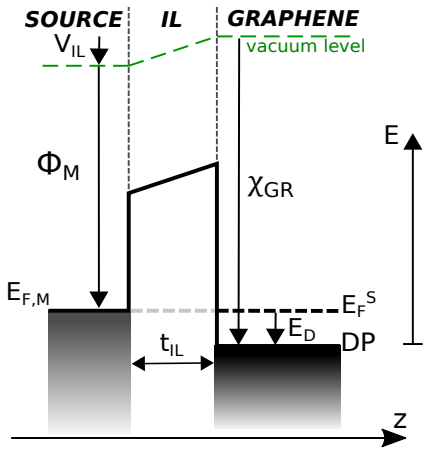

Figure 3.6: Band diagram at the source contact along the section AA' of Fig. 3.5, neglecting the presence of the back–gate.

by the following equations:

$$\phi_M - \frac{Q_{GR}}{C_{IL}} = \chi_{GR} - E_D \tag{3.10}$$

$$Q_{GR} = q\left[\int_{-\infty}^{0} DoS(E)\cdot\left[1-f(E,E_D)\right]dE - \int_{0}^{\infty} DoS(E)\cdot f(E,E_D)dE\right], \tag{3.11}$$

where ϕ_M is the work function of the metal contact, χ_{GR} is the graphene affinity (here set to 4.6 eV), *DoS(E)* is the graphene density of states (defined in Eq. 2.25) and C_{IL} is the capacitance associated to the insulating layer, namely ε_0/t_{IL}. The MIG structure is described taking into account the effect of the graphene quantum capacitance and exploiting the Fermi-Dirac distribution *f(E,E$_D$)* for charges. Once solved, the system of Eqs. 3.10 and 3.11 provides the charge Q_{GR} accumulated in the graphene underneath the metal contact and the displacement (E_D^S=E_D^D=E_D) of the Fermi levels (E_F^S, E_F^D) with respect to the graphene Dirac Point. E_D is then used as Dirichlet boundary condition for the Poisson equation (Eq. 3.1) at the left and right sides of the MC domain in Fig. 3.5(b).

Fig. 3.7 shows the displacement E$_D$ as a function of the work–function ϕ_M of the metal contact for a couple of values of the IL thickness (t_{IL}) in the metal/IL/graphene stack (solid lines) and in the metal/IL/graphene/back–oxide/metal structure (dashed lines). As expected, E$_D$ is null when the metal work–function equals the graphene affinity (vertical grey dashed–dotted line) and, the thinner the IL is, the larger the charge induced in the graphene is, since C_{IL} increases. We see that the presence of the back–oxide (here 20 nm of SiO_2, consistently with what simulated in the following of this section) does not change significantly the amount of the induced charge in the graphene and finally, the value of E$_D$ is almost the same of the previous structure (compare solid and dashed lines). This means that the metal is the only responsible for the doping of graphene for this structure.

The trend of E_D in Fig. 3.7 can be easily understood with the support of the band diagrams reported in Fig. 3.8. Let us consider the case of ϕ_M lower than χ_{GR} (Fig. 3.8(a)); under this condition, in graphene there are many available states as final states; consequently, we assist to an electron transfer from the metal to the graphene, resulting in a graphene enriched of electrons, namely an electrostatic n–doped graphene. The Fermi level is laying above the graphene Dirac Point, so $E_D^{S/D} > 0$ (corresponding to the left side of Fig. 3.7). The opposite situation is sketched in Fig. 3.8(b), taking place when ϕ_M is larger than χ_{GR} and the amount of

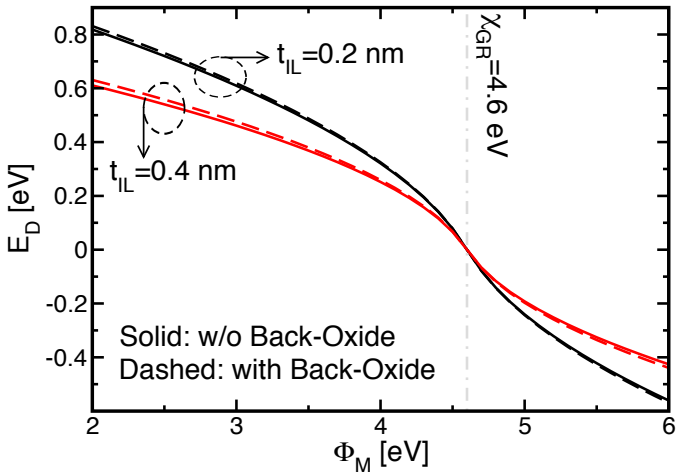

Figure 3.7: Displacement E_D versus the work–function of the S/D metal contact considering (dashed line) or neglecting (solid line) the presence of 20 nm of SiO_2 as back–oxide for a couple of t_{IL}. The grey dashed–dotted line indicates the graphene affinity. The source to back–gate voltage is null.

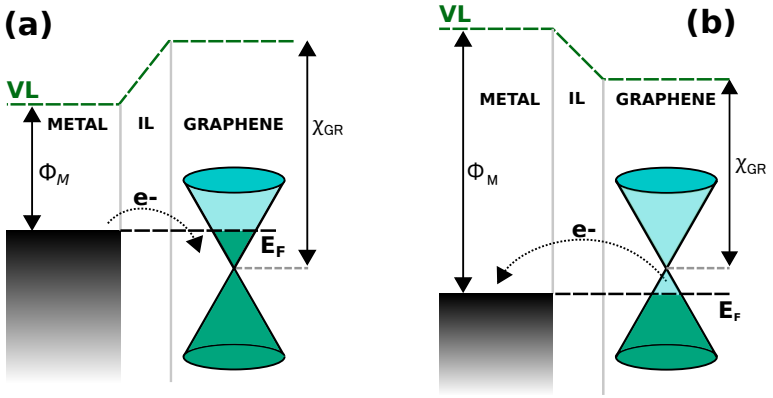

Figure 3.8: Fermi level alignment between the metal contact and the graphene in the case of $\phi_M < \chi_{GR}$ (a) and $\phi_M > \chi_{GR}$ (b). VL represents the vacuum level.

empty states in graphene is much lower than the occupied states in the metal contact. Now, the graphene is enriched of holes, thus $E_D^{S/D} < 0$, resulting in an electrostatically p–doped graphene.

3.3.2 GFETs with electrostatic doping of graphene

After the analysis of the single contact made in Sec. 3.3.1, we move now to the simulation of a complete GFET structure with electrostatically doped S/D regions, that can be compared with the results of GFETs with chemically doped S/D regions.

Figure 3.9 shows the connection between the metal/IL/graphene stack at the source (left side) and at the drain (right side) contacts. Recalling that, at the moment, we are neglecting the effect of the tunneling resistance (both at the source and at the drain side), the displacement between E_F^S and E_F^D corresponds to the extrinsic V_{DS} voltage directly applied between the source and drain metal contacts. In both chemical and electrostatic doping, carriers are injected at the S/D ends of the Monte Carlo simulation domain according to a Fermi–Dirac distribution (Eqs. 3.2 and 3.3) with E_F^S=0 and E_F^D=$-qV_{DS}$, respectively. Unless otherwise stated, we simulated n-

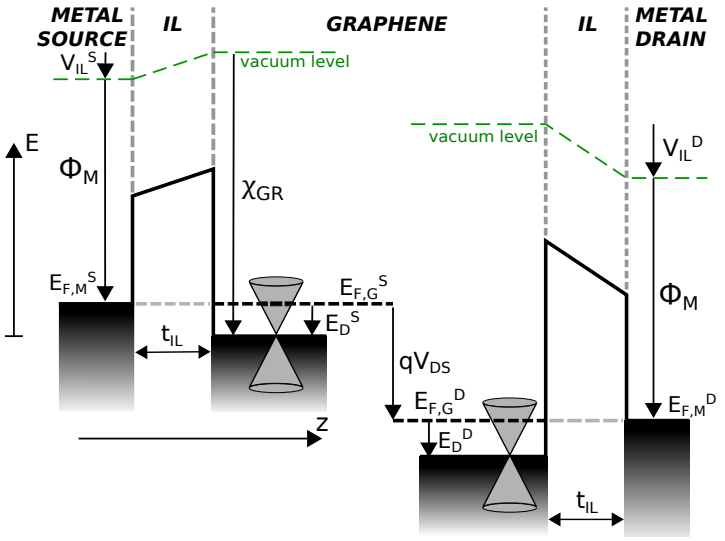

Figure 3.9: Band diagram of the metal/IL/graphene stack at the source side (on the left) and that at the drain side (on the right). Again, for the sake of simplicity, we are neglecting the presence of the back–gate and the tunneling resistance associated to both the insulating layers.

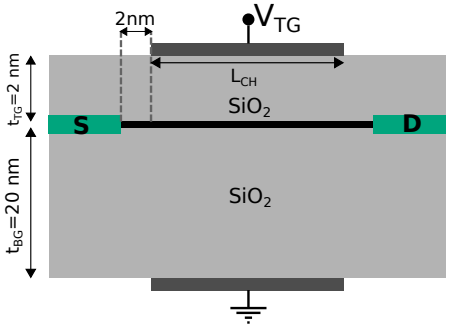

Figure 3.10: Sketch of the simulated GFET showing the assumed parameters.

GFETs with channel length L_{CH}=30 nm, 2 nm underlap (spacing between the S/D and the top–gate), 2 nm SiO_2 as top–oxide (t_{TG}) and 20 nm SiO_2 as back–oxide (t_{BG}). A sketch of the simulated device is reported in Fig. 3.10.

At the equilibrium (V_{DS} = 0 V), for the sake of a fair comparison between the devices in Fig. 3.5 (chemically vs. electrostatically doped S/D regions), the work–function of the S/D metal is tuned in order to induce in the graphene underneath the metal contact the same amount of charge as in the CD case. In fact, as for the CD case, the value of the doping is an input for the Monte Carlo transport simulation, in the ED case, instead, the work–function of the S/D metal contacts is used as an input.

Under these conditions, Fig. 3.11 compares the electron concentration along the transport direction in the two cases; here, for the ED case, we set a work–function of the S/D metal (ϕ_M=2.061 eV) that induces Q_{GR}/q=5·10^{13} cm^{-2} at the S/D, that is the value (dashed orange lines) of the n-doping set in the CD case (black line). Furthermore, again with the sake of a fair comparison, we switch–off the injection in the simulation domain of holes due to the band–to–band–tunneling (BBT) generation. In particular, the BBT model for the ED case is under development at the moment, since the determination of the BBT rate requires a careful estimation of the carrier fluxes in the high electric field regions that feature significant differences

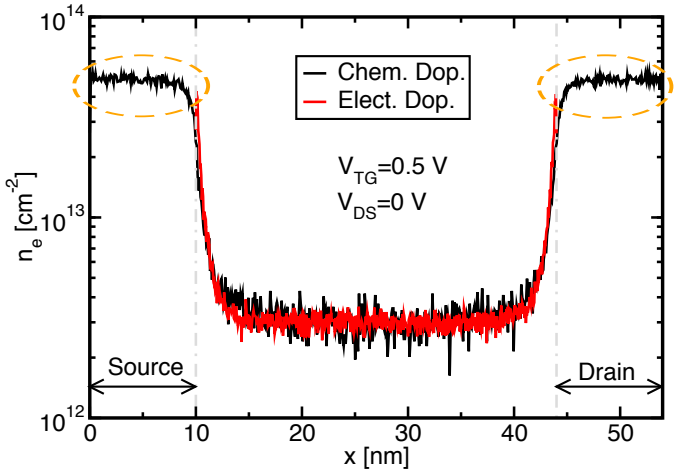

Figure 3.11: Comparison between the electron concentration along the transport direction between the ED case (red line) and the CD case (black line) at $V_{DS} = 0$ V for the device reported in Fig. 3.10 with L_{ch}=30 nm.

in the ED and CD cases. Furthermore, if holes are injected at the S/D contacts, they have a strong influence in the evolution of the potential profile at each iteration of the Monte Carlo, leading to an unfair comparison between ED and CD cases.

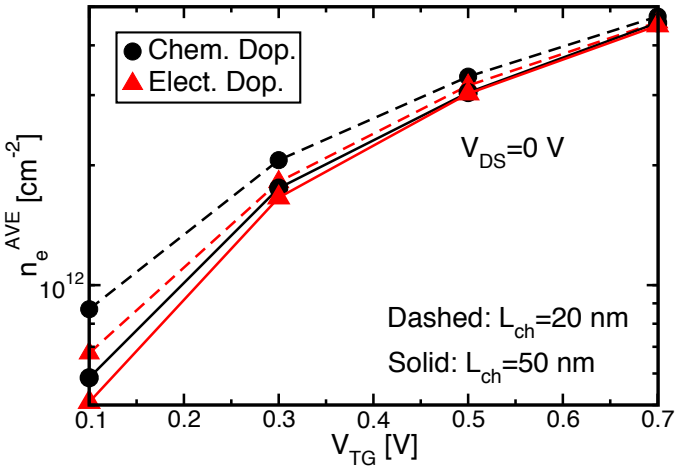

Figure 3.12: Average electron density in the channel as a function of V_{TG} for GFETs with L_{CH}=20 nm (solid lines) and L_{CH}=50 nm (dashed lines) and comparison between chemical (circles) and electrostatic (triangles) doped S/D regions. These simulations have been performed at the equilibrium, so applying a null V_{DS} bias.

Fig. 3.12 compares the average electron density under the top–gate as a function of V_{TG} in the case of CD and ED at the equilibrium (V_{DS}=0 V), for a couple of different channel lengths. As expected, longer the channel is (solid lines, L_{ch}=50 nm), better is the mutual agreement between the curves related to the chemical and the electrostatic doped S/D. This means that the electrostatics of the device is correctly controlled by the gate terminal, while the S/D regions only set the position of the electron Fermi level near the gate edges, verifying the model.

Fig. 3.13 compares the output characteristics of GFETs with CD or ED in the source and drain. For the CD case, simulations including the contribution of BBT are also reported in Fig. 3.13, showing the typical non–saturated behavior [29]. The observed differences are inves-

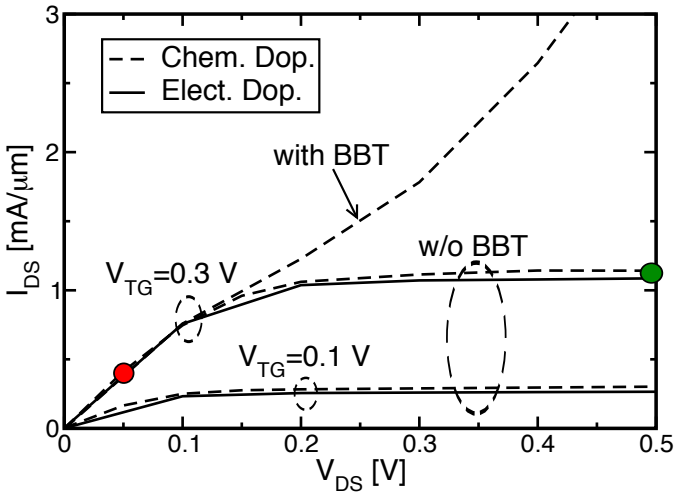

Figure 3.13: I_{DS} as a function of V_{DS} for GFETs with chemical (dashed) and electrostatic (solid) doping. Results including BBT according to the model in [29] are reported at V_{TG}=0.3 V for the case with CD. BBT model for the ED is under development. The red and green circles indicate the V_{DS} bias at which the profiles in Figs. 3.14 and 3.15 are taken.

tigated with the help of Figs. 3.14 and 3.15, showing the electron velocity v_e (a), concentration n_e (b) as well as the potential energy U (c) along the device at V_{DS}=0.05 V and V_{DS}=0.5 V, respectively. First, note the same n_e at the S/D sides in the two devices. At high V_{DS} the agreement between these profiles in the CD and ED cases is worse than at low V_{DS}, explaining the small differences in the resulting output characteristics of Fig. 3.13.

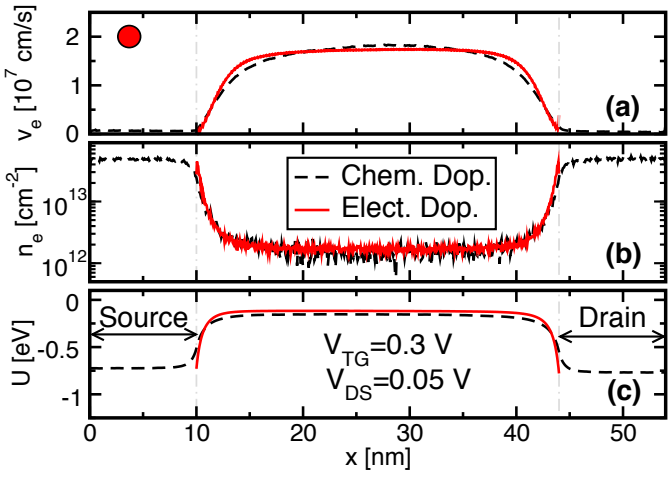

Figure 3.14: Electron velocity (a), density (b) and potential energy (c) along the channel for GFETs with chemical (black–dashed) and electrostatic (solid–red) doping for V_{TG}=0.3 V and V_{DS}=0.05 V. Device parameters: L_{CH}=30 nm, 2 nm underlap, t_{TG}=2 nm (SiO_2) and t_{BG}=20 nm (SiO_2).

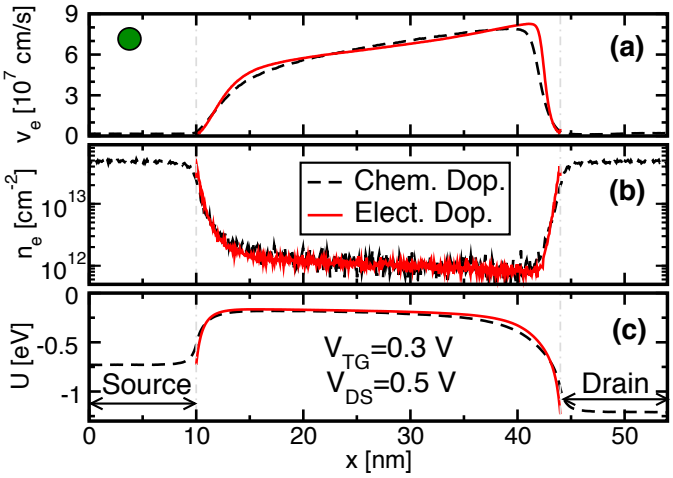

Figure 3.15: The same as in Fig. 3.14 with V_{DS}=0.5 V.

3.4 Modeling of the series resistances

So far we have included the effect of the graphene/metal Schottky contact in the calculation of the GFET electrostatics. In doing that, we have temporarily neglected the effect of the tunneling resistance associated to the insulating layer (IL) when solving the metal/IL/graphene stack. We remind that, under this condition, the calculation of the displacement E_D in the S/D regions (see Eqs. 3.10 and 3.11) is independent of the subsequent Monte Carlo transport simulation. However, the non–negligible tunneling resistance associated to the IL translates into a significant series resistance [101, 102], whose effect should be accounted for at both source and drain sides. To this aim, we decided to include in a unique series resistance (R) the single contributions of (Fig. 3.16):

- the *tunneling resistance* (R_{TUN}), thus the vertical resistance associated to the IL;
- the *graphene resistance* (R_{GRAPH}), hence the horizontal graphene sheet resistance underneath the S/D regions, that includes also the graphene junction resistance due to different charge concentration between the graphene under the metal and in the channel.

Consequently, we considered $R = R_{TUN} + R_{GRAPH}$. In this way, we are able to account for the series resistance in the same manner for both the electrostatically and in the chemically (where $R_{TUN} = 0$ is not considered) doped S/D cases.

Let us focus now on the ED case. To account for the effect of the series resistance, we consider the voltage drop across the insulating layer. The injection levels of the particles in the Monte Carlo domain must be changed at both source and drain sides. This means that, at each iteration of the Monte Carlo transport simulation, we need to shift the Fermi level $E_F^{S/D}$ underneath the metal with respect to the Fermi level of the S/D metal contact by the value of the voltage drop over the series resistance, that of course depends on the current I_{DS} flowing into the device. Figure 3.17 shows the new band diagram of the metal/graphene contact at the source side considering the effect of the series resistance on the electrostatics. Namely, at the source side:

$$E_{F,M} - E_F^S = qRI_{DS}, \tag{3.12}$$

while, at the drain side:

$$E_F^D - E_{F,M} = qRI_{DS}. \tag{3.13}$$

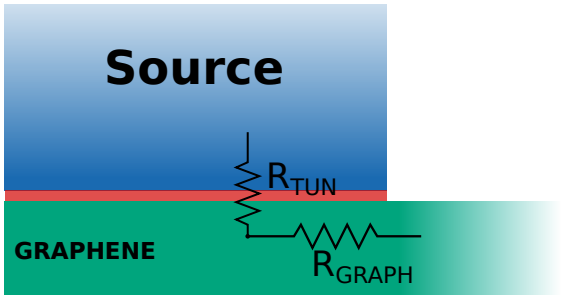

Figure 3.16: Sketch of the metal/graphene contact at the source side showing the vertical tunneling resistance R_{TUN} and the graphene resistance R_{GRAPH} contributing to the access resistance of the device. A similar situation is considered for the drain.

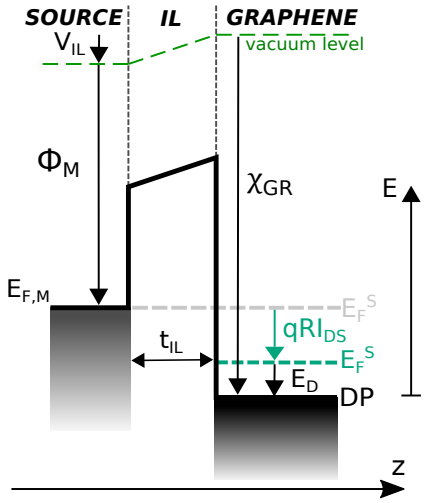

Figure 3.17: Band diagram at the source contact along the section AA' of Fig. 3.5(b) considering the effect of the series resistance. The Fermi level E_F^S in the graphene underneath the contact is now shifted of an amount RI_{DS} with respect to the metal Fermi level $E_{F,M}$, differently from Fig. 3.9.

Hence, Eq. 3.10 becomes:

$$\phi_M - \frac{Q_{GR}}{C_{IL}} = \chi_{GR} - E_D - qRI_{DS}, \tag{3.14}$$

while Eq. 3.11 is still valid. Clearly, shifting the Fermi levels at the S/D regions requires also to modify the term E_F^i in Eqs. 3.2 and 3.3, considering Eqs. 3.12 and 3.13 [1].

It is easy to understand that now the charge transport directly impacts the Dirichlet boundary conditions at the S/D terminals (namely the displacement $E_D^{S/D}$) at each Monte Carlo iteration for the ED case. To cope this mutual dependence between the electrostatics and the carrier transport, it is necessary to solve a self–consistent loop between the MC transport and the electrostatic solver at S/D, that can possibly lead to instability issues. In particular, Fig. 3.18 shows that, without introducing any damping procedure, the simulation does not converge (solid line). For this reason, the instantaneous current (estimated as an average along the channel of the product between the carrier concentration and the average carrier velocity) used to calculate the voltage drop across the S/D stack requires a proper estimation. To avoid oscillations,

[1] Concerning chemical doped S/D regions instead, since it is not needed to solve the MIG stack at the contacts, it is enough to shift the Fermi levels in Eqs. 3.2 and 3.3 (see Fig. 3.19).

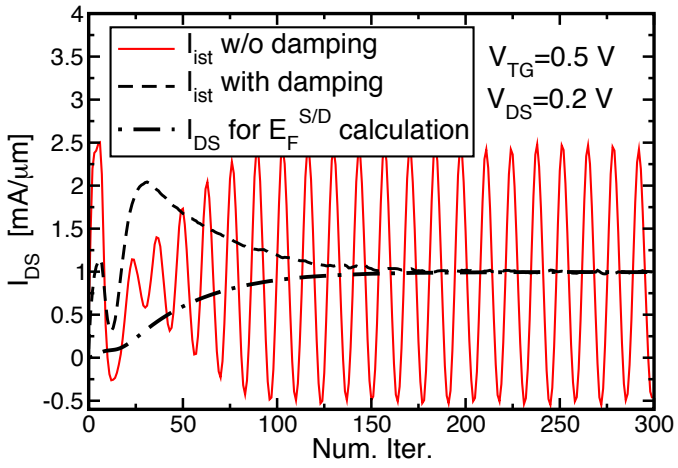

Figure 3.18: Example of I_{DS} evolution during the MC simulation of a GFET with series resistance. Without the damping procedure, the simulation does not converge (solid line). The damping algorithm solves the problem (dashed line). The dash–dotted line is the current value used in the algorithm to calculate the voltage drop across the series resistances at each iteration.

we limit the variations of the RI_{DS} value to less than 1% between two MC iterations. The dash–dotted line in Fig. 3.18 shows the current value used to calculate RI_{DS}, while the dashed line is the I_{DS} obtained at every iteration, that now converges thanks to the proposed damping scheme. Although the assumed maximum variation could seem a strong limit to the current evolution, we verified that the MC simulator is anyway capable to converge to a reliable value of the final current (see also Figs. 3.21 and 3.22, where the dashed lines are obtained without introducing the damping scheme).

Moving now to the simulations that account for the effect of the series resistance, Fig. 3.19 shows the potential energy profile along a CD GFET for V_{TG}=0.5 V and V_{DS}=0.5 V with R=0 (dashed line) and with R=100 $\Omega\mu$m (solid line). Following Eqs. 3.12 and 3.13, to account for the effect of series resistance, E_F^S is reduced by the amount RI_{DS}, while E_F^D is increased by the same amount. This reduces the intrinsic voltage drop across the channel:

$$V_{DS}^i = V_{DS} - 2RI_{DS}, \tag{3.15}$$

as clearly shown by Fig. 3.19.

Furthermore, by introducing the series resistances, the injection barrier at the source side is increased, changing also the intrinsic top–gate bias (V_{TG}^i) experienced by the graphene channel. At this regard, Fig. 3.20 shows the energy potential profile obtained for a simulation imposing V_{TG}^i=V_{TG}−RI_{DS}, V_{DS}^i and R=0 (dashed line). The difference between this simulation and another one that, instead, considers V_{TG}, V_{DS} and R=100 $\Omega\mu$m (solid line) is rather constant over x. Hence, only a rigid shift is present between the two curves, namely Δ_S=Δ_{Ch}=qRI_{DS}. It is interesting to note that Δ_{TOP} in Fig. 3.19 is smaller than Δ_{Ch}=Δ_S in Fig. 3.20; this demonstrates that R not only reduces V_{DS}^i, but also increases the effective potential energy barrier ($\Delta_S - \Delta_{TOP}$) at the injection point, as it should be, namely:

$$V_{TG}^i = V_{TG} - RI_{DS}. \tag{3.16}$$

Note that in Figs. 3.19 and 3.20 simulations of a CD GFET have been shown. However, very similar results have been obtained also for the ED case (not shown because of the redundancy of the results).

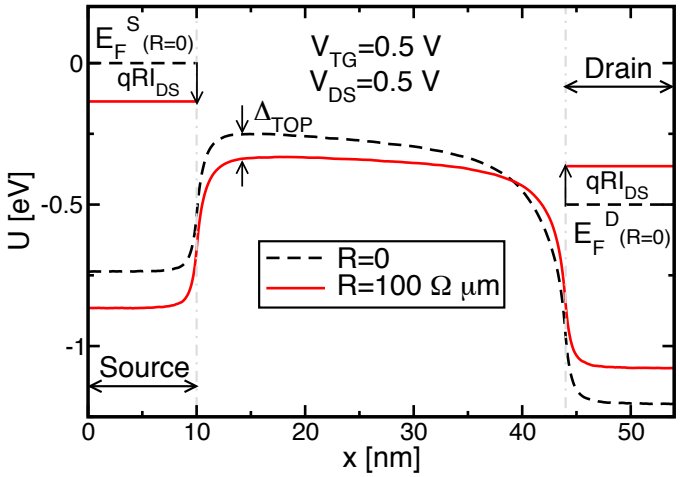

Figure 3.19: Potential energy profile along the GFET (CD) without (dashed black) and with (solid red) the series resitances. The Fermi levels in the S/D regions (E_F^S, E_F^D) are reported (dashed black: no R; solid red: with R). The shift of the Fermi levels in the source and in the drain regions reduces the intrisc V_{DS}^i across the channel.

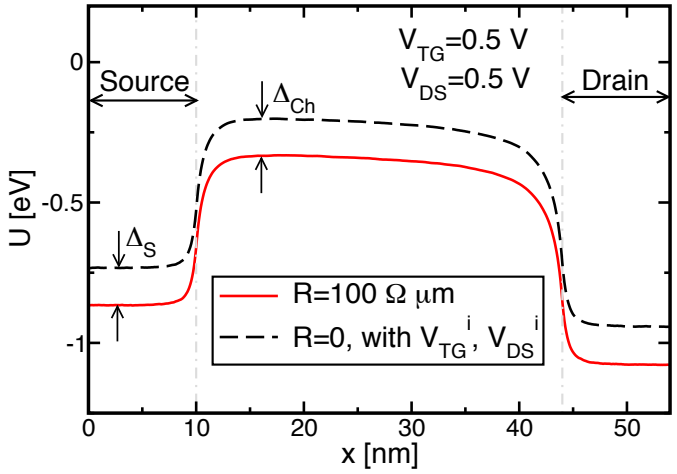

Figure 3.20: Potential energy profile along the GFET (CD). Solid red: simulation with V_{DS}, V_{TG} and the series resistance. Dashed black: simulation with the intrinsic biases V_{TG}^i=V_{TG}−RI_{DS}, V_{DS}^i=V_{DS}−$2RI_{DS}$ and without the series resistance. Δ_S=Δ_{Ch} demonstrates the rigid shift between the two potential energy profiles, since E_F^S and E_F^D are shifted of qRI_{DS} in the two simulations.

In order to verify the implemented model, Fig. 3.21 compares the output characteristics in the CD case with (solid lines) and without (dashed lines) the series resistance. In the figure it is also reported the case where R is introduced as a lumped element (symbols), by transforming the $I_{DS}(V_{DS}, V_{TG})$ plane through look–up tables [88]. This corresponds to stretch the output characteristics from the (V_{DS},V_{TG}) plane to the (V_{DS}^i,V_{TG}^i) plane through Eqs. 3.15 and 3.16. Switching–off the BBT tunneling and hole injection (Fig. 3.21(a)), a really good agreement between the method of [88] and our implementation (where R is introduced in the MC loop) is obtained, also considering different values of the series resistances. The agreement is good also when BBT is activated (Fig. 3.21(b)), confirming the correctness of our modelling approach, that has the advantage of saving the simulation time needed to construct the look–up tables (at

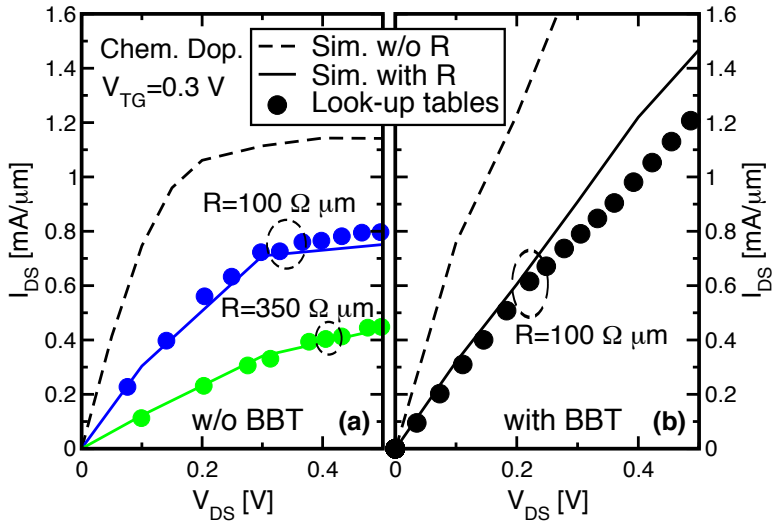

Figure 3.21: I_{DS} as a function of V_{DS} for a GFET with chemical doping without (a) and with (b) the contribution of BBT. Results without (dashed lines) and with the series resistance (solid lines) are compared. Symbols are the data without R after the trasformation of the plane (V_{DS}, V_{TG}) to include the series resistance potential drop through post–processing of simulated data (as proposed in [88]).

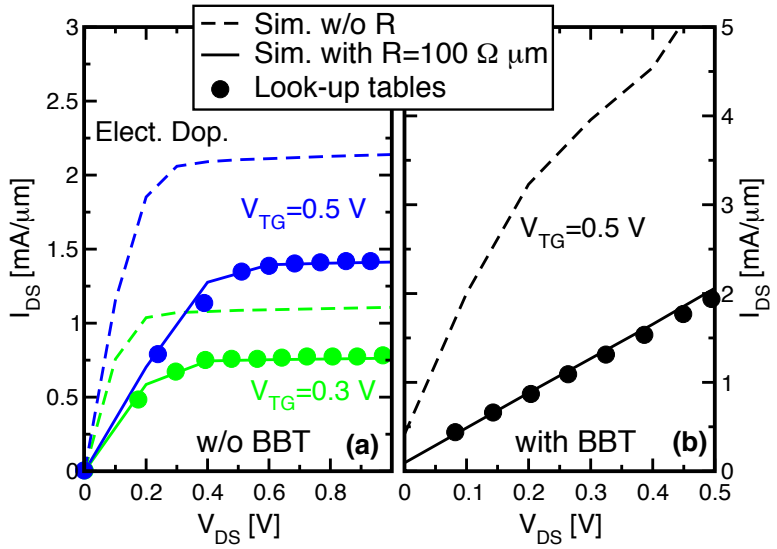

Figure 3.22: I_{DS} as a function of V_{DS} for a GFET with electrostatic doping without (a) and with (b) the contribution of BBT in the ED case. Results without (dashed lines) and with the series resistance (solid lines) are compared. Symbols are the data without R after the trasformation of the plane (V_{DS}, V_{TG}) to include the series resistance potential drop, as proposed in [88].

least a factor of two in time if a coarse table is used).

We verified the correctness of the model also in the case of electrostatic doped S/D regions (Fig. 3.22). In Fig. 3.22(a), when BBT is not included, the Monte Carlo simulation including series resistance (solid lines) are similar to the values obtained by the look–up–tables, also for different V_{TG} voltages. When BBT is activated (Fig. 3.22(b)) the good agreement is still valid, but the Monte Carlo simulator is estimating a non-negligible current at null V_{DS}. This is clearly an error, and it demonstrates how the model describing the BBT (see Sec.3.2) is not valid in the

case of the electrostatic doped S/D regions, where a high electric field is present at the border of the simulation domain. Hence, the BBT model must be further developed to describe the BBT also in the ED case.

3.5 Characterization of metal/graphene contact resistance

During this activity, we investigated also on reliable techniques able to characterize the different contributions to the overall series resistance linked to metal/graphene contacts. This is of fundamental importance, in order to fully understand and fairly model the impact of this extrinsic parameter on the GFET performance. In particular, the current section is dedicated to the experimental characterization of the metal/graphene contact resistance, through the application of the end–contact method to transfer length method (TLM) structures, and it collects the most significant results deriving from the measurements done at the University of Siegen, in the framework of the collaboration between the two universities.
The end–contact method has been first proposed in [103] and it has been largely used to characterize the contact resistance to Si, to III-V materials [103, 104] and, more recently, to graphene [105, 106]. In the beginning of this section, we will illustrate the theoretical background behind the definition of the front(end)–contact resistance and the transmission line model, commonly used to describe the graphene/metal contact (Sec. 3.5.1). Then, after a brief summary on the structural parameters of the characterized TLM samples (Sec. 3.5.2), in Sec. 3.5.3 we analyze the results of the measurements and how, under certain biasing conditions, the exploited model is not anymore accurate to describe the metal/graphene stack, finally giving a possible explanation and discussing the conditions under which the technique can provide reliable results.

3.5.1 End–contact method applied on TLM structures

Figure 3.23(a) shows the sketch of a metal/graphene contact of and the so–called transmission line model, proposed first by Berger [107] to describe the metal/semiconductor contacts. Also for the metal/graphene contacts, the potential profile in the graphene is influenced by both the specific contact resistivity ρ_c and the sheet resistance under the contact R_{SK}.

Following the transmission line theory [107, 108]:

$$\frac{dI(x)}{dx} = \frac{V(x)W}{\rho_c} \tag{3.17}$$

$$\frac{dV(x)}{dx} = \frac{I(x)R_{SK}}{\rho_c}, \tag{3.18}$$

where x is the spatial variable whose the zero–reference is the vertical edge of the metal graphene contact (see Fig. 3.23(a)), $V(x)$ and $I(x)$ are the voltage and current profile along x, respectively, while W is the width of the contact. Solving Eqs. 3.17 and 3.18, we end–up with the expression of the potential as a function of the spatial variable, namely:

$$V(x) = \frac{I\sqrt{\rho_c R_{SK}}}{W} \frac{\cosh\left[(L_{CON} - x)/L_{TK}\right]}{\sinh\left(L_{CON}/L_{TK}\right)}, \tag{3.19}$$

where I is now the current flowing through the contact, L_{CON} is the contact length, while L_{TK} is the transfer length, that is smaller than the contact length (see Fig. 3.23(b)) and characterizes the current crowding occurring at the metal/graphene contact. The so–called front–contact resistance can be easily found by imposing $x = 0$ in Eq. 3.19, so:

$$R_{CF} = \frac{V(x=0)}{I(x=0)} = \frac{\sqrt{\rho_c R_S K}}{W} \coth\left(L_{CON}/L_{TK}\right). \tag{3.20}$$

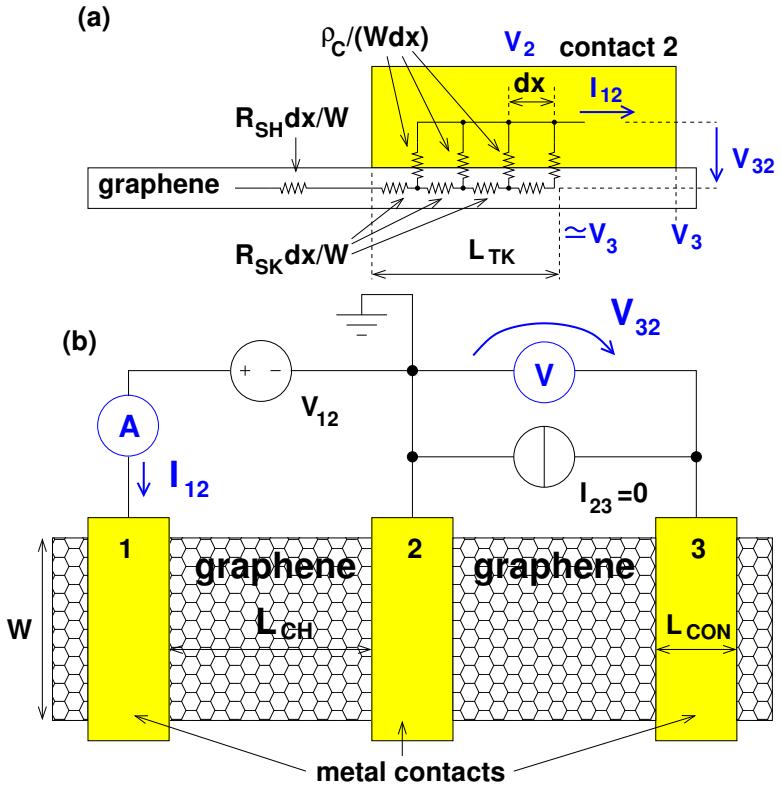

Figure 3.23: (a) Circuit schematic of the transmission line model for the metal–graphene contact. (b) Experimental setup and TLM structure used for the series resistance measurements.

Figure 3.23(b) shows the transfer length method (TLM) structure and the experimental setup used to study the graphene–metal contact resistance. While forcing the voltage V_{12}, the current I_{12} is measured between contacts 1 and 2 and the total resistance R_T of the back–gated transistor is obtained as [103]:

$$R_T = \frac{V_{12}}{I_{12}} = \frac{R_{SH} L_{CH}}{W} + 2R_{CF}. \tag{3.21}$$

Anyway, a complete TLM structure is made of a series of GFET devices with an increasing channel length L_{CH} (see Sec. 3.5.2). By measuring the current I_{12} as a function of V_{12} for the different devices (see Fig. 3.24(a)), we can extract R_T for different graphene lengths simply evaluating the slope of the curves. The front–contact resistance R_{CF} and the sheet resistance R_{SH} of the graphene channel are finally obtained by means of a linear fit of the measurements in the plane $R_{TOT}(L_{CH})$, as done in Fig. 3.24(b); in particular, the slope and the intercept of the linear fit with the y–axes are correlated to the R_{SH} and R_{CF}, respectively, through Eq. 3.21.

The end–contact resistance is instead defined as the resistance measured at $x = L_{CON}$, namely:

$$R_{CE} = \frac{V_{32}}{I_{12}} = \frac{V(x = L_{CONT})}{I(x = 0)} = \frac{\rho_c}{L_{TK} W \sinh\left(\frac{L_{CON}}{L_{TK}}\right)}. \tag{3.22}$$

The technique used to characterize experimentally R_{CE} consists in measuring I_{12}, while imposing simultaneously a zero current between contacts 2 and 3 (see Fig.3.23(b)); in the meantime, the potential drop V_{32} across the graphene–metal contact is also measured.

Figure 3.25 shows the linear trend of the measured V_{32} as a function of I_{12} for the same devices reported in Fig. 3.24. Since the slope of the $V_{32}(I_{12})$ curve represents the value of the end–contact resistance, the independence on L_{CH} obtained in Fig. 3.25 indicates that the

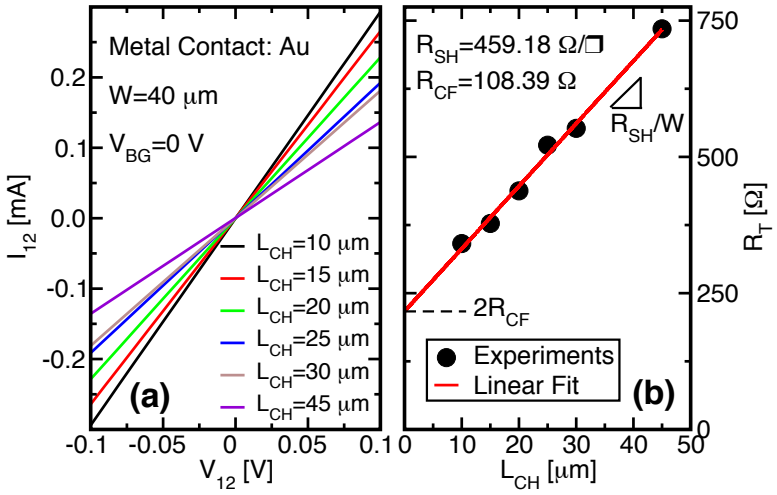

Figure 3.24: (a) Current measured through the graphene channel of the TLM structure exploiting Au contacts. (b) Total resistance versus L_{CH} obtained in a TLM structure with Au contacts. The linear fit allows to extract the front–contact resistance R_{CF} and the sheet resistance R_{SH} of graphene.

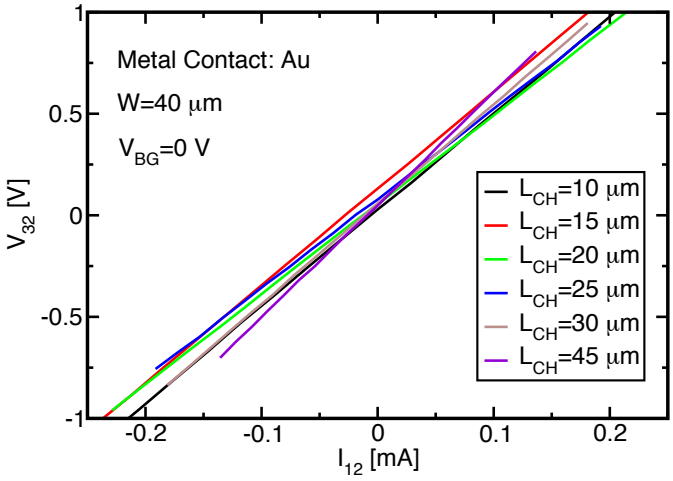

Figure 3.25: Voltage measured at the end–contact through the experimental setup of Fig.3.23(b). Note the linearity of the characteristics and the independence of L_{CH}.

resistance associated to the contact is not varying over the TLM structure, hence, all the contacts show the same R_{CE}, as expected.

Following [103, 104], since R_{CF} can be modeled with the transmission line model (see Fig. 3.23(a)), being the potential profile under the contact determined by the specific contact resistivity ρ_c and the sheet resistance R_{SK} of graphene under the metal, it is possible to correlate R_{CF} and R_{CE} with ρ_c and R_{SK} using the following equations [103]:

$$\frac{R_{CF}}{R_{CE}} = \cosh\left(\frac{L_{CON}}{L_{TK}}\right) \tag{3.23}$$

$$L_{TK} = \sqrt{\rho_c / R_{SK}} \tag{3.24}$$

Therefore, by measuring R_{CF} and R_{CE}, it is possible to extract R_{SK}, L_{TK} and ρ_c for the specific graphene–metal contact under study by solving Eqs. 3.22, 3.23 and 3.24.

3.5.2 TLM samples

As anticipated in Sec. 3.5.1, a complete TLM structure is built as a series of many GFET devices featuring different channel lengths. Figure 3.26 is a microscope image of a general TLM structure, used for the analysis reported in Sec. 3.5.3. In detail, the GFET on the left side of the figure measures the shortest channel length, equal to 5 μm in the design mask, while the device on the right is the longest one with L_{CH}=50 μm. The channel variation between adjacent devices is 5 μm (or 8 μm for other samples, see for instance Fig. 3.27 where L_{CH}=8 μm).

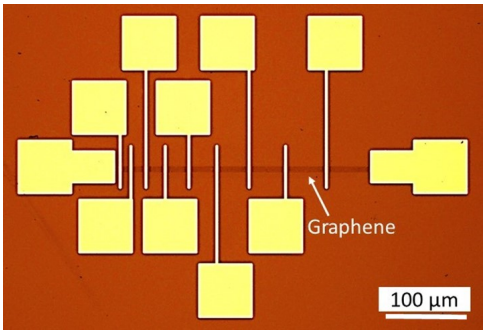

Figure 3.26: Microscope image of the measured TLM structure; the arrow indicates the graphene channel, while the yellow pads are the source and drain contacts of the different GFETs forming the complete TLM. The space between contacts (L_{CH}) varies from 5 μm to 50 μm (from left to right) with a 5 μm increase between adjacent channels. The channel width (W) is 5 μm in this particular structure. Other structures with W varying between 4 μm and 40 μm have been measured (see next figures).

Furthermore, devices consist of back–gated graphene channel, whose widths (W) varies from 4 to 40 μm. TLM structures with various metal contacts, i.e. gold (Au), nickel (Ni) and nickel/gold stack (Ni/Au, with Ni in contact with graphene) to chemical vapor deposited monolayer graphene have been fabricated (more details on the devices and their fabrication are provided in [81]). Anyway, the work–functions of the exploited metals (≃5.1 eV for both Au and

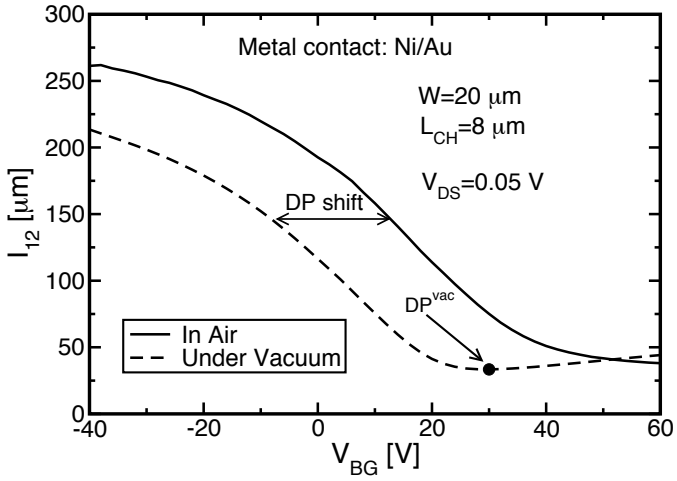

Figure 3.27: Comparison between typical current versus V_{BG} curves of a device exploiting the Ni/Au stack contacts measured in air (solid line) and under vacuum (dashed line). Because of the graphene charging due to the air, the Dirac Point (DP) is shifted from ≃30 V to very high V_{BG} bias (it is located above 60 V).

Ni [109]) are higher than graphene affinity, hence, the graphene underneath the metal contact will be electrostatically p–doped [99, 110] (see Fig. 3.8(b)).

The proper functioning of every single device, as well as the corresponding position of the Dirac Point (fundamental in order to determine at which bias the carrier type involved in the transport is changing), are verified by measuring the source–drain current (I_{12}) during a back–gate voltage (V_{BG}) sweep. As an example, Fig. 3.27 shows the trend of the transfer characteristic for a GFET with L_{CH}=8 μm and W=20 μm measured in air (solid line) and under vacuum (dashed line). The sample has the Ni/Au stack contacts and 85 nm of SiO_2 as back–oxide. As visible, the measurement in air is not showing the minimum conductivity point (corresponding to the Dirac Point) typical of GFET devices, because the air has a strong impact on graphene charging, that shifts the Dirac Point (doping of the graphene through humidity [111, 112]). In fact, the particles of water trapped by graphene shift the Dirac Point from of the measurement under vacuum, to very high V_{BG} bias. As it can be noticed, also the measurement under vacuum shows a Dirac Point shifted towards positive values $V_{DP} \simeq$30 V. This is probably due to the effect of the post processing Rapid Thermal Annealing (RTA) the sample underwent, as discussed in [15].

3.5.3 Measurement results and failure of the transmission line model

We start with an investigation on the front–contact resistance and of the sheet resistance. Figure 3.28 shows R_{SH} (black circles, left axis) and R_{CF} (red triangles, right axis) versus W obtained from TLM structures with Au contacts when applying a zero back–gate bias (V_{BG}). As expected, R_{SH} is almost constant since it is linked to the quality of the graphene sheet and in principle independent of the W, while R_{CF} scales inversely with W ($R_{CF} \propto 1/W$).

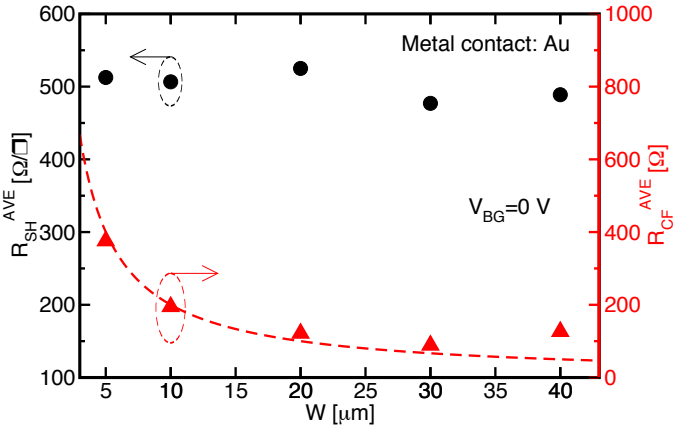

Figure 3.28: Sheet resistance (black circles, left axis) and front–contact resistance (red triangles, right axis) versus W of samples with Au contacts. The reported R_{SH} and R_{CF} values are averaged between measurements made on different TLM structures. The rather constant R_{SH} and the R_{CF} inversely proportional to W (dashed line) confirm the reliability of the measurements.

In Fig. 3.29 the dependence on the back–gate voltage is analyzed; both R_{CF} (a) and R_{SH} (b) increase with increasing V_{BG} [81, 106], as expected also looking to the $I_{12}(V_{BG})$ characteristic reported in Fig. 3.27, that shows a Dirac Point above 60 V; in fact, by increasing the V_{BG} bias from large negative values to large positive ones, we are approaching the Dirac Point, where the graphene charge density is reduced to a minimum value, leading to a less conductive graphene. Moreover, we see that R_{CF} shows a stronger V_{BG} dependence than R_{SH}.

Concerning the measurements of the end–contact resistance, Fig. 3.30 reports R_{CE} versus W obtained at V_{BG}=0 V for samples exploiting different metal contacts; Au contacts (circles) show

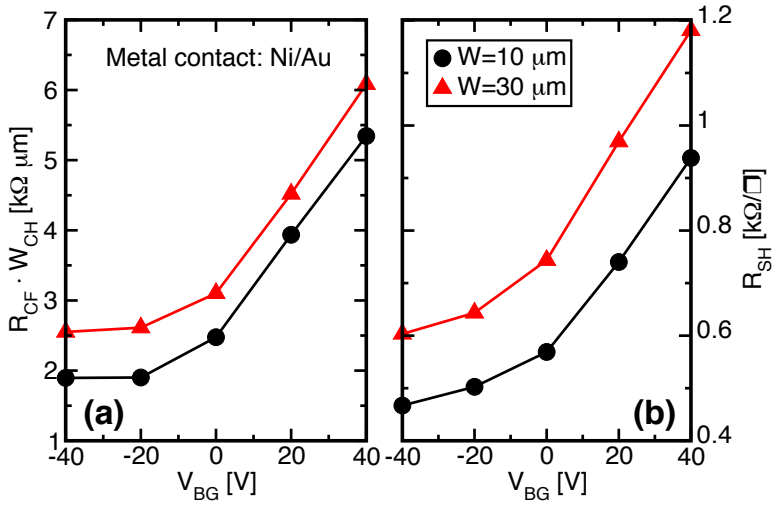

Figure 3.29: Front–contact resistance (a) and sheet resistance (b) as a function of V_{BG} for TLM structures with different W and Ni/Au contacts. By increasing the V_{BG} value, the hole charge accumulated in the graphene is reduced (Dirac Point is larger than 60 V, see Fig. 3.27), thus increasing R_{SH}. R_{CF} shows a similar trend as R_{SH}.

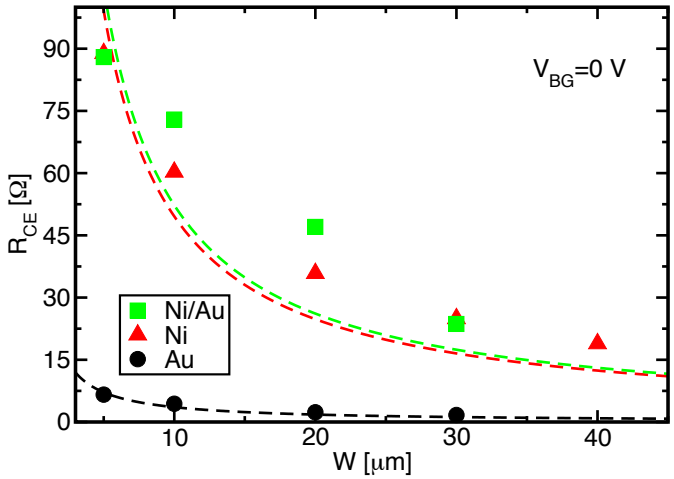

Figure 3.30: End–contact resistance as a function of W of samples with Au (black circles), Ni contacts (red triangles) and exploiting the Ni/Au stack (green squares). R_{CE} is obtained averaging on measurements made on different TLM structures. The dashed lines are guides for the eye representing the W^{-1} behaviour.

a smaller R_{CE} than Ni (triangles) and Ni/Au contacts (squares, we recall that Ni is in contact with graphene), hence the potential drop across Ni–graphene is larger than in Au–graphene. As expected, also R_{CE} scales with W, as R_{CF} (see Fig. 3.28).

Regarding the dependence of R_{CE} on the V_{BG}, Fig. 3.31 compares the trend of R_{CE} and R_{CF} (see also Fig. 3.29(a)) as a function of V_{BG} (black circles). While, as already shown, R_{CF} increases for increasing V_{BG}, R_{CE} is instead independent of V_{BG}, as reported also in [106]. This is a clear signal of the independence of V_{BG} by the potential under the contact (V_3 in Fig. 3.23(b)) on V_{BG}; this means that the potential under the contact is essentially fixed by the metal (Fermi level pinning, see also the simulation results in Sec. 3.3.1). As a consequence, a fixed hole density is also expected under the contact.

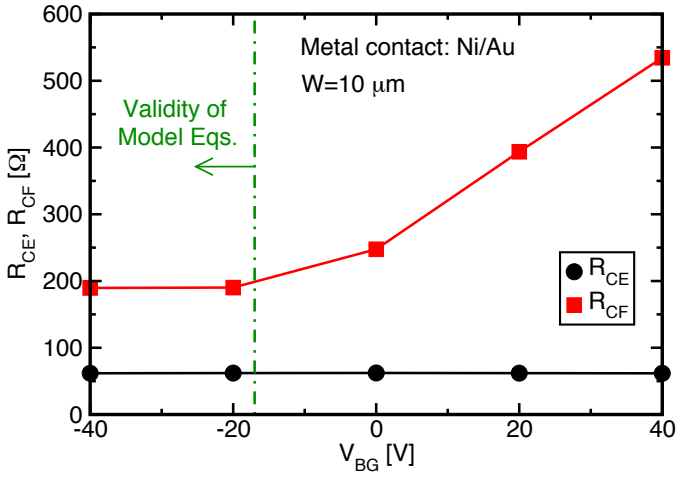

Figure 3.31: End–contact resistance (black circles) and front–contact resistance (red squares) as a function of V_{BG} of a sample with Ni/Au stack contacts for a TLM structure with W=10 μm. Note the V_{BG} indipendence of R_{CE}, while R_{CF} largely increases for V_{BG} values closer to the Diract Point.

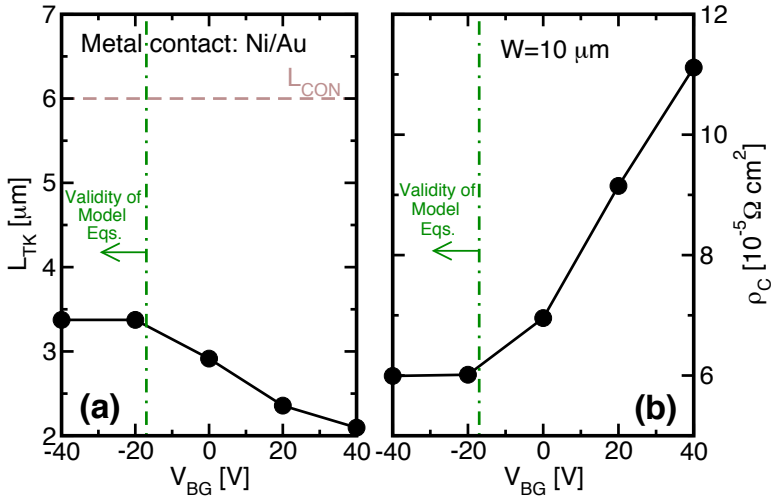

Figure 3.32: Transfer length (a) and specific contact resistivity (b) calculated by applying Eqs. (3.22) and (3.23) to the R_{CE} and R_{CF} values of Fig. 3.31. Note how L_{TK} and ρ_c are essentially constant for $V_{BG} \leq$-20 V, while largely vary for $V_{BG} >$-20 V.

We used Eqs. (3.22)–(3.24) to extract R_{SK}, L_{TK} and ρ_c from the measurements in Fig. 3.31. Fig. 3.32 shows L_{TK} (a) and ρ_c (b) versus V_{BG}. For $V_{BG} \leq -20$ V, L_{TK} and ρ_c are rather independent of V_{BG}, while for $V_{BG} > -20$ V, the two quantities are strongly varying. A similar behavior is shown for R_{SK} in Fig. 3.33 (black circles). This would suggest that, for $V_{BG} > -20$ V, the hole concentration under the contact is largely changing. However, this is inconsistent with the picture discussed above, hence with R_{CE} values independent of V_{BG}. Furthermore, ρ_c is usually associated to electron tunneling between metal and graphene, hence the ρ_c variation with V_{BG} (Fig. 3.32(b)) suggests a V_{BG} dependence of the potential under the contact, but this is again in contrast with a contact electrostatics fixed by the metal.

These inconsistencies suggest the *failure of the transmission line model to describe the front–contact* R_{CF}, at least for $V_{BG} > -20$ V. Indeed, for this biasing, the channel hole density decreases, creating a p-p^+ junction near the contact edge. This typically induces a further series

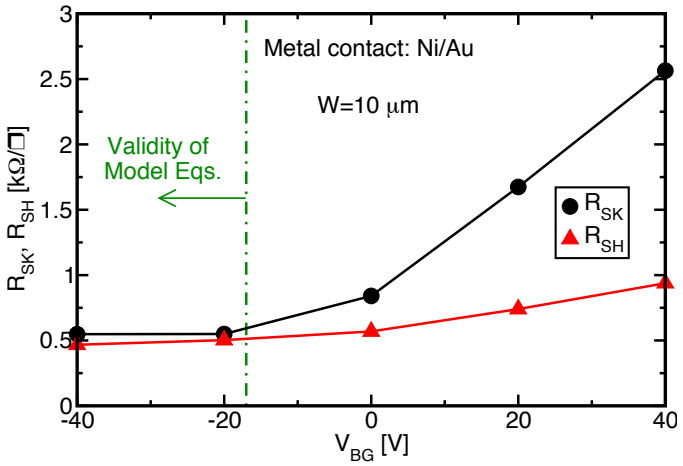

Figure 3.33: Comparison between the sheet resistance under the contact (R_{SK}, black circles) obtained from Eq. (3.24) and the sheet resistance in the graphene channel (R_{SH}, red triangles) of the device reported in Fig. 3.31. For $V_{BG} \leq -20$ V, $R_{SH} \simeq R_{SK}$ suggesting that there is no variation of the charge concentration between the channel and the graphene under the contact.

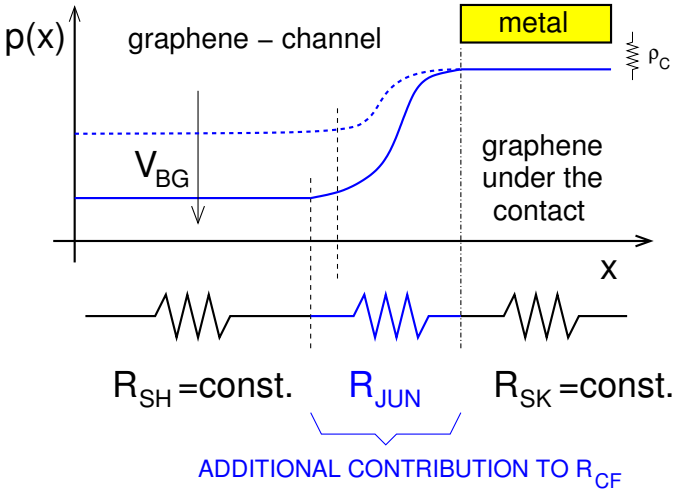

Figure 3.34: Sketch of the hole concentration of graphene in the proximity of the contact. R_{JUN} represents the resistance due to the p-p^+ junction in graphene that should be considered as an additional contribution to R_{CF}. For large negative values of V_{BG}, the p-p^+ junction disappears and R_{JUN} becomes negligible, so R_{CF} can be described by the transmission line model under the contact (see Fig. 3.23(b)) [106].

resistance contribution (R_{JUN}) that adds to R_{CF}, schematically reported in Fig. 3.34 [98]; by focusing on the blue solid line (generally referred here to $V_{BG} > -20$ V, see the vertical dashed dotted line of Figs. 3.31–3.33) and moving along the x axis on the figure, the hole concentration in graphene starts to rapidly increase in proximity of the contact region, causing the formation of the junction. The commonly used transmission line model does not account for this additional resistive contribution, generating errors in the extracted parameters. This is confirmed by Fig. 3.33, that shows the extracted R_{SK} becoming larger than R_{SH} for $V_{BG} > -20$ V, while it should be the contrary since the hole density in the channel is reducing with increasing V_{BG}.

For $V_{BG} \leq -20$ V, instead, the graphene channel is strongly p–doped, see the dashed blue line in the sketch of Fig 3.34. Hence, there is no evident difference between the hole concentration

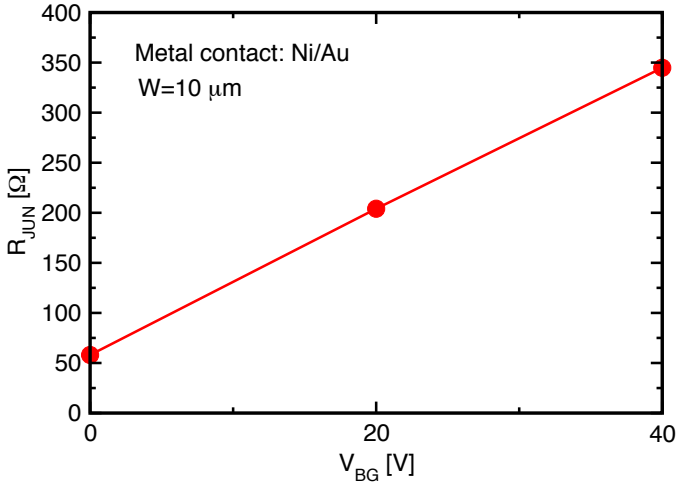

Figure 3.35: Estimation of the junction resistance R_{JUN} by means of the measurements reported in Fig. 3.31.

in the channel and under the contact. In these conditions, R_{CF} is independent of V_{BG} as R_{CE} (see Fig. 3.31) and the extracted R_{SH}, L_{TK} and ρ_c are constant. In particular, R_{SK} is very close to R_{SH} (Fig. 3.33) and this supports the picture of similar p concentration in the channel and under the contact (assuming similar hole mobility). In this V_{BG} range, we consider reliable the results obtained with the model equations and we extract $R_{SK}\simeq 500\ \Omega/\square$, $\rho_c\simeq 6\cdot 10^{-5}\ \Omega\text{cm}^2$ and $L_{TK}\simeq 3.5\ \mu$m for the Ni/Au contact.

Following the reasoning proposed above, Fig. 3.35 provides the trend of the junction resistance R_{JUN} directly extracted from the measurements reported in Fig. 3.31.

Although this analysis has been shown for the Ni/Au metal contacts, similar results are obtained also in case of the other metal contacts (not shown).

3.6 Conclusion

In this chapter we initially presented the state–of–the–art of the Monte Carlo (MC) simulator dedicated to GFET devices developed at the University of Udine. Then, we moved to the extension of the semi–classical transport model, including the possibility to simulate GFETs with electrostatically doped source (S) and drain (D) regions. To this aim, we developed a simple 1D physics–based model for the metal/graphene Schottky contact. Once solved the electrostatics of the metal/IL/graphene stack, Dirichlet boundary conditions can be applied at the ends of the graphene channel before the MC transport simulation, which is finally predicting similar current values for GFETs with chemically and electrostatically doped S/D regions having the same S/D charge density. Anyway, we want to highlight that, because of technological limitations (e.g. the difficulties in doping the graphene), the two solutions may be not equivalent in actual experimental devices.

Moreover, we presented an efficient implementation of the S/D series resistance directly in the self–consistent loop of the Monte Carlo model. The model has been validated comparing the results of the MC simulations including the series resistance in the self–consistent loop against results obtained following the approach base on look–up–tables, which requires a post–processing of several simulation data. The obtained good mutual agreement confirms the correctness of our technique, that has the important advantage in saving time needed to construct the look–up–tables.

The last section of the chapter is focused on the experimental characterization of the graphene/metal contact resistance, where the so–called end–contact resistance technique has been used to extract the different contributions of the series resistance. We have shown how the exploited transmission line model, generally used to characterize series resistance, fails to correctly describe the graphene/metal contact under certain biasing conditions. We found a possible explanation in the additional graphene junction resistance, which becomes relevant in that biasing range dominating the dependence of the contact resistance and we provided the conditions under which the technique could considered reliable. This provides a reliable characterization technique that can help in calibrating the proposed GFET model, allowing for realistic predictions of the GFET performance.

Chapter 4

Physics–Based Modelling of the Graphene–Base–Transistor

4.1 Introduction

This chapter is focused on the Graphene–Base–Transistor (GBT), a recent device concept based on graphene proposed for high frequency applications [22]. The chapter is organized as follows. Section 4.2 illustrates the structure and the operation principle of the GBT. In Sec. 4.3, we report the details of the developed electrical model to predict the Direct Current (DC) and Radio Frequency (RF) performance of GBT devices, from the preliminary version of the model able to simulate the simpler GBT structure, to an improved one that includes the detrimental space charge effects occurring at high current levels, to analyze their impact on the maximum achievable cutoff frequency. The role of series resistances, discussed in Chapt. 3 for Graphene-Field-Effect-Transistors, is analyzed also here showing their influence on the unity power gain of GBTs. Finally, we validate our electrical model against the results obtained through a Non–Equilibrium–Green–Function (NEGF) based simulator, developed at the University of Bologna [24, 25, 113]. Furthermore, in Sec. 4.4, we briefly discuss the use of the electrical model as reference for the calibration of the compact model for GBT devices developed at the University of Bordeaux [114]. Section 4.5 presents instead the Monte Carlo simulator, that has been developed in order to investigate the electron transport in GBTs and, in particular, the impact on the common–base–current gain of electron backscattering in the base–collector insulator. Section 4.6 collects simulations exploring the GBT design space, giving guidelines for the optimization of the principal GBT RF figures of merit. Section 4.7 is finally focused on the comparison between the simulation results and the available experimental measurements. We start from the calibration of the model against current–voltage measurements performed on "conventional" GBTs (proving the proof–of–principle of DC operation [30]), we then move to more advanced GBT structures exploiting bilayer insulators stacks as emitter–base–insulator, that recently have been realized in order to overcame the limitations imposed by the first GBT prototypes [31, 113].

4.2 GBT structure and operation

The Graphene–Base–Transistor (GBT) has a structure very different from the more conventional GFETs [22]. The structure is a vertical arrangement of three regions: a silicon or metal emitter (E), a graphene base (B) and a metal collector (C). These regions are separated each other by two insulators, the base–emitter insulator (EBI) and the base–collector insulator (BCI), as reported in Fig. 4.1. The peculiarity of the GBT is the vertical electron transport through the graphene layer. Although the base is very thin (one atomic layer), it is expected that the high

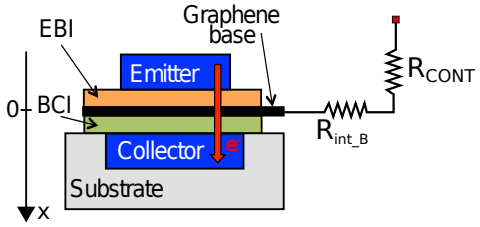

Figure 4.1: Sketch of the GBT structure. Electrons leave the emitter by tunneling through the emitter–base insulator (EBI), cross the graphene base and then travel inside the conduction band of the base–collector insulator (BCI).

mobility of the graphene reduces the base resistance. This aspect has not been verified yet because of the lack of *ad hoc* experiments, but, as it will be shown in Sec. 4.3.6, our simulations predict a limited impact of the graphene resistivity on the device performance.

In the GBT, differently from conventional MOSFETs that rely on the band–gap of the channel material, the ON/OFF state is controlled by the graphene base terminal and it mainly depends on the filtering capability of the EBI and BCI dielectrics. Consequently, the absence of a bandgap in graphene is not an issue for this transistor based on a "vertical" concept.

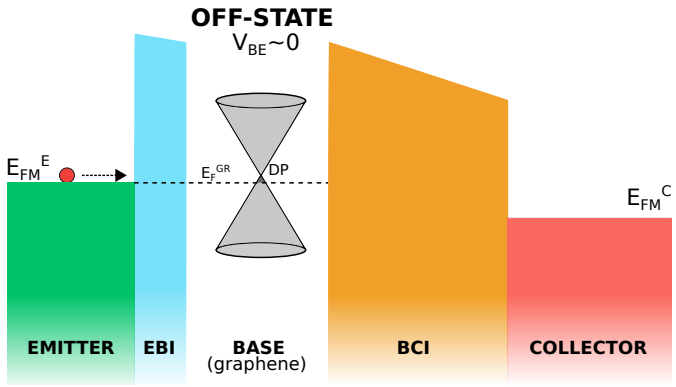

Figure 4.2: Energy band diagram of a GBT in the OFF–state. The base-emitter bias V_{BE} is not sufficient to allow the electron tunneling through the EBI. Under this condition the collector current is almost null.

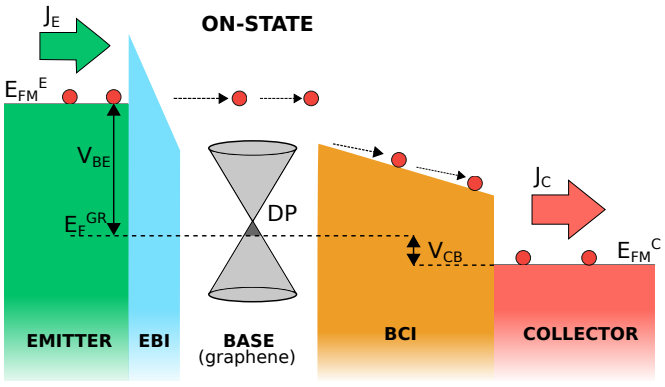

Figure 4.3: Energy band diagram of a GBT in the ON–state. The V_{BE} and V_{CB} are such as to force the electron tunneling through both the EBI and BCI, giving rise to the collector current.

Figures 4.2 and 4.3 report the energy band diagram of the GBT during the OFF and ON state, respectively. Applying a very small or null base–emitter voltage (V_{BE}), the electrons in the emitter face the tunneling barrier created by the EBI (Fig. 4.2). At the same time, up to a certain collector–base voltage (V_{CB}), the BCI acts as a filtering barrier, avoiding the charge tunneling from the base to the collector and leading to a negligible collector current.
During the ON–state instead, a forward bias is applied between the base and emitter terminals. Under this condition, the tunneling through the EBI and BCI of electrons injected from the emitter is favored, giving rise to the collector current (Fig. 4.3). Furthermore, when the V_{BE} is large enough, the tunneling barrier of the BCI completely disappears under the injection level in the emitter, leading to a collector current independent of V_{CB}, or in other words, to the collector current saturation.

4.3 Electrical model for GBT devices

In this section we present the developed electrical model of the GBT, able to simulate the DC operation and calculate the principal RF figures of merit. From the point of view of the GBT operation principle, both metal and silicon (Si) represents a possible design option as emitter material. Anyway, we first illustrate the modelling of a GBT featuring a Si–emitter (Sec. 4.3.1), and then that of metal emitter GBTs (Sec. 4.3.2), since this latter is easily obtained from the first one through simple simplifications. In Sec. 4.3.3 we give useful guidelines for the use of Si or metal as emitter. In Sec. 4.3.4, we will introduce the effects occurring at high current levels (here called high current effects), investigating their impact on the maximum achievable GBT cutoff frequency. Then, we briefly move to the detrimental effect of series resistance on the unity power gain of GBT devices. Finally, in order to validate our model, we compare our simulated current–voltage characteristics against those obtained with a full–quantum simulator, based on Non–Equilibrium Green Functions [24, 113].

4.3.1 Modeling of the GBT with silicon emitter

Let us consider a GBT device exploiting an n–doped Si–emitter. Figure 4.4 reports the complete Conduction Band (CB) diagram of the structure. The developed one–dimensional model solves the electrostatics along the x direction of the GBT (Fig. 4.1) and calculates the tunneling current and the cutoff frequency (f_T). Concerning the currents, although the out–of–plane transport across a graphene layer is not assessed yet [115, 116] (as discussed in Sec. 4.2, in GBTs electrons are crossing perpendicularly the graphene), in this work the graphene base is treated as a completely transparent layer, and no scattering events or energy losses for the electrons that are crossing the base are considered. Hence, we assume *a–priori* that the collector current J_C is the current due to electrons injected from the emitter (J_E=J_C) and crossing the whole device. Consequently, in our simulations, the graphene base impacts only the GBT electrostatics through the effect of the graphene quantum capacitance. This latter plays a fundamental role in the GBT operation, since it leads to an incomplete screening between the collector and the emitter regions. Furthermore, at the moment, we are neglecting any kind of high current effect (h.c.e.), i.e. the electrostatic impact of the space charge in the insulators, that is important only when the number of the charges flowing in the GBT is very large. These high current effects will be included in the model later (see Sec. 4.3.4), but their quantitative relevance is small for the GBTs currently available.

To solve the electrostatics of the device, the total potential drop in the Si–emitter (ΔV_E) and the Fermi level in the graphene base (e_f) have to be determined. Note that e_f is referred to the Dirac Point (DP) and it is taken positive when the Fermi level lies below the Dirac Point,

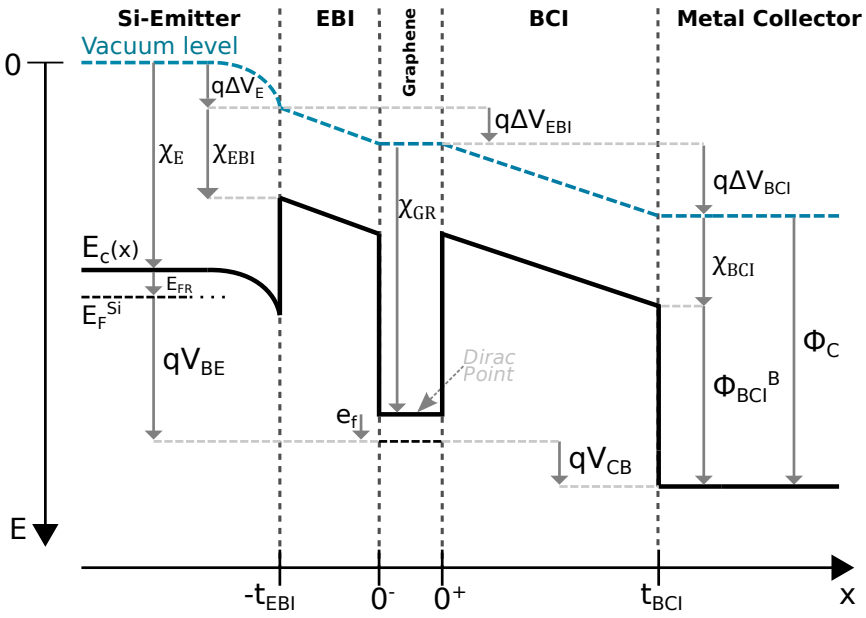

Figure 4.4: Conduction band diagram of a GBT with Si–emitter. The band bending in the Si–emitter is calculated by the model self–consistently with the potential along the GBT structure. The arrows indicate positive quantities.

as it happens in normal GBT operation [22]. As for the emitter–base section, by considering the applied base–emitter voltage V_{BE}, we write (Fig. 4.4):

$$qV_{BE} + E_{FR} + \chi_E = q\Delta V_E + q\Delta V_{EBI} + \chi_{GR} + e_f, \tag{4.1}$$

where ΔV_{EBI} is the potential drop in the EBI, while χ_E and χ_{GR} are the Si and graphene affinities, respectively (Fig. 4.4). Furthermore, E_{FR} is the Fermi level referred to the CB in the Si–emitter and, again, we take it positive when the Fermi level is below the CB bottom. In particular, by assuming a Fermi–Dirac distribution in the Si–emitter, we have:

$$E_{FR} = -k_B T \mathcal{F}_{1/2}^{-1}(N_D/N_C), \tag{4.2}$$

where N_D is the Si doping concentration, N_C is the effective density of states for electrons, k_B is the Boltzmann constant and T is the temperature. $\mathcal{F}_i(\gamma)$ is the Fermi integral of order i according to [117].

From Fig. 4.4, we obtain also the equation for the base–collector section:

$$\chi_{GR} + e_f + qV_{CB} = q\Delta V_{BCI} + \Phi_C, \tag{4.3}$$

where Φ_C is the work function of the metal collector, ΔV_{BCI} is the potential drop on the BCI and V_{CB} is the applied collector–base voltage (Fig. 4.4).

The base charge density $Q_B(e_f)$ is calculated as difference between the electron and hole charges, hence it is related to the Fermi level position in graphene (see also Eq. 3.11):

$$Q_B(e_f) = \frac{2q}{\pi v_F^2 \hbar^2}\left[\int_0^{+\infty} e \cdot \frac{\exp\left[(e_f - e)/(k_B T)\right]}{1 + \exp\left[(e_f - e)/(k_B T)\right]} de - \int_{-\infty}^{0} |e| \cdot \frac{de}{1 + \exp\left[(e_f - e)/(k_B T)\right]}\right]. \tag{4.4}$$

Eq. 4.4 directly expresses $Q_B(e_f)$, where $e{=}E{-}q\Delta V_E{-}q\Delta V_{EBI}{-}\chi_{GR}$ is the energy referred to the Dirac Point (for graphene we considered a Fermi–Dirac distribution for carriers and negligible

chemical doping). Now, Gauss law across the graphene layer yields

$$Q_B(e_f) = \Delta V_{EBI} C_{EBI} - \Delta V_{BCI} C_{BCI} = \Delta V_{EBI} \frac{k_{EBI}\varepsilon_0}{t_{EBI}} - \Delta V_{BCI} \frac{k_{BCI}\varepsilon_0}{t_{BCI}}, \tag{4.5}$$

where C_{EBI} and C_{BCI} are the capacitance, k_{EBI} and k_{BCI} are the relative permittivity and t_{EBI} and t_{BCI} are the thickness of the EBI and BCI, respectively. We get:

$$\Delta V_{BCI} = \frac{1}{C_{BCI}}(C_{EBI}\Delta V_{EBI} - Q_B(e_f)). \tag{4.6}$$

As mentioned before, in the derivation of Eqs. 4.5 and 4.6, we do not consider the electrostatic effect of electrons traveling inside the EBI and BCI during the GBT conduction, whose effect is relevant at high current levels only (see Sec. 4.3.4).

The continuity of the electric displacement field at the Si–emitter/EBI interface gives:

$$\frac{\Delta V_{EBI}}{t_{EBI}} k_{EBI}\varepsilon_0 = \varepsilon_E E_S, \tag{4.7}$$

where ε_E is the permittivity of the emitter material (ε_E=ε_{Si} in our case) and E_S is the electric field at the emitter side of the interface. By inserting Eq. 4.7 into Eq. 4.1 and Eq. 4.6 into Eq. 4.3, we can cast the equations for the emitter and collector regions as

$$\begin{cases} \dfrac{q\varepsilon_E}{C_{EBI}} E_S(\Delta V_E) + q\Delta V_E + e_f = qV_{BE} + E_{FR} + \chi_E - \chi_{GR} \\ \dfrac{q\varepsilon_E}{C_{BCI}} E_S(\Delta V_E) - \dfrac{q}{C_{BCI}} Q_B(e_f) - e_f = \chi_{GR} + qV_{CB} - \Phi_C, \end{cases} \tag{4.8}$$

where E_S is expressed as a function of ΔV_E and $Q_B(e_f)$ is given by Eq. 4.4.

To derive an explicit expression for E_S as a function of the applied potentials, we start by defining the difference between the Si intrinsic Fermi level and the CB minimum as:

$$K_{Fn} = -\frac{E_{GAP}}{2} + \frac{k_B T}{2} \ln\left(\frac{N_V}{N_C}\right), \tag{4.9}$$

where N_V is the density of states for holes. Similarly, the distance between the top of the valence band and the Si intrinsic Fermi level is:

$$K_{Fp} = -\left[\frac{E_{GAP}}{2} + \frac{k_B T}{2} \ln\left(\frac{N_V}{N_C}\right)\right]. \tag{4.10}$$

Consequently, by assuming Fermi–Dirac distribution for the carriers in Si, we write the electron and hole density as

$$n = N_C \mathcal{F}_{1/2}\left(u(x) + \frac{K_{Fn}}{k_B T}\right) \tag{4.11}$$

$$p = N_V \mathcal{F}_{1/2}\left(-u(x) + \frac{K_{Fp}}{k_B T}\right), \tag{4.12}$$

where $u(x)$=$q/(k_BT)\varphi(x)$ is the normalized (dimensionless) potential profile along the Si. With the definitions given above, the Poisson's equation becomes:

$$\begin{aligned} \frac{d^2u(x)}{dx^2} &= \frac{q^2}{k_B T \varepsilon_E}\left[N_C \mathcal{F}_{1/2}\left(u(x) + \frac{K_{Fn}}{k_B T}\right)\right. \\ &\quad \left. - N_V \mathcal{F}_{1/2}\left(-u(x) + \frac{K_{Fp}}{k_B T}\right) - N_D + N_A\right] \\ &= \frac{q^2}{k_B T \varepsilon_E} S(K_{Fn}, K_{Fp}). \end{aligned} \tag{4.13}$$

Let us indicate with u_B and u_S the potentials in the deep bulk ($x \to -\infty$) and at the Si/EBI interface ($x{=}-t_{EBI}$), respectively, so $\frac{du}{dx}(-\infty) = 0$ and $\frac{du}{dx}(-t_{EBI}) = \frac{qE_S}{k_BT}$, where E_S is again the electric field at the EBI interface. By defining $y = (du/dx)^2$ and following the method in [118], we obtain:

$$\int_{\left(\frac{qE_S}{k_BT}\right)^2}^{0} dy = \int_{u_S}^{u_B} 2\frac{q^2}{k_BT\varepsilon_E} S(K_{Fn}, K_{Fp}) du. \tag{4.14}$$

Keeping in mind the definition of $S(K_{Fn}, K_{Fp})$ in Eq. 4.13 and the general propriety of the Fermi integrals ($d\mathcal{F}_j(\eta)/d\eta{=}\mathcal{F}_{j-1}$) [117], the solution of Eq. 4.14 is:

$$\begin{aligned} E_S \;=\; & \sqrt{\frac{2k_BT}{\varepsilon_E}}\Bigg[- N_V\left(\mathcal{F}_{3/2}\left(-u_B + \frac{K_{Fp}}{k_BT}\right) - \mathcal{F}_{3/2}\left(-u_S + \frac{K_{Fp}}{k_BT}\right)\right) \\ & -N_C\left(\mathcal{F}_{3/2}\left(u_B + \frac{K_{Fn}}{k_BT}\right) - \mathcal{F}_{3/2}\left(u_S + \frac{K_{Fp}}{k_BT}\right)\right) + \left(N_D - N_A\right)(u_B - u_S)\Bigg]^{1/2} \end{aligned} \tag{4.15}$$

By considering the electron density in the deep bulk equal to the Si doping ($n(-\infty) = N_D$), we can calculate the value of dimensionless potential u_B (by inverting Eq. 4.11) and u_S (as a function of the potential drop in Si) as:

$$u_B = -\frac{K_{Fn}}{k_BT} + \mathcal{F}_{1/2}^{-1}(N_D/N_C);\; u_S = u_B + \frac{\Delta V_E}{V_{th}}. \tag{4.16}$$

We can now express E_S as a function of the potential drop ΔV_E, thus obtaining:

$$\begin{aligned} E_S(\Delta V_E) \;=\; & \sqrt{\frac{2k_BT}{\varepsilon_E}}\Bigg[- N_V\left(\mathcal{F}_{3/2}\left(\frac{K_{Fn}}{k_BT} - \mathcal{F}_{1/2}^{-1}(N_D/N_C) + \frac{K_{Fp}}{k_BT}\right)\right. \\ & \left. -\mathcal{F}_{3/2}\left(\frac{K_{Fn}}{k_BT} - \mathcal{F}_{1/2}^{-1}(N_D/N_C) - \frac{\Delta V_E}{V_{th}} + \frac{K_{Fp}}{k_BT}\right)\right) \\ & -N_C\left(\mathcal{F}_{3/2}\left(\mathcal{F}_{1/2}^{-1}(N_D/N_C)\right) - \mathcal{F}_{3/2}\left(\mathcal{F}_{1/2}^{-1}(N_D/N_C) + \frac{\Delta V_E}{V_{th}}\right)\right) \\ & -\frac{\Delta V_E}{V_{th}}\left(N_D - N_A\right)\Bigg]^{1/2} \end{aligned} \tag{4.17}$$

We are finally able to solve the system 4.8, since it is a non–linear system of equations in the unknowns e_f and ΔV_E. After numerically solving the system, it is possible to calculate ΔV_{EBI} and ΔV_{BCI} by means of Eqs. 4.6, 4.7 and 4.17.

Once the GBT electrostatic is obtained, the GBT current density can be calculated. The energy spectrum of J_E is [119]

$$dJ_E = \frac{qm_Ek_BT}{2\pi^2\hbar^3} \ln\left[1 + \exp\left(\frac{E - E_F}{k_BT}\right)\right] \cdot T_{WKB}(E) dE, \tag{4.18}$$

where $E_F = \chi_E + E_{FR}$ is the Fermi level in the Si–emitter with respect to the vacuum level (see Fig. 4.4) and m_E is the electron mass in the emitter (for Si, we consider six–fold degenerate conduction band minimum assuming $m_E = 4\sqrt{m_t m_l} + 2m_t$, and the crystal orientation is assumed to be <100>). Then, we calculate the GBT current by integrating dJ_E over energy and cross sectional area. In Eq. 4.18, we neglect quantization effects at the Si/EBI interface. Indeed, they may induce small shifts along the V_{BE} axis in the simulated $J_E(V_{BE})$ curves [120], but we consider them less relevant than other model uncertainties.

In Eq. 4.18, $T_{WKB}(E)$ is the transmission coefficient from the emitter to the collector for the electrons tunneling at the energy E (defined as in Fig. 4.4), which we compute through the

WKB approximation as:

$$T_{WKB}(E) = \exp\left[-\frac{2}{\hbar}\int_0^x \sqrt{2m_I(E_C(x)-E)dx}\right], \tag{4.19}$$

where the integral is calculated over the transport direction x, $E_C(x)-E$ is the difference between the minimum of the conduction band in the insulator at the x position and the considered energy level E, while m_I is the tunneling mass of the generic insulator; indeed, we left the possibility to specify different tunneling masses in the EBI and BCI (m_{EBI} and m_{BCI}, respectively). Furthermore, we consider both direct and Fowler–Nordheim tunneling and, by denoting with χ_{EBI} and χ_{BCI} the EBI and BCI affinities, respectively, T_{WKB} depends on Φ^B_{EBI}=(χ_E−χ_{EBI}) and Φ^B_{BCI}=(Φ_C−χ_{BCI}), that basically are the energy barriers between the emitter and the EBI and between the collector and the BCI, respectively. Finally the collector current can be calculated by integrating over energy Eq. 4.18:

$$J_C = J_E = \int_{E_C}^{\phi_0} (T^{EBI}_{WKB}\cdot T^{Gr}_{WKB}\cdot T^{BCI}_{WKB})\cdot\left(\frac{qm_E k_B T}{2\pi^2\hbar^3}\right)\cdot\ln\left[1+\exp\left(\frac{E^{Si}_F - E}{k_B T}\right)\right]dE, \tag{4.20}$$

where ϕ_0 is the vacuum level, while the overall tunneling coefficient T_{WKB} is split in different contributions T^{EBI}_{WKB}, T^{Gr}_{WKB} and T^{BCI}_{WKB} correlated to the tunneling barrier of the EBI, graphene and BCI, respectively. Concerning transport through graphene, since the DP is at the K–points [34], while the energy at the Γ–point is larger, the assumption of momentum conservation would result in a tunneling barrier which is not the CB profile of Fig. 4.4 but, instead, presents an additional barrier at the position of the graphene layer [22]. However, in computing T^{Gr}_{WKB}, we construct the tunneling barrier by using the minima of the graphene at the K–point (Fig. 4.4), i.e. neglecting momentum conservation, since scattering due to disorder at the EBI/graphene interface can occur. In any case, we have verified that this assumption is not a critical choice for the J_E calculation, since the thickness of this additional barrier would be very thin (≈0.3 nm) [34].

When high current effects are not considered, the cutoff frequency can be estimated following a quasi–static approach, namely:

$$f_T = \frac{1}{2\pi(\tau_C+\tau_D)}, \tag{4.21}$$

where $\tau_C = dQ_B/dJ_E = dQ_B/J_C$ is the *charging time*, representing the delay spent to charge the graphene base, while τ_D is the *drift time*, representing the time needed by the charges to cross the dielectrics. According to the Ramo's theorem, this latter contribution can be calculated as $\tau_D = (t_{EBI}+t_{BCI}-t_{FN})/(2v_D)$ [121], where t_{FN} is the average length of the tunneling path, set null in this work in order to consider the worst case; v_D is the *drift velocity* and it has been set to a realistic value of 10^7 cm/s (Sec. 4.5.2) and it plays a critical role when high current effects are considered (Sec. 4.3.4). At high V_{BE}, the delay τ_D prevails on τ_C leading to the saturation of f_T.

4.3.2 Modeling of the GBT with metal emitter

The conduction band diagram of a GBT with a metal emitter is reported in Fig. 4.5. With respect to the band diagram reported in Fig. 4.4, the profile of the conduction band inside the emitter is now completely flat. Consequently, a model for GBTs with metal emitter can be easily derived from the previous reported in Sec. 4.3.1 by assuming ΔV_E=0, $E_S(\Delta V_E)$=0 and considering $\chi_E + E_{FR}$=Φ^M_E, where Φ^M_E is the work function of the metal emitter (see Fig. 4.5).

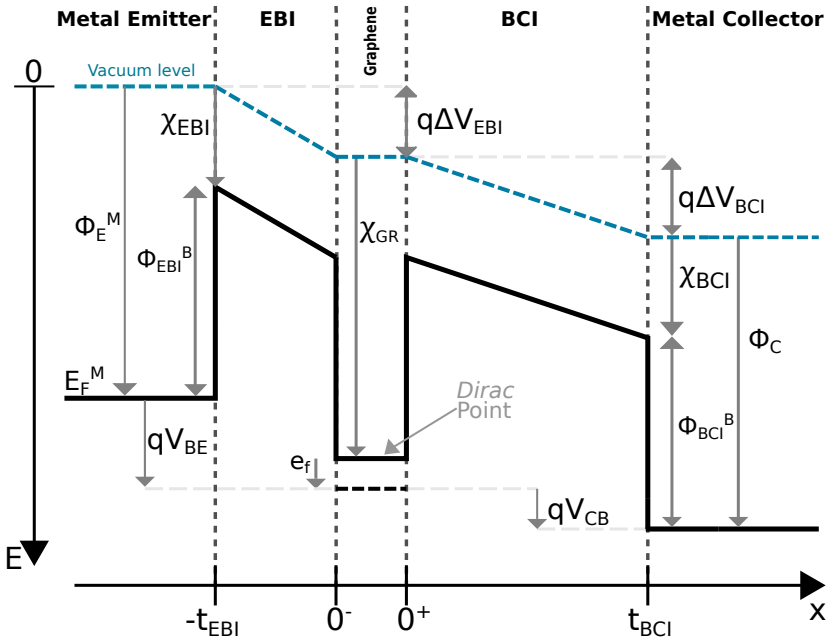

Figure 4.5: Conduction band diagram of a GBT with metal emitter. Note the flat profile of the conduction band inside the emitter. Also in this case, the arrows indicate positive quantities.

Applying these simplifications, the equations of the Syst. 4.8 become:

$$qV_{BE} + \Phi_E^M = q\Delta V_{EBI} + \chi_{GR} + e_f \tag{4.22}$$

$$\frac{qQ_B(e_f)}{C_{BCI}} + e_f = qV_{CB} + \Phi_C - \chi_{GR}, \tag{4.23}$$

while Eq. 4.4 is still valid. In the calculation of the tunneling current done in Eq. 4.18, the term E_F must be now set to ϕ_E^M.

4.3.3 Comparison between GBTs with silicon and metal emitter

By means of the developed model, it is possible to compare GBTs with metal and Si emitters and investigate their performance as a function of the structure and material parameters.

Fig. 4.6 shows ΔV_{EBI} calculated for different EBI and BCI thicknesses (t_{EBI} and t_{BCI}, respectively) and a couple of insulator permittivity values ($k_{EBI} = k_{BCI} = k$). The inflection point in the ΔV_{EBI} vs. V_{BE} curves indicates the Neutrality Point (NP), hence the zero base charge condition (Q_B=0), when the Fermi level in the graphene is aligned with the Dirac Point. In normal GBT operation, the base is charged with holes, thus NP corresponds to the minimum V_{BE} that ensures the correct polarization of the device. We see that for Si–emitter GBTs (filled symbols), NP is moved toward higher V_{BE} than for the metal emitter GBT (open symbols), due to the additional voltage drop in the Si emitter (ΔV_E). This translates in a larger threshold voltages in switching on the device. While t_{EBI} and t_{BCI} contribute in the definition of the NP position (Fig. 4.6(a)), this latter is not impacted by k (b). In fact, taking into consideration the metal emitter case and imposing the neutrality condition in graphene (Q_B=0), then $\Delta V_{EBI} = qV_{BE} + \phi_E^M - qV_{CB} - \phi_C$, which depends only on the emitter and collector materials and on the biasing of the device.

Figure 4.7 reports the calculated J_C vs. V_{BE} for the metal (a) and the Si–emitter (b) GBTs. It is worth noting the opposite dependence of the current on the k value in the two cases. In

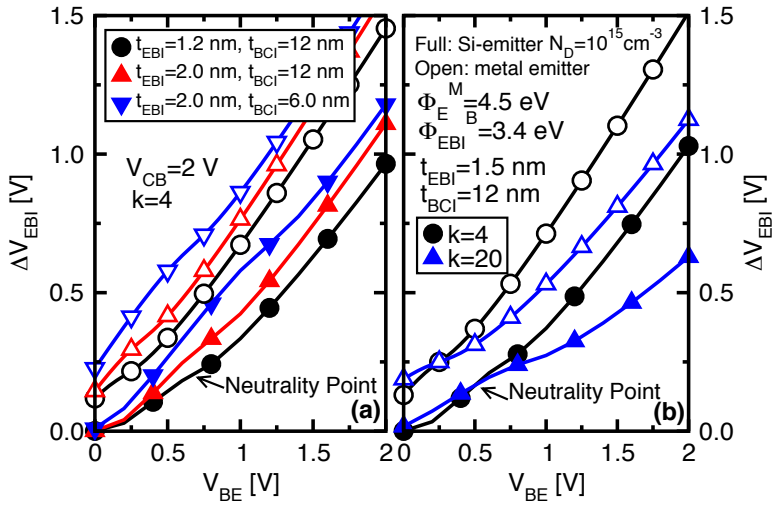

Figure 4.6: Potential drop ΔV_{EBI} as a function of V_{BE} for a few combinations of t_{EBI} and t_{BCI} (a) and for different $k_{EBI} = k_{BCI} = k$ (b) for GBTs with metal (open symbols) or Si emitter (filled symbols). The Si band bending reduces ΔV_{EBI} and induces a shift of the neutrality point to higher V_{BE} with respect to the metal emitter case.

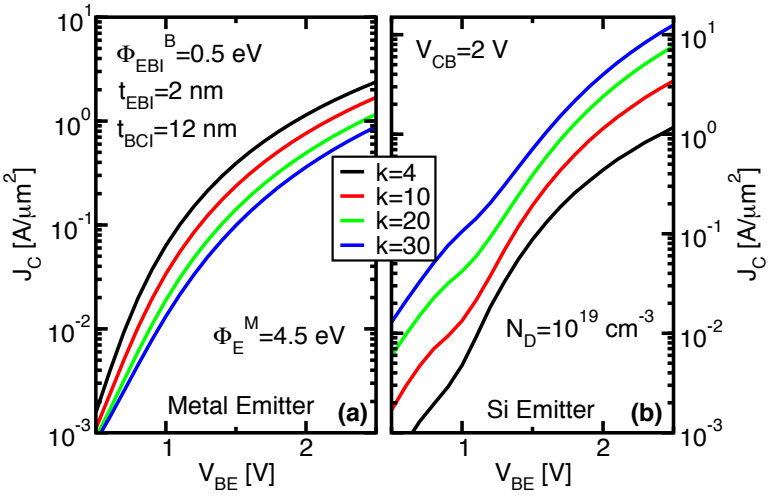

Figure 4.7: Collector current density as a function of V_{BE} for a few values of $k_{EBI} = k_{BCI} = k$ for GBTs with metal emitter (a) and Si–emitter (b). The Si doping is N_D=$10^{19} cm^{-3}$.

fact, the devices show markedly different J_C dependence on the permittivity of EBI and BCI (k_{EBI}=k_{BCI}=k) thus suggesting different optimization strategies. For the metal emitter GBT, the smaller the k value is, the thinner the EBI energy barrier for electrons is (Fig. 4.8(a)), so that a thinner energy barrier leads to larger J_C (Fig. 4.7(a)). For the Si–emitter, instead, J_C increases when increasing k (Fig. 4.7(b)). Indeed, Fig. 4.8(b) shows that larger k values result in lower EBI barriers with respect to the Si Fermi level (dashed line). This is explained by Eq. 4.7: a larger k increases E_S and the Si band bending, thus pushing down the bottom of the Si CB at the interface with respect to the Fermi level. Consequently, the energy barrier for the electrons tunneling at the Fermi level decreases, thus increasing the current. Furthermore, the presence of the band bending at the Si/EBI interface induces a dependence of the Si Fermi level on the applied V_{BE}, strongly modifying the J_C–V_{BE} behavior with respect to the metal emitter case (see Fig. 4.7), in which the electron injecting level is instead fixed (i. e. the metal Fermi level,

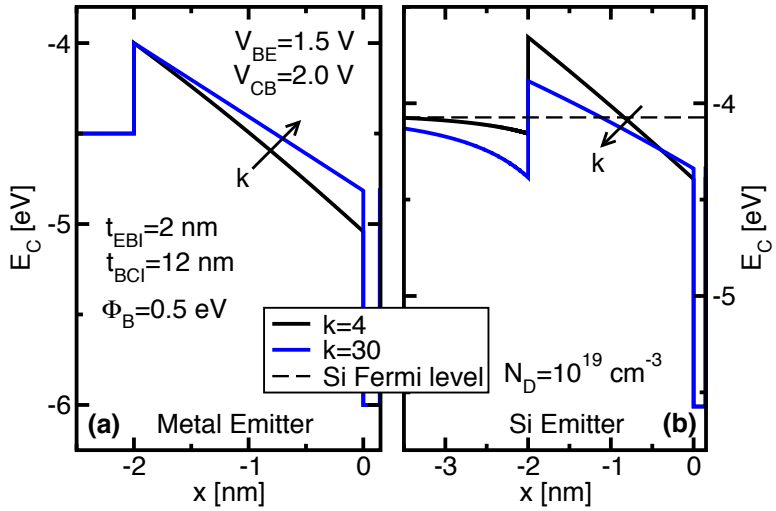

Figure 4.8: Conduction band diagrams calculated for GBTs with metal (a) and Si–emitter (b). Note the opposite dependence of the EBI barrier on the k_{EBI}=k_{BCI}=k.

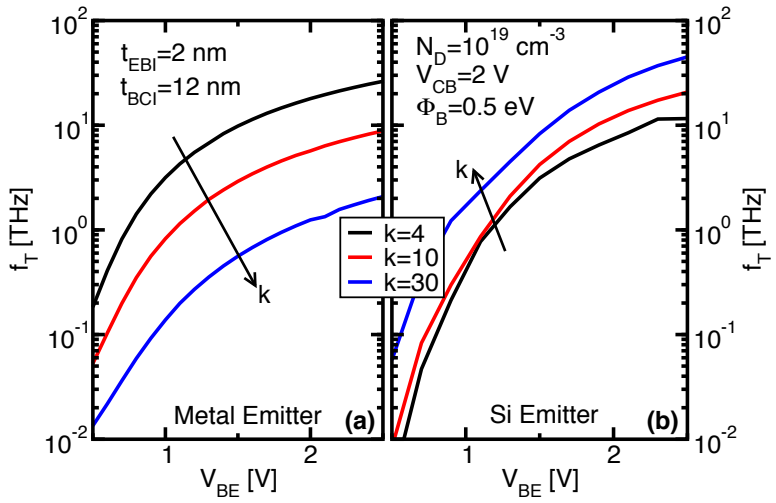

Figure 4.9: Cutoff frequency versus V_{BE} for a few values of k_{EBI}=k_{BCI}=k for GBTs with metal (a) and Si–emitter (b). The opposite f_T dependence on the k value is explained by the CB diagrams shown in Fig 4.8.

see Fig. 4.8).

Figure 4.9 reports f_T versus V_{BE} curves for GBTs with metal (a) and Si (b) emitters. Clearly, the dependence of f_T on k is the same of the J_C curves in Fig. 4.7; consequently, for the metal emitter device (Fig. 4.9(a)), the larger the k is, the lower the cutoff frequency is; contrary, larger k values increase f_T in Si–emitter devices (Fig. 4.9(b)). Anyway, the model predicts that THz operation may be possible for both the design configurations.

4.3.4 Modeling of the GBT under high current regime

In general, the high current effects impacting the maximum f_T of bipolar devices are due to the electrostatic feedback generated by the mobile charge traveling through the collector high field region [122]. To investigate if similar effects are relevant also in GBTs, we included in the electrostatics the charge traveling in the EBI and BCI layers.

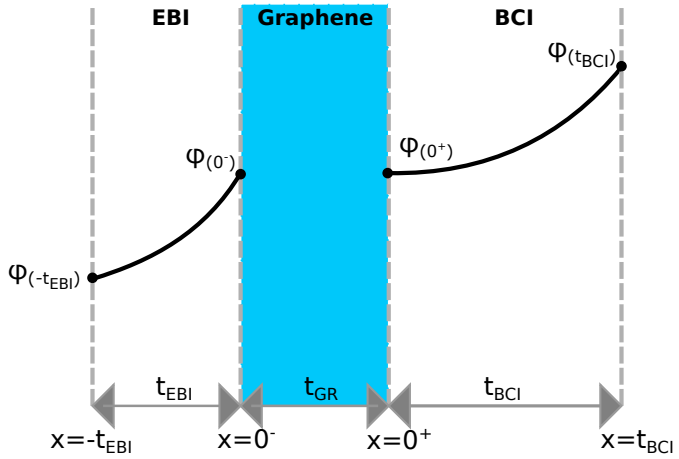

Figure 4.10: Parabolic potential profile considering a negative constant charge inside the EBI and BCI. The blue area represents the graphene layer.

Since in the GBT current calculation we consider only electrons moving from the emitter to the collector, thus neglecting possible hole tunneling components [24], the electron density in the EBI is:

$$n_{EBI} = \frac{J_E}{q v_{EBI}^d}, \tag{4.24}$$

where v_{EBI}^d is the average electron drift velocity in the EBI (assumed constant in space). A similar expression relates n_{BCI} and v_{BCI}^d in the BCI. As done in Eq. 4.21 for the calculation of the drift time τ_D, v_{EBI}^d and v_{BCI}^d are both set to $v_{EBI} = v_{BCI} = v_d = 10^7$ cm/s [123] and hence, n_{EBI}=n_{BCI}=n. Since the carrier density is assumed constant, the CB profile inside the EBI and BCI becomes parabolic (see Fig. 4.10).

For simplicity, let us consider a GBT device implementing a metal emitter with work–function Φ_E^M, so Eqs. 4.22 and 4.23 are considered. Figure 4.11 reports the conduction band diagram of the complete device under high current regime.

The negative uniform charge (ρ=$-qn$) due to the electrons traveling across the EBI and BCI enters the Poisson's equation, which provides the parabolic potential profile in the dielectrics:

$$\varphi = ax^2 + bx + c = \frac{qn}{2\varepsilon}x^2 + bx + c, \tag{4.25}$$

where ε is equal to $k_{EBI}\varepsilon_0$ for EBI and to $k_{BCI}\varepsilon_0$ for BCI, and b and c are two constants to be determined. ΔV_{EBI} is the difference between the potential at the graphene interface (x=0) and at the emitter interface (x=$-t_{EBI}$, Fig. 4.11). From Eq. 4.25 we get:

$$\Delta V_{EBI} = \varphi(0) - \varphi(-t_{EBI}) = -\frac{qn}{2\varepsilon_{EBI}}t_{EBI}^2 + b_{EBI}t_{EBI}, \tag{4.26}$$

hence, we can express the parameter b_{EBI} as a function of ΔV_{EBI}:

$$b_1 = \frac{1}{t_{EBI}}\left[\Delta V_{EBI} + \frac{qn}{2\varepsilon_{EBI}}t_{EBI}^2\right]. \tag{4.27}$$

Next, we find the electric field $E_{EBI}(0^-)$ at $x = 0^-$:

$$E_{EBI}(0^-) = -\left.\frac{d\varphi}{dx}\right|_{x=0^-} = -\left[\frac{\Delta V_{EBI}}{t_{EBI}} + \frac{qn}{2\varepsilon_{EBI}}t_{EBI}\right]. \tag{4.28}$$

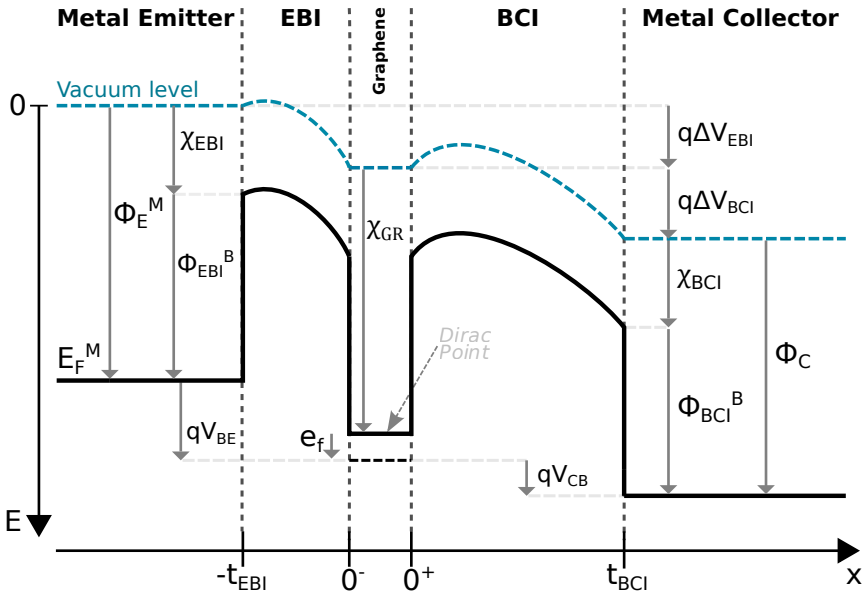

Figure 4.11: Conduction band diagram across a GBT with metal emitter under high current fluxes. The figure reports the physical quantities used to derive the electrostatic model. The arrows indicate positive quantities.

A similar approach is used for the BCI. By assuming no–potential drop inside the graphene layer (Fig. 4.11), we obtain:

$$E_{BCI}(0^+) = -\frac{d\varphi}{dx}\bigg|_{x=0^+} = -\left[\frac{\Delta V_{BCI}}{t_{BCI}} - \frac{qn}{2\varepsilon_{BCI}} t_{BCI}\right]. \tag{4.29}$$

The base charge is $Q_B(e_f)=\varepsilon_{BCI}E_{BCI}(0^+)-\varepsilon_{EBI}E_{EBI}(0^-)$ and, by using Eqs. 4.28 and 4.29, as well as Eqs. 4.22 and 4.23, we obtain:

$$Q_B(e_f) = \frac{qn}{2}(t_{EBI}+t_{BCI}) + \frac{k_{EBI}\varepsilon_0}{t_{EBI}}(\phi_E^M + V_{BE} - \chi_{GR} - e_f) - \frac{k_{BCI}\varepsilon_0}{t_{BCI}}(\chi_{GR} + e_f + V_{CB} - \phi_C). \tag{4.30}$$

Now, by using Eq. 4.4 in Eq. 4.30, we derive a non–linear equation in the only unknown e_f, whose solution provides the potential profile once J_E is given.

To calculate the GBT current density, we again integrate over energy Eq. 4.18, by assuming E_F=Φ_E^M and m_E=m_0 as the electron mass in the metal emitter. Now, by combining Eqs. 4.24, 4.30 and 4.18, the complete system of non–linear equations for the device electrostatics and the transport is obtained.

To solve the system, we implement an iterative, self–consistent procedure that, at each iteration, calculates the potential profile and then J_E (see Fig. 4.12). This latter is used to evaluate the charge inside the dielectrics (n, through Eq. 4.24), that becomes an input for the solution of the potential at the next iteration (Eq. 4.30). A damping algorithm prohibits collector current changes larger than 10% between two iterations, thus ensuring convergence.

Under this conditions, the cutoff frequency of the intrinsic device is now calculated as

$$f_T = \frac{1}{2\pi\tau_C} = \frac{1}{2\pi\frac{dQ_B}{dJ_E}}, \tag{4.31}$$

differently from what done before in Eq. 4.21. Indeed, Eq. 4.31 does not include the transit time τ_D of electrons through the dielectrics, since it is inherently accounted for in the electrostatics,

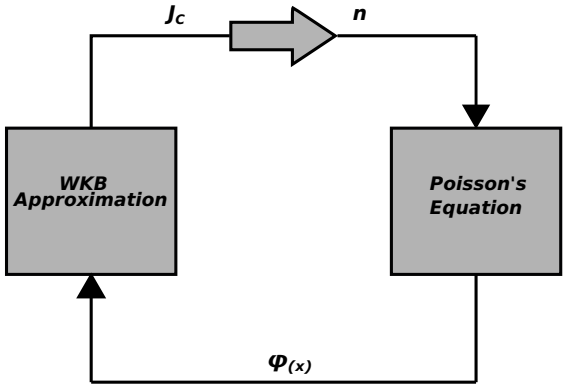

Figure 4.12: Self–consistent procedure between the Poisson's equation solver and the calculation of the collector current for the inclusion of high current effects.

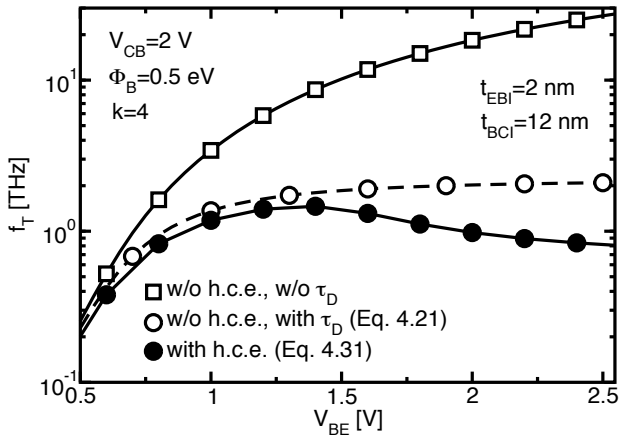

Figure 4.13: Cutoff frequency of a metal emitter GBT calculated with the model non–considering the h.c.e. (open symbols) and the one accounting for the moving electrons inside the dielectrics (filled circles). At low V_{BE} (<1.5 V), the latter agrees with the model in Sec. 4.3.2, where the term τ_D accounts for the electron drift across the dielectrics (open circles). For V_{BE}>1.5 V, the electrostatic feedback of the traveling charges further reduces f_T with respect to the model in Sec. 4.3.2. In this preliminary model, neglecting τ_D results in very high f_T values (open squares), which are completely different with respect to the other cases. Φ^B_{EBI}=Φ^B_{BCI}=Φ_B. k is the relative permittivity of both EBI and BCI and we assumed Φ^M_E=4.5 eV and m_E=m_0 [23].

where the traveling charge and its modulation with bias are included. This is demonstrated by Fig. 4.13; for V_{BE}<1.5 V, the model developed so far (black circles) agrees with the model not including space charge effects (Sec. 4.3.2), which calculates f_T with Eq. 4.21 by adding the term τ_D to τ_C (open circles). Instead, the two models largely differ if τ_D is neglected (open squares), thus confirming that, in the self–consistent model, the delay due to the traveling time of electrons is already included. For V_{BE}>1.5 V, the electrostatic feedback of the electrons in the insulators increases the base charge, resulting in lower transconductance than that calculated with the non self–consistent model and, consequently, in smaller f_T (also when including τ_D).

Concerning the role of the drift velocity of electrons inside the insulators, Fig. 4.14 shows f_T versus J_C estimated assuming different v_d values. The simulations that account for the high current effects (lines) show the drop–off at large J_C typically seen also in HBTs. This effect

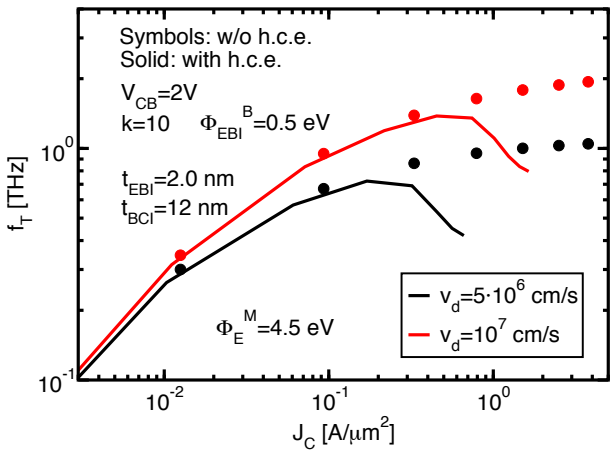

Figure 4.14: Cutoff frequency f_T vs. J_C of a metal emitter GBT calculated with different models and for a couple of $v_d = v^d_{EBI} = v^d_{BCI}$ values. H.c.e induce f_T drop at large J_C.

is not visible in the simulations with the model neglecting h.c.e. (symbols), that are reported as a reference. When v_d is reduced, the maximum f_T of the device is lower. Anyway, with the assumed value of v_d=10^7 cm/s, the THz operation of the intrinsic device is maintained also when accounting for high current effects.

4.3.5 Impact of high current effects on GBT characteristics

By using the complete model of Sec. 4.3.4, we analyzed the impact of the moving electrons in the GBT electrical behavior.

Figure 4.15(a) shows the calculated ΔV_{EBI} versus the applied V_{BE}. The symbols are the reference curve calculated with the non–self–consistent model of Sec. 4.3.2. When the high current effects are accounted for (lines) and when the energy barrier height between the emitter

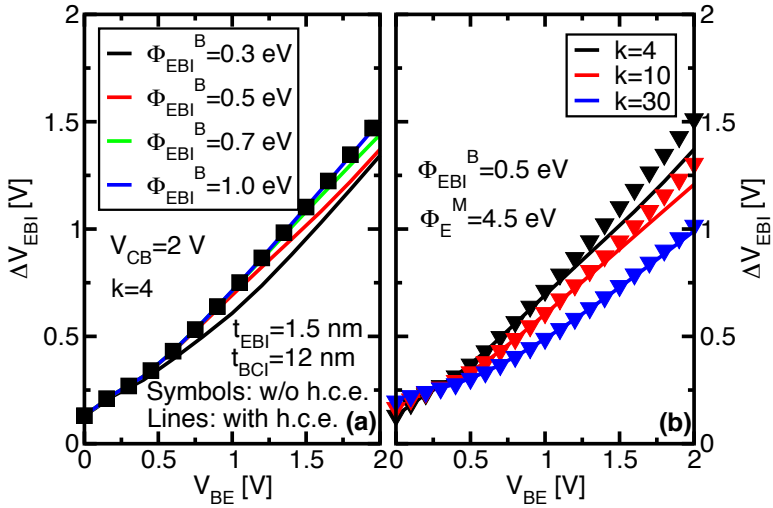

Figure 4.15: Potential drop ΔV_{EBI} on the EBI as a function of the applied V_{BE} for different EBI barrier heights Φ_B (a) and for different dielectric constants (b) of metal emitter GBTs. (a) The electrostatics visibly changes when relatively low Φ_B are considered due to the J_C impact on the electrostatics. (b) The k value mediates the h.c.e.

and the EBI (Φ^B_{EBI}) is relatively large, the tunneling current is low and, thus, the charge in the oxides is small. In other words, the simulations with the complete model are getting closer to the symbols when the barrier height is increased, hence n is becoming negligible. By reducing Φ^B_{EBI}, instead, the tunneling of emitted electrons (thus J_C) increases. This raises the n value inside the oxides and, hence, changes the potential profile. In fact, Fig. 4.15(a) shows that by reducing Φ^B_{EBI}, ΔV_{EBI} moves away from the non self–consistent simulation.
Figure 4.15(b) shows how the k value (again we are considering $k_{EBI} = k_{BCI} = k$) mediates the high current effects. For low k values, the difference between the two models (solid lines and symbols for the self–consistent and non self–consistent models, respectively) is relatively large, while for large k values it is reduced. This means that GBTs with high–k dielectrics are less prone to h.c.e. and this is due to the fact that a larger permittivity of the dielectric reduces the impact of the space charge on the GBT electrostatic (see Eq. 4.25).

Figure 4.16 shows J_E as a function of V_{BE} for a few values of the EBI thickness. For V_{BE} <1 V, the J_E values calculated including the injected charge in the electrostatics (solid lines) are close to the dashed lines, obtained without considering the contribution of the traveling charge. For larger V_{BE}, instead, the current in the device increases and the traveling charge limits J_E. Indeed, the charge in the oxides (mainly in the BCI) opposes the further injection of electrons from the emitter, thus leading to saturation of J_E. Note that J_E at high V_{BE} becomes insensitive to t_{EBI}, because $J_E(V_{BE})$ is limited by the charge in the BCI, in agreement with [24].

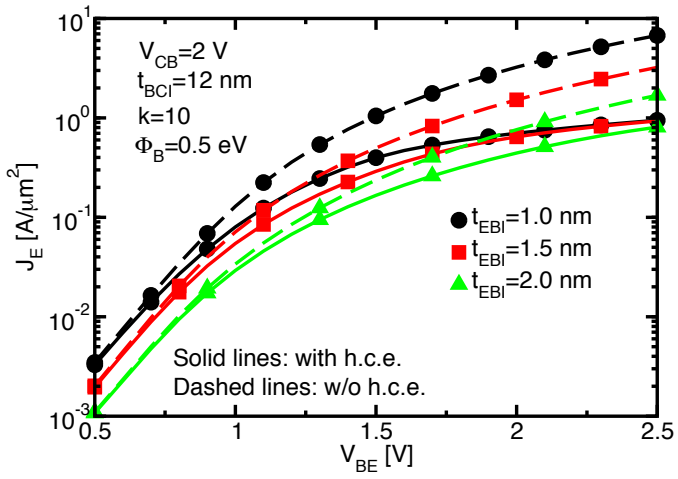

Figure 4.16: Current density versus V_{BE} for different t_{EBI}. The inclusion of high current effects (solid lines) leads to a saturation of J_E at the larger V_{BE} values. Φ^B_{EBI}=Φ^B_{BCI}=Φ_B. $k = k_{EBI} = k_{BCI}$. In this and the next simulations, $m_{EBI} = m_{BCI} = 0.25m_0$ are assumed.

Figure 4.17 shows f_T as a function of t_{BCI}. Again, the cutoff frequency of the GBT is limited by the electrostatic impact of the charge inside the BCI layer, as already seen in Figs. 4.13 and 4.14. The BCI is typically much larger than the EBI, hence it contains a larger amount of charge that, via the electrostatics feedback, impacts the base hole density, thus reducing f_T (see Eq. 4.31). Indeed, by increasing t_{BCI}, if high current effects are accounted for, the model predicts f_T values (Fig. 4.17, solid lines) much lower than those obtained with the non self–consistent model (dashed lines). Again, the k value is effective in mediating the impact of h.c.e. on f_T: the larger the k is, the smaller the f_T reduction is (see also Fig. 4.15).

Now, the developed model makes it possible to estimate realistic maximum f_T values for the intrinsic GBT device, allowing an accurate comparison of the GBT RF performance with recently reported HBT data. Fig. 4.18 shows the GBT cutoff frequency as a function of J_E

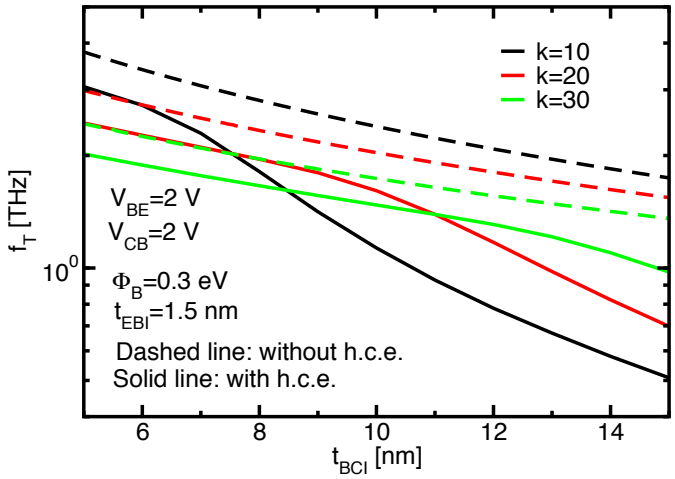

Figure 4.17: Cutoff frequency f_T as a function of t_{BCI} for metal emitter GBTs, calculated using different models: thick BCI layers cause a serious decay in the GBT performance.

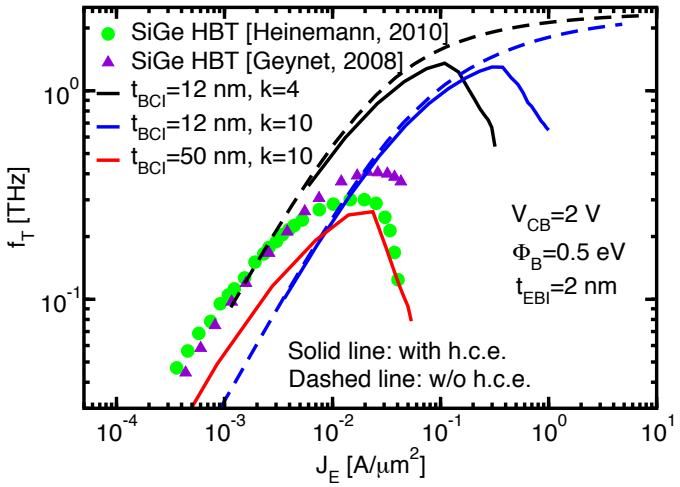

Figure 4.18: Cutoff frequency versus J_E for a few dielectric constants k_{EBI}=k_{BCI}=k. Reference data for SiGe HBT devices are reported for comparison (symbols) [124, 125]. Simulations of a GBT with very thick BCI are also reported (red line). We assumed Φ^B_{EBI}=Φ^B_{BCI}=Φ_B=0.5 eV.

for a few k=k_{EBI}=k_{BCI} values. Again, the f_T drop typical of high current conditions can be observed (solid lines). In spite of the reduced performance, the maximum f_T for GBT overcomes the 1 THz threshold. High current effects appear to be less of a limiting factor in GBTs than in SiGe HBTs (symbols). A maximum f_T comparable to that of HBTs would be reached only for a GBT design with a very thick BCI (t_{BCI}=50 nm, red line). Indeed such BCI thickness would be close to the typical base-collector depletion region width in HBTs [122], thus explaining why this case shows similar maximum f_T.

The maximum f_T for GBTs is obtained for J_E≈0.1 A/μm^2; at present it is not clear if any dielectric can sustain such high J_E. Reliability of SiO_2 has been studied for current densities approximately up to 10^{-7} A/μm^2 [126] and, consequently, it is hard to extrapolate a time–to–breakdown corresponding to the current densities in Fig. 4.18. On the other hand, tunneling current densities in the range $10^{-3}/10^{-2}$ A/μm^2 have been measured across boron nitride layers sandwiched between two graphene electrodes [72].

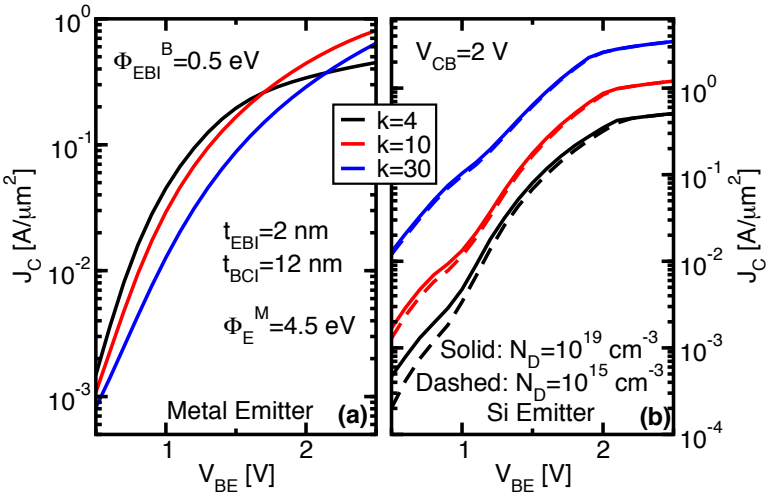

Figure 4.19: The same as in Fig. 4.7 but including the high current effects, for GBTs with metal emitter (a) and Si–emitter (b). In the latter, the Si doping is N_D=$10^{15}cm^{-3}$ (dashed lines) and N_D=$10^{19}cm^{-3}$ (solid lines).

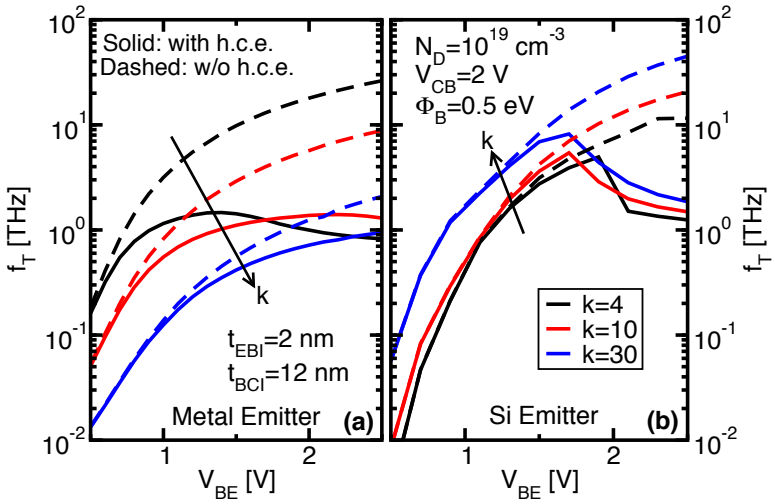

Figure 4.20: The same as in Fig. 4.9 (dashed lines) including the high current effects (solid lines).

In order to deeply evaluate the different technological options for the GBT, in Fig. 4.19 we compare metal against Si emitter GBTs. We simulated the same GBT devices of Figs. 4.7–4.8, but now including the high current effects. It is interesting to note now that, in the metal emitter device (Fig. 4.19(a)), when high current effects are weak (i.e. V_{BE}<1.5 V), the larger the k is, the lower the current is (as in Fig. 4.7(a)), differently to what happens for V_{BE}>1.5 V: in this range in fact, high current effects are taking place and since GBTs with low–k oxides are more prone to h.c.e., it results in lower J_C. For this reason in Fig. 4.19(a) the black line is crossing the other curves.
For the Si–emitter device (Fig. 4.19(b)), the dependence of J_C on k shown in Fig. 4.7(b) is maintained also including high current effects in the whole V_{BE} range. Furthermore, Fig. 4.19(b) shows also that the J_C dependence on the Si doping (N_D) is limited, especially at large V_{BE}, where the Si emitter is driven in strong accumulation and the ΔV_E is similar, regardless of N_D.

Fig. 4.20 shows the impact of the high currents effects on the achievable f_T. Even in presence

of high currents effects (solid lines), THz operation are reached. In addition, for the metal emitter GBT (Fig. 4.20(a)), at low voltage, the charge in the insulators is small and the electrostatic feedback negligible, so the same behavior is expected as in Fig. 4.9(a). At large V_{BE} instead, when high current effects take place, smaller k values result in a larger impact of n on the electrostatics (Eq. 4.25), that reduces J_E and hence f_T. This reduction has a twofold origin: first, the charge inside the BCI induces holes in the graphene that reduce the electric field across the EBI, thus lowering the tunneling current. Second, it raises the BCI energy barrier. Hence, a trade–off exists, whereby a low k increases injection from emitter, but also space charge effects. As a result, the V_{BE} at maximum f_T changes appreciably, but the maximum f_T only slightly increases when reducing k (Fig. 4.20(a), solid lines).
For the Si–emitter GBTs (Fig. 4.20(b)) the dependence of f_T on k is the same as in Fig. 4.9(b); furthermore, the larger the k is, the lower the insulator charge related effects are, as discussed above. Finally, the sudden drop of f_T at V_{BE} ≈2 V (solid lines) is due to the fact that the electrons at the Si CB bottom start to see the top of the parabolic CB profile of the BCI, pushed up by electron charge build–up. This effect strongly reduces T_{WKB} and J_E.
In Fig. 4.20(b), we assumed N_D=10^{19} cm^{-3}. However the maximum f_T of Si–emitter GBTs is weakly dependent on N_D, since J_E is in turn weakly depending on N_D (see Fig. 4.19). Indeed, smaller N_D leads to larger voltage drop in the Si, but once the emitter is brought in strong accumulation (high V_{BE}), GBTs with different Si doping show similar J_E and similar f_T. Therefore, a lower N_D will translate in a larger V_{BE} to reach high currents, but the intrinsic device maximum f_T is essentially unchanged.

4.3.6 Impact of the series resistance on the unity power gain of the GBT

Since series resistances are one of the major limitations in graphene–based devices (see Sec. 3.4), we included in the model the impact of the series resistances on the performance of the GBTs in terms of the unity power gain frequency (f_{max}).

We estimated f_{max} following the approach normally used for conventional bipolar transistor

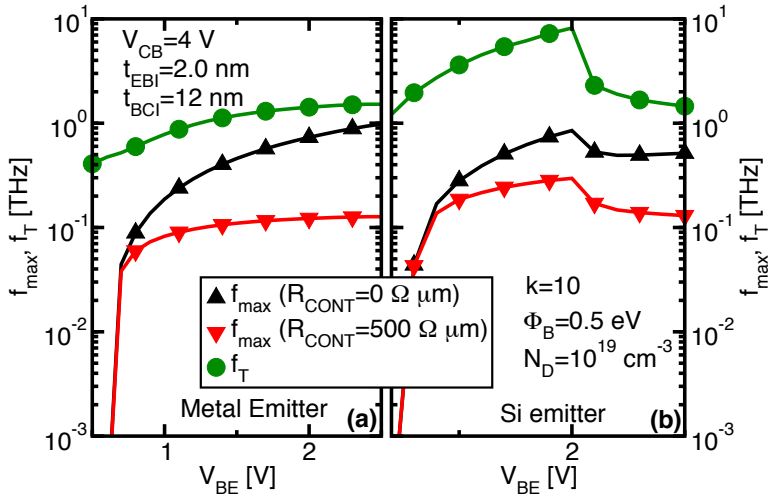

Figure 4.21: Comparison between f_{max} and f_T versus V_{BE} for metal (a) and Si (b) emitter devices and for two values of R_{CONT}. We set k_{EBI}=k_{BCI}= k =10, while hole mobility in graphene is 1000 cm^2/(Vs) [127]. W=L=1 μm.

[122]:

$$f_{max} = \sqrt{\frac{f_T}{8\pi R_B C_{BC}}}, \tag{4.32}$$

where C_{BC} is estimated considering the BCI capacitance only, that is $C_{BCI} = W \cdot L \cdot \varepsilon_{BCI}/t_{BCI}$, where $W \cdot L$ is the GBT area. R_B is the graphene base resistance, calculated as sum of the intrinsic base resistance (R_{int_B}, Fig.4.1) and the contact resistance between the graphene layer and the base contact (R_{CONT} [$\Omega \cdot \mu$m]). Namely

$$R_B = R_{int\_B} + \frac{R_{CONT}}{W} = \frac{L}{12W} \cdot \frac{1}{Q_B(e_f)\mu_p^{GR}} + \frac{R_{CONT}}{W}, \tag{4.33}$$

that considers a simple squared GBT geometry and the graphene base contacted at both sides [122]; L and W represent the distance between the two base contacts and the contact width, respectively. The intrinsic base resistance depends on the effective hole density in the base and on the graphene hole mobility (μ_p^{GR}).

Fig. 4.21 reports the simulated f_T and f_{max} as functions of V_{BE} in the case of metal (a) and Si–emitter (b) devices. We evaluated f_{max} by assuming a realistic mobility value of μ_p^{GR}=1000 cm^2/(Vs) [127] and setting either R_{CONT}=0 $\Omega\mu$m (triangles up) or R_{CONT}=500 $\Omega\mu$m (triangles down) [128]. As expected, f_{max} is lower than f_T and degrades when increasing R_B. The contact resistance R_{CONT} has a strong impact on f_{max} and this indicates that special care should be taken in the fabrication of the contacts to the graphene, a point that is strictly in common with the Graphene–Field–Effect–Transistor devices (see Chapt. 3). Note that, even in the worst case, the f_{max} values are well above 100 GHz and they can reach 1 THz for very small R_{CONT}.

4.3.7 Verification of the tunneling model

We verified the correctness of the developed model comparing simulated current–voltage (IV) curves against simulations performed with the model of [24, 25, 113] developed at the University of Bologna. The two models are (i) exploiting two different modelling approaches (semiclassical vs. Non–Equilibrium Green Function (NEGF) formalism), (ii) based on different assumptions (e.g. our model assumes a uniform charge in the insulators, while the NEGF calculates locally the electron density).

The simulated GBT template features a 3 nm EBI and a 20 nm BCI. The Bologna model assumes a Si emitter, while the EBI and the BCI are silicon–like semiconductivity materials, having the same band structure of Si but with an affinity such as to induce a Schottky barrier of 0.2 eV between the emitter and the EBI, hence the difference between the conduction band minimum in EBI and the Fermi level in the emitter is 0.2 eV (flat band conditions are assumed in the emitter). In order to fairly compare the two simulators, in our model we simulated a GBT with a metal emitter, with an effective mass m_E^M equal to the DoS mass of the 4 silicon valleys

Table 4.1: Material parameters used in our model to simulate the GBT template.

$\phi_{EBI} = \phi_{BCI}$	0.2 eV
$m_{EBI} = m_{BCI}$	0.19 m_0
$k_{EBI} = k_{BCI}$	11.7 ε_0
$\phi_E^M = \phi_C^M$	4.25 eV
m_E^M	$4\sqrt{0.19 \cdot 0.916}\ m_0$
χ_{GR}	4.55

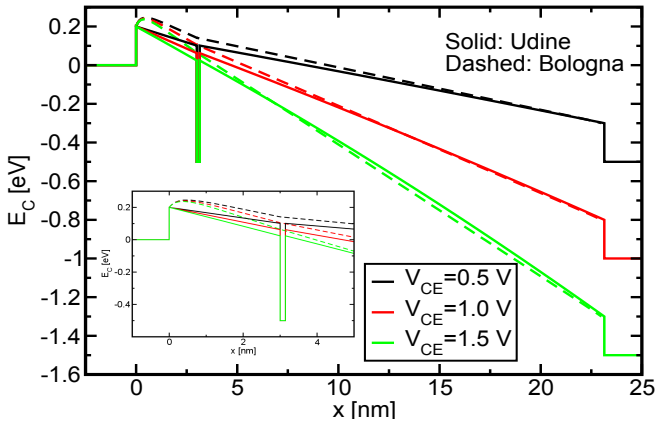

Figure 4.22: Comparison between the energy conduction band profile obtained with the simulator developed in this thesis (solid lines) and with the simulator of [24, 25, 113] (dashed lines) at V_{BE}=1.5 V for a few values of V_{CE}. The inset better shows the difference in the tunneling barrier height at the emitter/EBI interface.

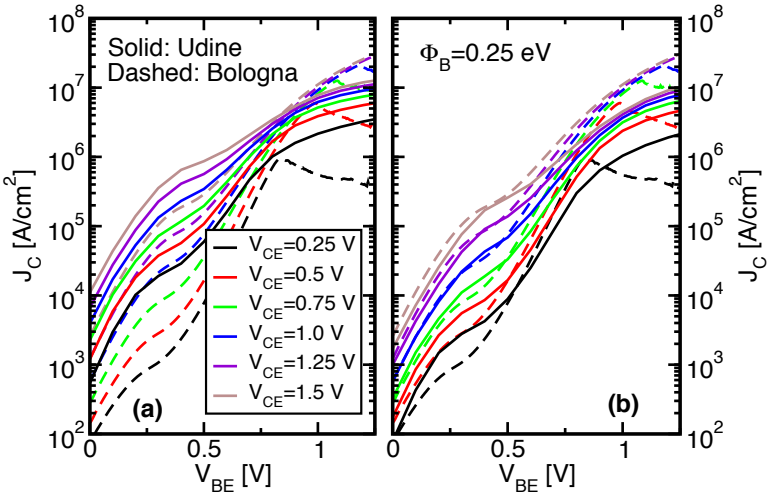

Figure 4.23: (a) Simulated collector current as a function of V_{BE} (solid lines) and comparison with the results obtained with [24, 25, 113] (dashed lines). (b) The agreement between the curves is improved by increasing the EBI barrier height in our model.

having the principal axis of the constant energy ellipsoidal surface parallel to the emitter/EBI interface. All the parameters used in our model are reported in Tab. 4.1.

Figure 4.22 reports the comparison between the conduction band diagrams obtained with the two simulators at different V_{CE} bias values and at V_{BE}=1.5 V. The inset reports the zoom in the EBI region, in order to better show the difference in the simulated conduction band profiles especially at the emitter/EBI interface: the Bologna model shows a significant bending of the conduction band. This is due to the penetration of the electron wave–functions into the EBI, that has not been included in our model. The resulting collector currents are instead reported in Fig. 4.23(a). Despite the complete different modelling approaches between the two models, we can say that a general quite good mutual agreement is obtained. The agreement becomes worst at low V_{CE}, when the EBI barrier height in the Bologna model is particularly high with respect

to our calculations. The agreement of the IV curves is improved if an increased effective barrier for the EBI is considered in our model (Fig. 4.23(b)), thus increasing the CB discontinuity from 0.2 eV to 0.25 eV, even though the situation at high V_{CE} is worst with respect to Fig. 4.23(a).

4.4 Compact model for the GBT

As an application of the developed model presented in Sec. 4.3, it has been also used as reference to develop and calibrate a compact model for the GBT devices, in a joint collaboration with the University of Bordeaux. In particular, the compact model has been developed by the University of Bordeaux, while we provided the reference simulations to calibrate the compact model. All the details about the compact model are reported in [114]. Basically, it relies on a self–consistent base potential calculation and on a physics–based charge model associated with an empirical transfer current equation.

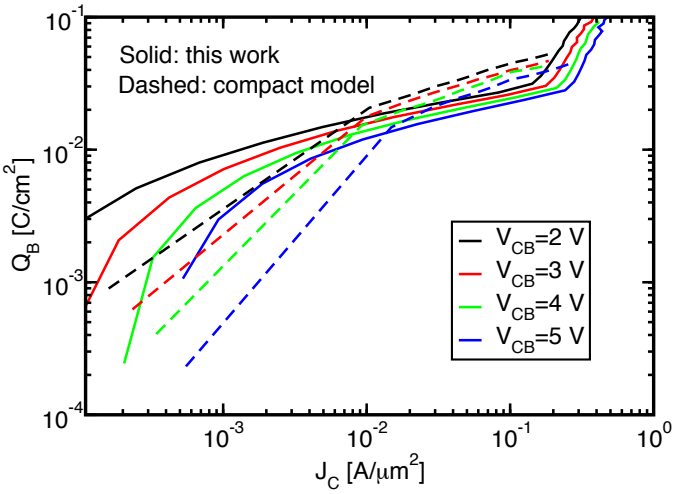

Figure 4.24: Charge accumulated in the graphene base Q_B as a function of the collector current J_C for a few values of the collector–base bias. Comparison between the numerical model (solid lines) and compact model (dashed lines).

The template GBT device used for the calibration of the compact model has 2 nm of EBI ($k_{EBI} = 25$) and a 12 nm BCI ($k_{BCI} = 2.5$). Figure 4.24 shows a comparison between the charge accumulated in the graphene base Q_B as a function of collector current J_C obtained by the numerical simulations (our model) and the results provided by the compact model for a few values of the collector–base bias. A quite good mutual agreement is obtained between the models, although the value of Q_B differs, especially at high base–emitter bias, where high current effects take place. The largely different modelling approaches used to describe this phenomenon causes the deviation of the curves.

A much better agreement is obtained in the transfer characteristics reported in Fig. 4.25, again for few values of the collector–base bias, verifying the calibration of the compact model. Finally, in Fig. 4.26 we compare the cutoff frequency obtained with the two models. A good mutual agreement is observed up to the peak of the cutoff frequency, which represents the optimum bias condition for circuit applications.

The developed compact model has been implemented in Verilog-A and it represents a good trade–off between the accuracy of the predicted results and the simulation time and allows for the analysis of circuits based on GBT devices.

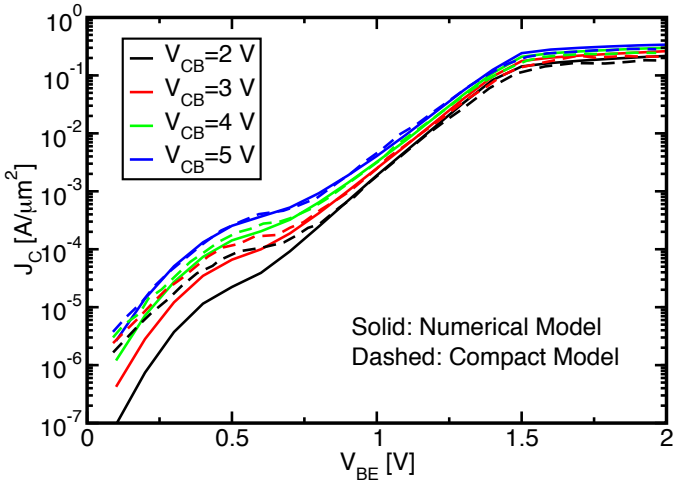

Figure 4.25: Transfer characteristics for a few values of the collector–base bias. Comparison between the numerical model (solid lines) and compact model (dashed lines).

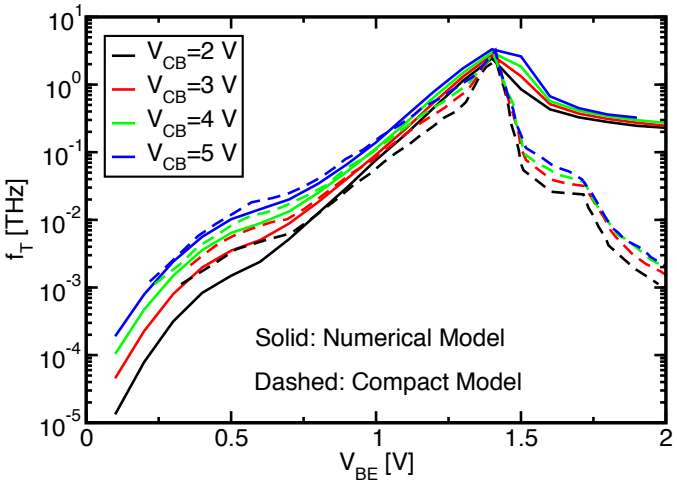

Figure 4.26: Cutoff frequency f_T as a function of the base–emitter bias V_{BE} for a few values of the collector–base bias. Comparison between the numerical model (solid lines) and compact model (dashed lines).

4.5 Monte Carlo simulator for the electron transport through the GBT

The poor performance of the first GBT prototypes is also due to the large measured base current I_B [30, 77] (see also Sec. 4.7.1). To solve the problem, there is the need to understand the origin of I_B. A possible contribution may be due to the electrons backscattered by the BCI, which rejects the electrons towards the graphene base and favors the electron capture by the graphene. In order to evaluate this contribution that degrades the common–base current gain ($\alpha_F = I_C/I_E$) of the GBT, we developed a dedicated Monte Carlo simulator for electron transport in the conduction band of the EBI and BCI.

It is worth noting that another important contribution to the base current can be the direct capture by the graphene base of the forward moving electrons. However, in the lack of a consolidated theoretical framework, in our simulations this contribution to I_B is neglected,

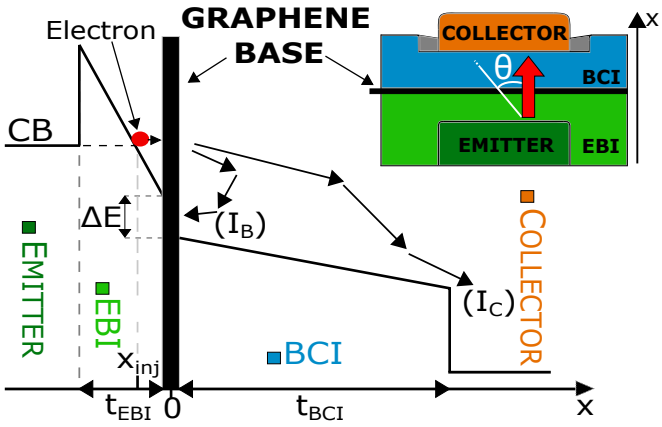

Figure 4.27: Conduction band diagram of the GBT. The electrons injected from the EBI through the graphene scatter in the BCI and either reach the collector (contributing to I_C) or backscatter to the base and are captured by the graphene (thus contributing to I_B). The inset shows the GBT structure and the definition of the backscattering angle θ.

making the calculated α_F an upper estimate of the actual one. Again, consistently with [24], we neglected hole injection from the graphene to the EBI (larger tunneling barrier for holes), since it is expected to provide a negligible reduction of the emitter efficiency and hence of α_F.
During the GBT operation, electrons are injected from the emitter towards the collector by tunneling; with a sufficiently high V_{BE}, Fowler–Nordheim tunneling through the EBI barrier takes place and electrons are injected in the conduction band (CB) of the EBI at x_{inj} (Fig. 4.27) with an energy that corresponds to the Fermi level in the emitter. For electrons crossing the graphene base, we assumed the conservation of the electron momentum parallel to the graphene plane and of the total energy. After crossing the graphene, electrons reach the conduction band of the BCI. During the motion in the conduction band of the dielectrics, the electrons are subjected to many scattering events that can deflect their trajectory depending on the type of the collision occurred. In this respect, we include in the simulator both emission and absorption of polar optical and non–polar acoustic phonons, extending the model presented in [129] to a

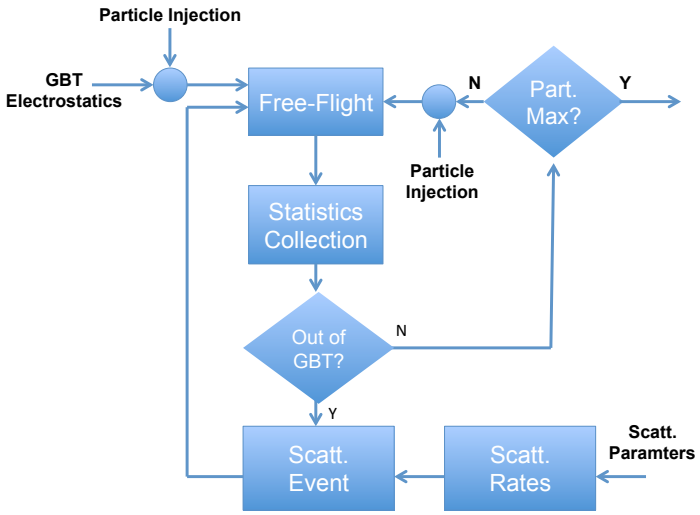

Figure 4.28: Flowchart of the single–particole Monte Carlo simulator for GBT devices.

non–parabolic conduction band material (see Sec. 4.5.1).
The flowchart of the Monte Carlo (MC) simulator is reported in Fig. 4.28. The developed MC tool is of the single–particle type, so it injects in the device one electron at a time once the GBT electrostatics has been determined through the electrical model of Sec. 4.3. Electron free flights and scattering events are alternated until the particle exits the GBT, either arriving to the collector terminal from the BCI with positive velocity (thus contributing to I_C), or impinging the graphene layer with negative velocity due to backscattering in the BCI (thus contributing to I_B, Fig. 4.27). In this latter case, the scattering events occurring in the BCI (mostly in proximity of the graphene/BCI interface) deviate the electron trajectory towards the graphene base ($\theta > \pi/2$, see the inset in Fig. 4.27). In particular, we consider an electron as captured by the base every time it impinges on the graphene; hence, we discard the possibility that such electron can be injected back again in the BCI conduction band. By knowing the amount of electrons that are exiting through the collector and the ones captured by the base during the simulation, we are able to estimate $\alpha_F = I_C/(I_C + I_B)$.

4.5.1 Scattering model for the dielectric materials

As already mentioned above, the scattering model for the charges travelling in EBI and BCI of the GBT has been taken from [129] and it has been extended to a non–parabolic conduction band material [130]. The dielectric is considered as a bulk material and we use the following non-parabolic dispersion relationship:

$$E(1+\alpha E) = \frac{\hbar^2 k^2}{2qm_I} \tag{4.34}$$

where m_I is the transport mass (i. e. the curvature of the dispersion relationship in proximity of its minimum) and α is the non-parabolic coefficient.

Scattering rates for absorption and emission of polar optical phonons are, respectively [130]:

$$S_{po}^{ab} = \frac{q^3\omega_{LO}\sqrt{m_I}}{4\sqrt{2}\pi\hbar^2}\cdot\left(\frac{1}{\varepsilon_>}-\frac{1}{\varepsilon_<}\right)\cdot n_{LO}\cdot\frac{1+2\alpha E_f}{\sqrt{q\gamma_i}}\cdot\log\left(\frac{\sqrt{\gamma_i}+\sqrt{\gamma_f}}{\sqrt{\gamma_f}-\sqrt{\gamma_i}}\right) \tag{4.35}$$

$$S_{po}^{em} = \frac{q^3\omega_{LO}\sqrt{m_I}}{4\sqrt{2}\pi\hbar^2}\left(\frac{1}{\varepsilon_>}-\frac{1}{\varepsilon_<}\right)(n_{LO}+1)\frac{1+2\alpha E_f}{\sqrt{q\gamma_i}}\log\left(\frac{\sqrt{\gamma_i}+\sqrt{\gamma_f}}{\sqrt{\gamma_i}-\sqrt{\gamma_f}}\right) \tag{4.36}$$

where ω_{LO} $[eV]$ is the optical–phonon–energy (or optical–phonon–frequency), $\varepsilon_>$ $[F/m]$ ($\varepsilon_<$) is the permittivity at frequencies larger (smaller) than the considered ω_{LO}, while n_{LO} is the phonon occupation calculated considering the Bose–Einstein statistics. Furthermore $\gamma_i = E_i(1+\alpha E_i)$ (in units of [eV]) and similarly $\gamma_f = E_f(1+\alpha E_f)$, where $E_f = E_i \pm \omega_{LO}$ and E_i and E_f are the initial and final electron energy, respectively. We considered two different values of energy for the longitudinal phonons, consequently in the following we will include the contribution of two different phonons, whose corresponding frequencies are indicated as ω_{LO1} and ω_{LO2}. For this reason, when computing the scattering rates related to the phonon at lower energy (or frequency), then we take $\varepsilon_> = \varepsilon_\infty$ and $\varepsilon_< = \varepsilon_{int}$ (where ε_∞ and ε_{int} are the permittivities calculated at infinite and intermediate frequencies, respectively), while when the phonon at larger energy is considered, then we consider $\varepsilon_> = \varepsilon_{int}$ and $\varepsilon_< = \varepsilon_0$ (where ε_0 is the permittivity calculated at zero frequency).
In the derivation of the model we considered the minimum and the maximum wave–vector values of the phonon as $k_q^{MIN} = k_i - k_f$ and $k_q^{MAX} = k_i + k_f$ (where k_i and k_f are the magnitude of the wave–vector associated to E_i and E_f, respectively). After the scattering event, the state is selected considering a random number r and looking for the phonon wave–vector k_q^*, ensuring

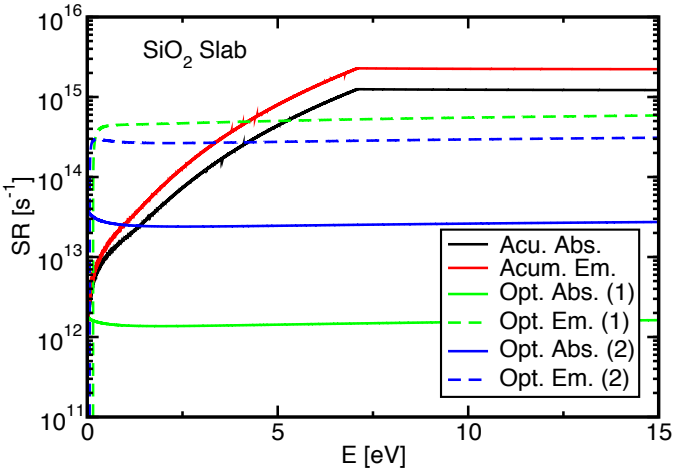

Figure 4.29: Example of the scattering rates included in the Monte Carlo simulator for the case of a SiO_2 slab.

that

$$r = \frac{\int_{k_q^{MIN}}^{k_q^*} \frac{1}{k_q} dk_q}{\int_{k_q^{MIN}}^{k_q^{MAX}} \frac{1}{k_q} dk_q}$$

and thus

$$k_q^* = k_q^{MIN} \exp\left[r \ln\left(k_q^{MAX}/k_q^{MIN}\right)\right]. \tag{4.37}$$

The polar angle θ between the initial and final wave–vector is estimated as:

$$\cos(\theta) = \frac{k_i^2 + k_f^2 - k_q^{*2}}{2k_i k_f}, \tag{4.38}$$

while the azimuth angle ϕ is uniformly distributed in the range [0,2π].
Polar optical phonons alone are not able to stabilize the electron energy at high electric fields, so another scattering mechanism must be introduced in order to dissipate the carrier energy under these conditions and to avoid velocity–runaway phenomena. For this reason, we introduced in our model non-polar acoustic phonons, whose scattering rates are calculated as [130]:

$$S_{ap} = \frac{3m^*(1+2\alpha E_i)q^2 C_{ae}^2}{4\pi\rho\hbar k} \int_{k_q^{MIN}}^{k_q^{MAX}} \frac{k_q^3}{E_q}\left(\frac{1}{2} \pm \frac{1}{2} + n_q\right) dk_q, \tag{4.39}$$

where C_{ae} is the deformation potential (in units of [eV]), ρ is the dielectric density [kg/m^3], $k_q^{MIN} = 2m_0 v_s/\hbar$ (v_s is the sound velocity [m/s]) and $k_q^{MAX} = min(2k_i - k_q^{MIN}, 2\pi/\lambda)$ (where λ is a minimum phonon wavelength). The phonon energy is:

$$E_q = \begin{cases} \frac{2}{\pi}\hbar k_{BZ} v_s \sqrt{1 - \cos\left(\frac{\pi k_q}{2k_{BZ}}\right)} & k_q < k_{BZ} \\ \frac{2}{\pi}\hbar k_{BZ} v_s & k_q > k_{BZ}, \end{cases} \tag{4.40}$$

where k_{BZ} is the wave–vector at the border of the first Brillouin zone.
The wave-vector after the scattering event is selected considering the relation:

$$r = \frac{\int_{k_q^{MIN}}^{k_q^*} \frac{k_q^3}{E_q}(n_q+1) dk_q}{\int_{k_q^{MIN}}^{k_q^{MAX}} \frac{k_q^3}{E_q}(n_q+1) dk_q},$$

Table 4.2: Scattering parameters used for the simulations of Figs. 4.29–4.34 and 4.43. SiO_2 parameters taken from [130].

	χ_I [eV]	m_I [m_0]	α [eV^{-1}]	ε_{stat} [ε_0]	ε_{int} [ε_0]	ε_∞ [ε_0]	ω_{LO1} [meV]	ω_{LO2} [meV]	C_{ae} [eV]	ρ [kg/m^3]	v_s [m/s]
SiO_2	0.95	0.5	0.2	3.9	3.15	2.19	153	63	2.1	2.2×10^3	4.6×10^3
Al_2O_3	1.65 [131]	0.4 [131]	0.2	10 [131]	7.27 [132]	3.2 [132]	109 [133]	63.3 [133]	2.1	3.7×10^3	1.0×10^3

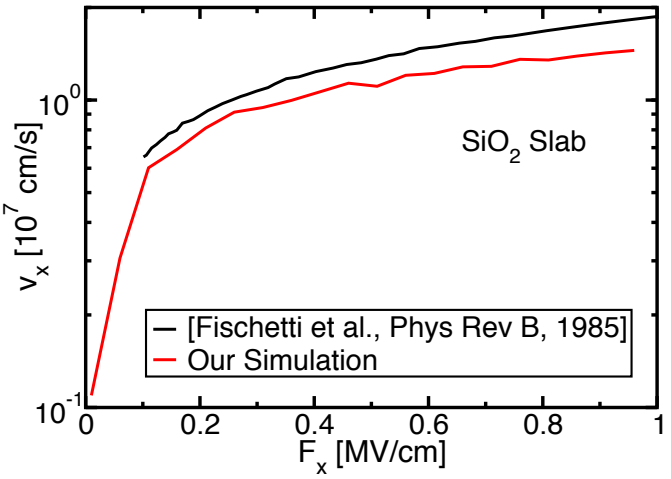

Figure 4.30: Calculated average electron velocity as a function of the electric field again in a SiO_2 slab and comparison with the data in [129].

where r is again a random number uniformly distributed between 0 and 1 and the final energy $E_f = E_i \pm E_q(k_q^*)$.

The scattering rates obtained by the described model are used as input for the Monte Carlo tool (see Fig. 4.28). An example of the scattering rates obtained for a silicon dioxide (SiO_2) slab is reported in Fig. 4.29 (Tab. 4.2 summarizes the parameters used to simulate SiO_2 [130]). Figure 4.30 instead compares the corresponding average electron velocity in the dielectric CB as a function of the applied electric field (again in a SiO_2 slab) calculated with our Monte Carlo simulator and the results obtained in [129], showing how the trend of the average velocity is correctly reproduced.

4.5.2 Electron transport in the GBT

Moving now to the simulation of the GBT structure, Fig. 4.31 shows the calculated electron concentration ($n(x)$) and the average velocity ($v_x(x)$) along the transport direction x in a GBT with SiO_2 dielectrics (both EBI and BCI) and t_{EBI}=3.0 nm and t_{BCI}=12 nm for a few V_{BE} values. As expected, the injection point x_{inj} moves backward as V_{BE} is increased due to the larger conduction band bending. The electron concentration is calculated according to the relation $n(x) = J_C/(q \cdot v_x(x))$, where J_C is the GBT collector current density simulated with the electrical model presented in Sec. 4.3 and $v_x(x)$ is given by the Monte Carlo simulation. In the EBI, $n(x)$ decreases along x (Fig. 4.31(a)), because electrons are accelerated (Fig. 4.31(b)) by the strong electric field. In the BCI, instead, the electron concentration and the average velocity along x are essentially constant. These simulations verify the important assumption made in

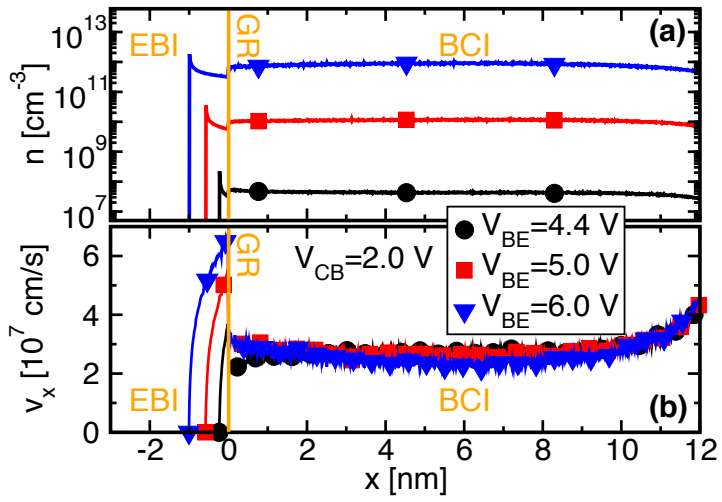

Figure 4.31: Average electron concentration (a) and average electron velocity (b) along a GBT device with EBI and BCI made of SiO_2 (t_{EBI}=3.0 nm, t_{BCI}=12 nm) for a few values of V_{BE}.

the development of the model in Sec. 4.3.4, where we assumed a constant electron drift velocity (v^d_{EBI}=v^d_{BCI}=10^7 cm/s) in the dielectrics when accounting for the space charge effects.

Simulations of GBT featuring different BCI materials confirm that the average electron velocity is always in the order of 10^7 cm/s. As an example, Fig. 4.32 shows the electron concentration (a) and the corresponding electron drift velocity (b) along the transport direction in a GBT with a 5.0 nm of SiO_2 and 15 nm of alumina (Al_2O_3) for a few values of V_{CB} [134]. Scattering parameters of Al_2O_3 are reported in Tab. 4.2. The average behavior of the electrons moving in the device is similar to that in Fig. 4.31. The structure of this latter simulated GBT is similar to the first realized GTB prototype, which uses Al_2O_3 as BCI [30] (see Sec. 4.7.1). Furthermore, these results confirm that, by using v^d_{EBI}=v^d_{BCI}=10^7 cm/s in the electrical model, we are overestimating the space charge effects, since in the simulated dielectrics the electron velocity is always larger and, thus, the related space charge effects should be smaller. Moreover,

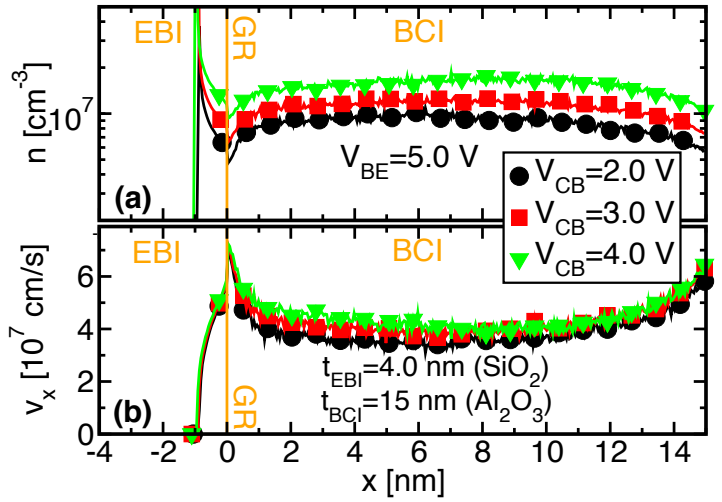

Figure 4.32: Average electron concentration (a) and average electron velocity (b) along a GBT device with an EBI of SiO_2 and a BCI made of Al_2O_3 (t_{EBI}=4.0 nm, t_{BCI}=15 nm) for a few values of V_{CB} and V_{BE}=5 V.

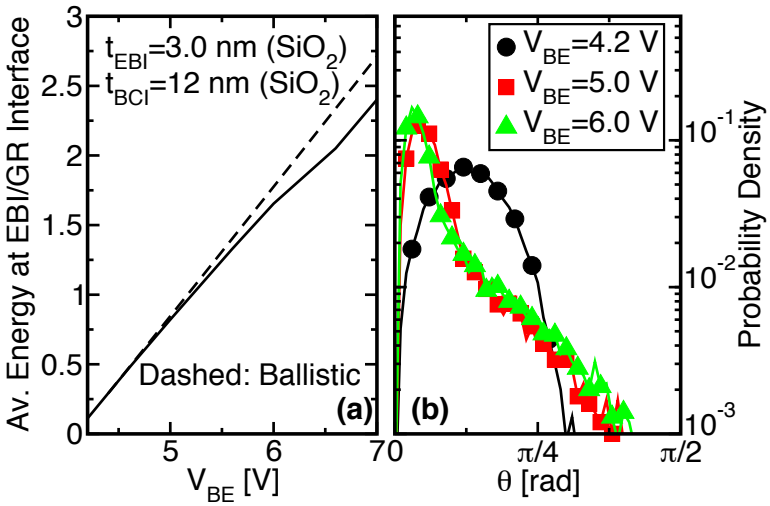

Figure 4.33: Electron energy (a) and probability distribution of the angle of incidence θ (inset in Fig. 4.27) (b) at the EBI/GR interface (x=0 in Fig. 4.27). Ballistic electron transport is reported as a reference in plot (a) (dashed line).

Fig. 4.14 already showed that no drastic f_T drop is seen down to v_d=5·10^6 cm/s, reassuring us on the assumed drift velocity and on the possible impact of the v^d_{BCI} variations due to the different exploited BCI materials.

By considering again the GBT of Fig. 4.31, Fig. 4.33(a) shows the average kinetic energy of electrons at the EBI/graphene interface computed with (solid line) and without scattering (dashed line). Since the thickness of the EBI is quite limited, scattering induces only a small energy relaxation in the EBI layer. Fig. 4.33(b) reports the probability density of the angle θ (inset in Fig. 4.27) between the x axis and the electron velocity of the electrons hitting the EBI/graphene interface from the insulator side. By increasing V_{BE}, the distribution peak approaches θ=0, since the electric field strongly directs all the electrons toward the base.

Concerning the transport in the BCI, for increasing V_{BE}, the average kinetic energy of electrons entering the BCI is larger (Fig. 4.33(a)), hence, the average number of backscattering events in the BCI increases, consequently increasing I_B and reducing α_F (Fig. 4.34). In addition, by increasing the BCI thickness, the field in the BCI decreases, leading to more backscattering and further reducing α_F (Fig. 4.34(b)). This reduction, however, is modest as can be easily understood noting that in our model α_F is given by $(1-r)$, where $r = I_B/I_E$ is the backscattering coefficient in the BCI. For large α_F values, r is small and large percentage variations of r result in small percentage variation of α_F (e.g. by changing t_{BCI} from 10 nm to 20 nm, r varies by 28% whereas α_F by 6% only; see Fig. 4.34(b) at high V_{BE}).

As for the t_{BCI} dependence, by increasing the EBI thickness (t_{EBI}) for given V_{BE} and V_{CB}, α_F reduces as shown in Fig. 4.34(a), since the electrostatics of the device leads to a lower electric field in the BCI. Furthermore, optimized GBTs typically feature different materials for the EBI and BCI (see Sec. 4.6). In this case, by denoting with χ_{EBI} and χ_{BCI} the affinity of the EBI and BCI, respectively, a conduction band discontinuity ΔE=(χ_{BCI}-χ_{EBI}) is present at x=0 (Fig. 4.27). In this respect, for ΔE>0, the average kinetic energy of electrons entering the BCI and the fraction of electrons that suffer backscattering increase, further reducing α_F (Fig. 4.34(a), empty symbols). Hence, the use of dielectrics with very different affinities can be detrimental for α_F.

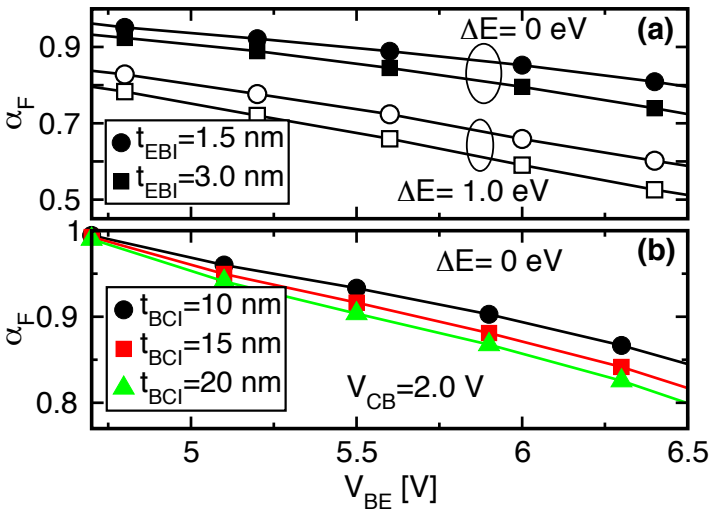

Figure 4.34: α_F versus V_{BE} for different EBI thickness (t_{EBI}) and ΔE for t_{BCI}=12 nm (a) and for different BCI thickness (t_{BCI}) with t_{EBI}=2.0 nm (b). In all the proposed configurations, SiO_2 parameters (Tab. 4.2) are used both for EBI and BCI, with the only exception of the open symbols in plot (a), which are obtained enforcing ΔE=1 eV by imposing a different affinity χ_{BCI}.

4.6 Optimization of GBT devices exploiting realistic dielectric materials

After the preliminary study of the GBT performance done in Sec. 4.3.3, we performed an exploration of the design space considering realistic materials for both the EBI and BCI, with the aim to maximize the RF GBT performance.

Table 4.3: Parameters used to simulate the optimized GBTs. m_I is the tunneling mass inside EBI and BCI to calculate the tunneling current. Collector metal is Ti.

	DEV. 1	DEV. 2	DEV. 3
Emitter	Si N_D [cm^{-3}] 10^{19}	Ti Φ_E^M [eV] 4.33	Si N_D [cm^{-3}] 10^{19}
EBI	Ta_2O_5	SiCOH	Ta_2O_5
BCI	Ta_2O_5	SiCOH	SiCOH
$\boldsymbol{m_I}$ [m_0]	0.5 Ref. [135, 136]	0.5	0.5
$\boldsymbol{k}$ [ε]	25 Ref. [137]	2.5 Ref. [138]	25 / 2.5
$\boldsymbol{\Phi_B}$ [eV]	0.36 Ref. [139]	0.53 Ref. [138]	0.36
$\boldsymbol{\Phi_C^M}$ [eV]	4.33	4.33	4.33
$\boldsymbol{t_{BCI}}$ [nm]	12	12	12

The analysis in Fig. 4.7(b) pointed out that dielectrics with large k values ensure large J_C for Si–emitters devices. Therefore, to design an optimized Si–emitter GBT structure, we selected Ta_2O_5 as EBI and BCI, because its large k value and the small conduction band (CB) offset with respect to silicon can boost the GBT performance [139]. We assume a Si emitter doping of N_D=10^{19} cm^{-3} and a BCI thickness of t_{BCI}=12 nm, that ensures that the Neutrality Point (NP) of graphene is positioned at relatively low V_{BE} (see Fig. 4.6).

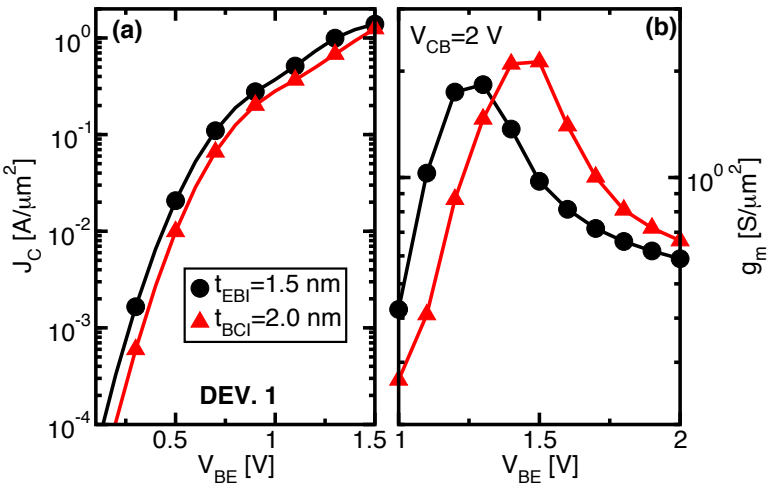

Figure 4.35: J_C (a) and g_m (b) as functions of V_{BE} for a few t_{EBI} in DEV. 1.

Figure 4.35 shows the calculated J_C (a) and the transconductance g_m (b) of the GBT described above (hereafter referred as DEV. 1). In particular, assuming $t_{EBI} \leq 2$ nm, J_C and g_m reach very large values. For $V_{BE} \geq 1.5$ V, J_C is rather independent of t_{EBI} since it is limited by the high current effects (h.c.e.) induced by the charge in the BCI. To simulate DEV. 1, we used the model parameters listed in Tab. 4.3.

Figure 4.7(a) shows that GBTs with metal emitter are expected to have better performance if low–k dielectrics are selected for the EBI and BCI layers (at least until h.c.e. do not start to degrade the GBT operation). Hence, to design an optimized metal emitter GBT (hereafter referred as DEV. 2), we select a low–k material for the insulators (i.e. SiCOH, [138]). Furthermore, we assumed Ti emitter and collector.

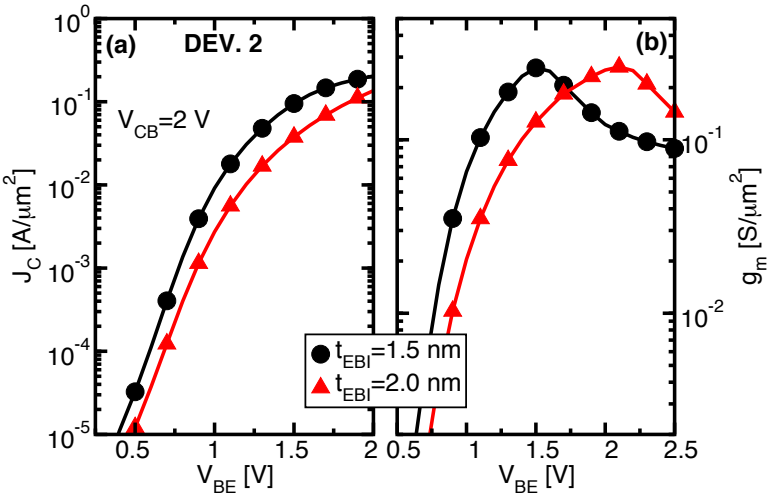

Figure 4.36: J_C (a) and g_m (b) of DEV. 2 as functions of V_{BE} for a few t_{EBI}.

Figure 4.36 shows J_C (a) and g_m (b) for DEV. 2, simulated by using the model parameters in Tab. 4.3. We note that, by assuming similar EBI and BCI thicknesses in the two devices, J_C and g_m of DEV. 2 are lower than in DEV. 1 (see Fig. 4.35). This is due, first, to the smaller tunneling barrier between Si and Ta_2O_5 (0.36 eV) than between Ti and SiCOH (0.5 eV) and, second, to the band bending in the Si emitter: it lowers the energy barrier height for the electrons that are

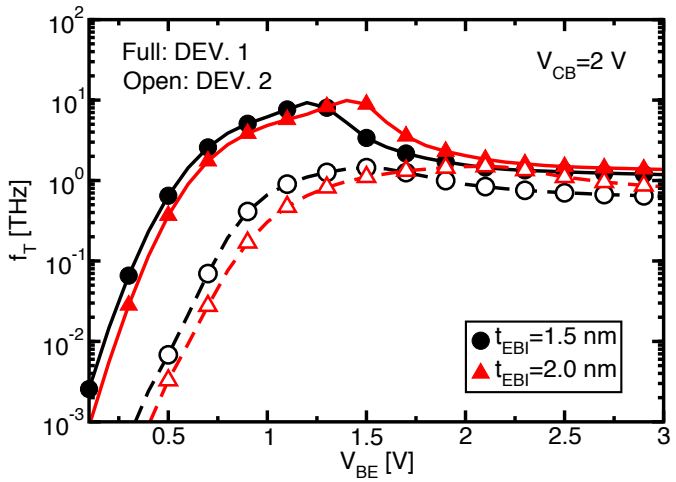

Figure 4.37: Comparison of f_T values of DEV. 1 (filled symbols) and of DEV. 2 (open symbols) as a function of V_{BE} for different EBI thickness.

tunneling at the emitter Fermi level (see Fig. 4.8), thus increasing J_C.

Figure 4.37 reports the simulated f_T for DEV. 1 (filled symbols) and DEV. 2 (open symbols). As it can be seen, DEV. 1 shows larger f_T values than DEV. 2 for similar EBI and BCI thicknesses. This reflects the larger current of DEV. 1. This latter shows f_T values up to 10 THz, but also for DEV. 2 THz operation is reachable by the intrinsic device.

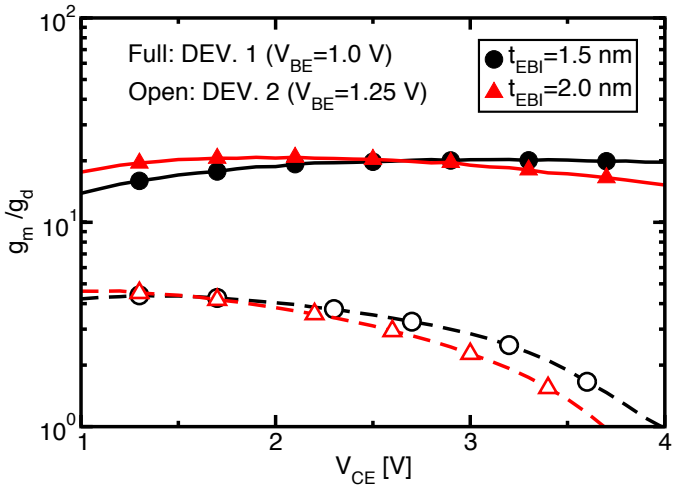

Figure 4.38: Intrinsic voltage gain g_m/g_d as a function of V_{CE} for a few values of the *EBI* thickness, for DEV. 1 (filled symbols) and DEV. 2 (open symbols) GBTs.

Furthermore, Fig. 4.38 compares the intrinsic voltage gains (g_m/g_d) and, now, DEV. 2 (open symbols) shows better results. In particular, the metal emitter GBT can reach a g_m/g_d of about 20, while for the Si emitter case, the gain is rather low (≈4).

In spite of the large g_m, the low intrinsic gain for DEV. 1 is due to the high output conductance g_d, that is much larger with respect to that of DEV. 2, as demonstrated by Fig. 4.39. Indeed, the use of a high–k BCI induces a large capacitance coupling between the collector and the base. The base potential can be largely influenced by the collector bias, thus increasing the output conductance of the device. This problem can be alleviated by integrating in the Si–emitter GBT structure a BCI with a lower k value, as demonstrated by Fig. 4.40, where we

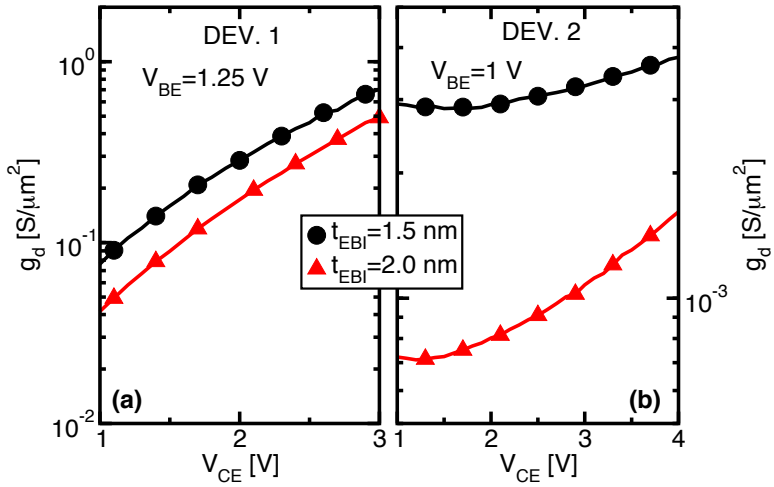

Figure 4.39: Output conductance g_d versus V_{CE} for DEV. 1 (a) and DEV. 2 (b).

simulated a Si emitter GBT with Ta_2O_5 EBI and SiCOH BCI (DEV. 3 in Tab. 4.3). The use of a low–k BCI increases g_d and, consequently, the gain. In fact, g_m/g_d for DEV. 3 is around 50 in the best case (Fig. 4.40(b), red triangles) that is one order of magnitude larger than for DEV. 1 (Fig. 4.38, open symbols). DEV. 3 also achieves a maximum f_T above 1 THz (Fig. 4.40(a)). In this case the lower dielectric permittivity of the BCI in DEV. 3 makes it more prone to h.c.e. than DEV. 1.

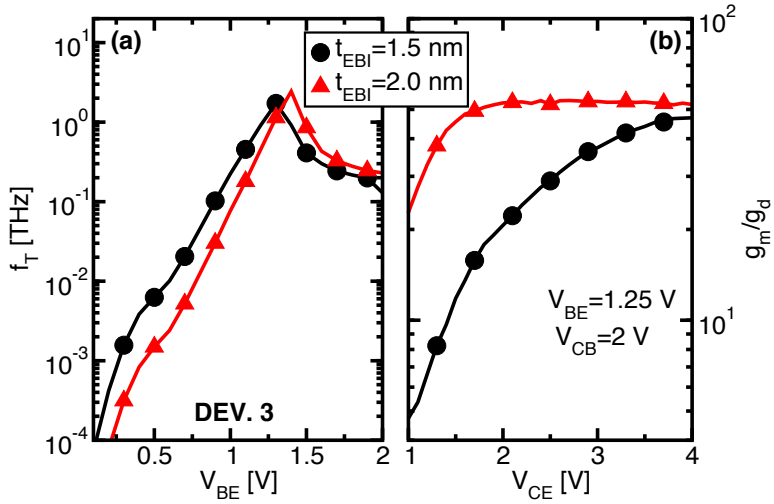

Figure 4.40: Cutoff frequency (a) and intrinsic gain (b) for DEV. 3.

4.7 Comparison with experiments

In this section we summarizes the comparisons between the simulation results and the available measurements, that have been done with the aim to verify and calibrate the developed models. In the beginning (Sec. 4.7.1) the model has been compared with the first GBT prototypes available in literature, while later, in Sec. 4.7.2, we report simulations of more advanced GBT exploiting bilayer stacks as EBI, namely engineered barriers that have been fabricated in order to overcome the poor performance of the first samples.

4.7.1 First GBT prototypes

The first experimental GBT devices have been fabricated at the Royal Institute of Technology (KTH) of Stockholm [30]. The samples have a structure formed by an n-doped silicon emitter, a silicon dioxide (SiO_2) EBI, an alumina (Al_2O_3) BCI and finally a titanium (Ti) collector. The doping concentration of the emitter is $N_D = 10^{15} cm^{-3}$. The fabricated GBT samples differ from each other by the base-collector oxide thickness (t_{BCI}) and by the area of the devices. The fabrication process is made to be compatible with the normal silicon CMOS technology: the silicon dioxide is grown thermally on the n-doped silicon emitter realizing the tunneling barrier, while the BCI is deposited on the monoatomic graphene layer and finally the metal collector is made with titanium/gold through evaporation. The silicon oxide (k_{EBI}=3.9) is grown on the silicon emitter, hence the electrons injected from the emitter see a Φ^B_{EBI}=3.1 eV base-emitter barrier, while the use of alumina (k_{BCI}=10) as base-collector oxides imposes a barrier height of Φ^B_{BCI}=2.68 eV, which are relatively high energy barriers with respect to those simulated in the previous sections. The whole parameters used to simulate these devices are listed in Tab. 4.4.

The first simulated device has a 5 nm base-emitter oxide thickness (t_{EBI}), while t_{BCI}=16 nm with an area of A=3600 μm^2. Figure 4.41 shows the comparison between the experimental

Table 4.4: Parameters used in the simulations of Figs. 4.41 and Fig. 4.42.

T	300 [K]
m_{EBI}, m_{BCI}	0.5 [m_0], 0.25 [m_0] Ref. [140]
k_{EBI}, k_{BCI}	3.9, 10 Ref. [141]
Φ^B_{EBI}, Φ^B_{BCI}	3.1, 2.68 [eV] Ref. [141]
m_E	$4\sqrt{m_t m_l} + 2m_t$
m_t	0.19 [m_0]
m_l	0.919 [m_0]
N_C	$2.800 \cdot 10^{19}$ [cm^{-3}]
N_V	$1.040 \cdot 10^{19}$ [cm^{-3}]
ε_E	11.7 [ε_0]
χ_E	4.05 [eV] (Silicon)
Φ^M_C	4.33 [eV] (Titanium)

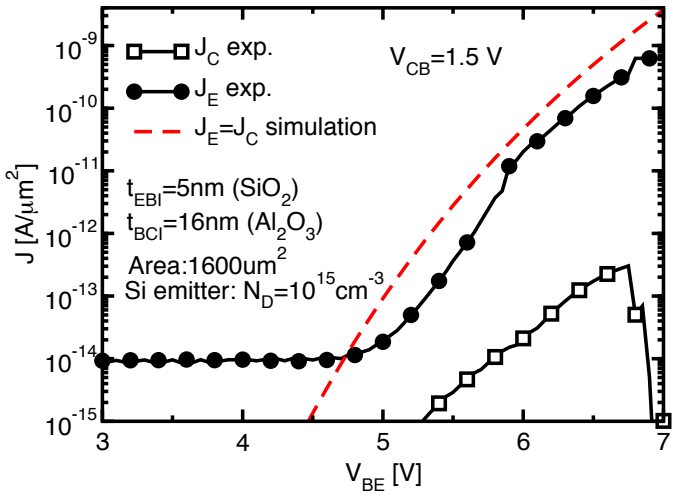

Figure 4.41: Comparison between an experimental device and the model: collector current J_C and emitter current J_E as a function of V_{BE} for a few biases V_{CB}.

currents and the simulated ones as a function of the base–emitter voltage. In the experiments, we can see that the emitter current increases rapidly after a certain V_{BE} bias: we identify in this point the typical transistor threshold voltage and it indicates the voltage at which the electrons injected from the emitter see a small tunneling barrier to allow a significant current flux; under these conditions the Fowler–Nordheim phenomenon is taking place. This leads to a high I_{ON}/I_{OFF} state ratio. As already mentioned in Sec. 4.5, these first measurements highlight that the emitter current is a few orders of magnitude larger than the collector current. This suggests that the base current actually is not negligible at all and it has a strong influence on the output collector current. Unfortunately, this is a general trend in all the fabricated prototypes, that need to be improved in the next fabrication runs (see Sec. 4.7.2). Consequently, in Fig. 4.41 we see that the simulated collector current is far from the measured one (since we are neglecting the base current $J_C = J_E$), even though the trend and the profile of the curves is quite similar. Hence, the most interesting comparison is that between the emitter currents; indeed, in this case, the simulated J_E is close to the experiment, with very similar trends, thus verifying our tunneling model. The good agreement between the measured and simulated J_E indicates that the base current is mostly due to the capture in graphene of the electrons injected from the emitter rather than the hole injection from the base.

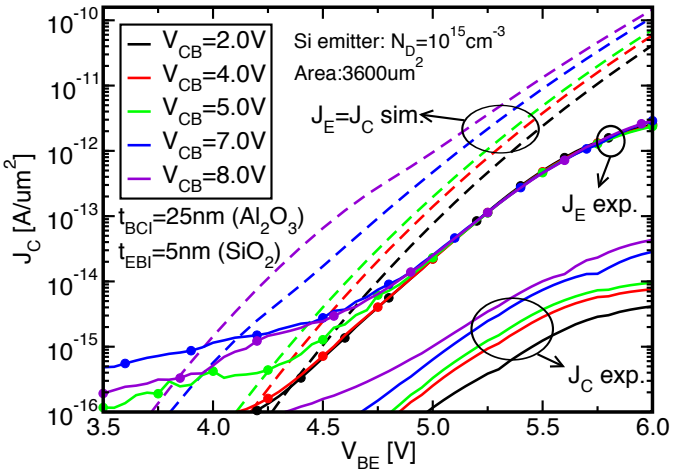

Figure 4.42: Comparison between the experimental [30] and simulated current densities as a function of V_{BE}. Model parameters are reported in Tab. 4.4.

Figure 4.42 shows again the experimental currents as a function of V_{BE} for a few values of V_{CB} for a second GBT with 25 nm of Al_2O_3 as BCI. Although worse that Fig. 4.41, the agreement between the simulated currents and the measured J_E is satisfactory. Again, the sample shows very large J_B and J_C cannot be reproduced by the model. From this largest set of measurements, we calculated the α_F values (Fig. 4.43(a)) that can be simulated with Monte Carlo simulator presented in Sec. 4.5, in order to evaluate the impact of the electron backscattering on the formation of the base current. The used scattering parameters are reported in Tab. 4.2, for both the SiO_2 EBI and the Al_2O_3 BCI, where the Al_2O_3 acoustic phonon scattering deformation potential C_{ae} is tentatively set equal to that of SiO_2.

Simulated α_F are reported in Fig. 4.43(a). Similarly to Fig. 4.34, as V_{BE} increases, the kinetic energy of the electrons entering in the BCI conduction band increases, thus enhancing the probability of the electron to be backscattered in the graphene base. On the other hand, by increasing V_{CB}, the increase of the BCI electric field favors the electron drift toward the collector terminal, leading to higher α_F. Such V_{BE} and V_{CB} dependencies are consistent with those of the experimental α_F (Fig. 4.43(b)) [30]. However, these latter values ($10^{-3} \div 7{\times}10^{-2}$

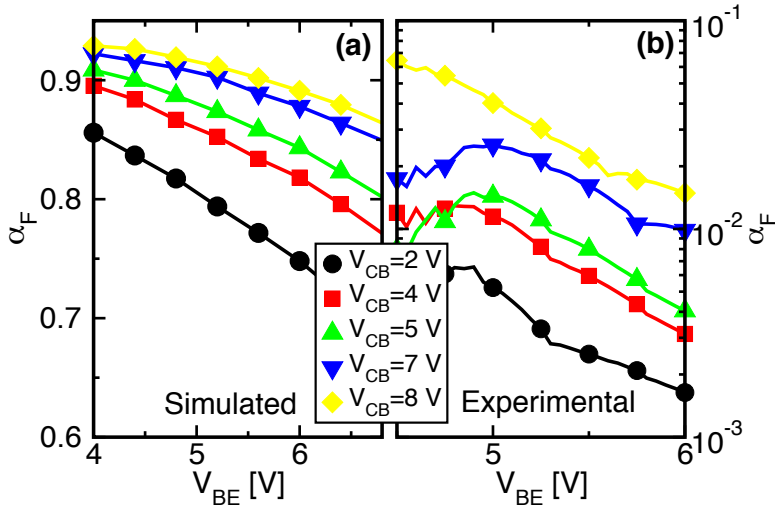

Figure 4.43: Simulated (a) and experimental (b) α_F as a function of V_{BE} for the GBT reported in Figs. 4.42. Material parameters used in the simulations are listed in Tab. 4.2.

[30, 77]) are much lower than the calculated α_F values ($0.5 \div 0.9$, Fig. 4.43(a)). Anyway, the simulated α_F are still small enough to pose a severe limit to the GBT static performance.

If the scattering probability in the BCI is increased by choosing C_{ae} as high as 10 eV, we see a decrease of α_F (compare triangles vs. circles in Fig. 4.44(a)), but not enough to match the measurements. Moreover, the dependence of α_F on V_{CB} becomes weaker (Fig. 4.44(b)), since the larger probability of backscattering due to the increase of C_{ae} contrasts the effect of the higher electric field, but this is in contrast with the experimental trend. Hence, this C_{ae} increase is not a viable strategy to match the measurements.

We also tried to increase the conduction band mass in Al_2O_3 up to $0.6m_0$ (possibly justified by the large electron–phonon coupling in Al_2O_3 [133, 142]) that indeed lowers α_F, but again not enough to match the experiments, as illustrated in Fig. 4.45. This indicates that backscattering is important for the I_B formation but it is not the only component that contribute to the very low measured α_F, at least for these GBT devices.

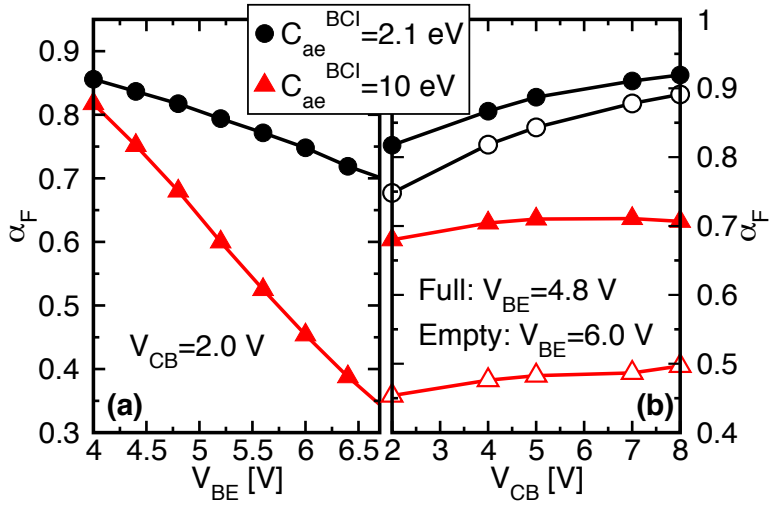

Figure 4.44: Simulated α_F as a function of V_{BE} (a) and V_{CB} (b) for the GBT of Fig. 4.42. C_{ae} of BCI is used as a free parameter.

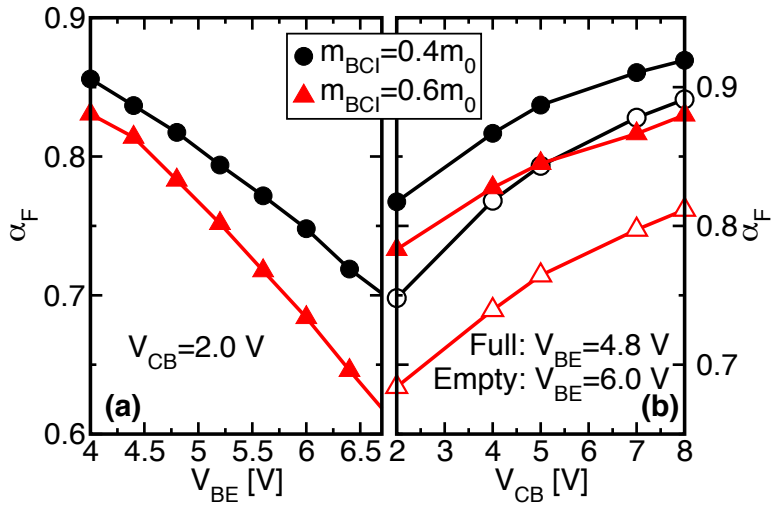

Figure 4.45: Simulated α_F as a function of V_{BE} (a) and V_{CB} (b) for the GBT of Fig. 4.42. In this case, m_{BCI} is used as a free parameter.

4.7.2 GBT devices with bilayer EBI

Due to the poor collector current achievable by the first GBT prototypes (Sec. 4.7.1), in [61], bilayer tunnel barriers have been proposed as EBI for GBTs, where a thin interface layer (IL) is combined with a thick low–barrier dielectric (LBD) [61, 113]. Fig. 4.46 shows the conduction band diagram along the transport direction of this improved GBT structure.
We remind that bilayer tunnel barriers can improve the ON/OFF tunnel current ratio and the

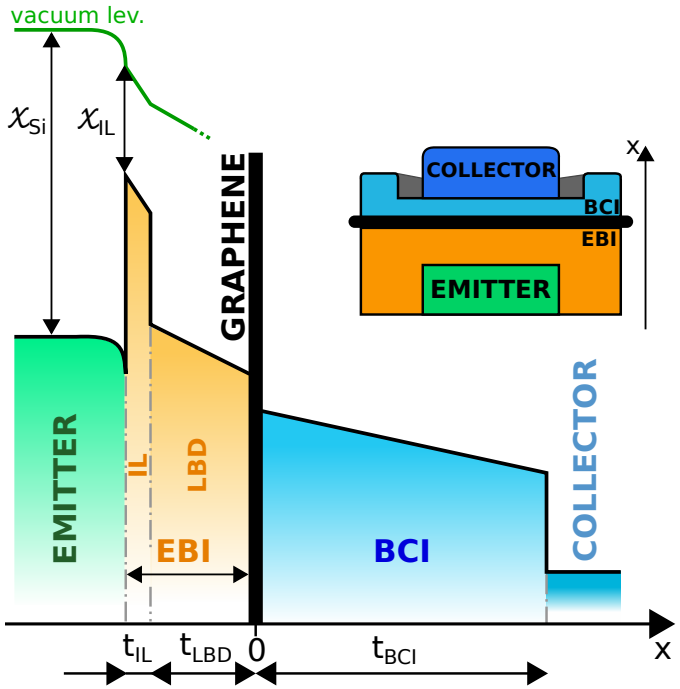

Figure 4.46: Conduction band diagram along the GBT structure. The EBI stack is made of a thin high–barrier interfacial layer (IL) and a thicker low–barrier dielectric (LBD). The inset shows the sketch of the device cross section.

program/retention performance of non–volatile memories [143, 144]. When the GBT is switched off (small V_{BE}), the thick LBD prevents tunneling (see Fig. 4.47(a)). For large V_{BE}, instead, due to the band bending that pushes down in energy the conduction band (CB) of the LBD, the emitter electrons cross a very thin tunnel barrier (the IL alone, Fig. 4.47(b)), thus resulting in very large emitter currents. Furthermore, concerning the BCI, the use of amorphous Si improves the α_F value with respect to the first GBT prototypes (see Sec. 4.7.1) featuring high–k dielectrics [30, 31, 61, 77], because of the much smaller actual tunnel barrier. Cristalline silicon should give even better results but the immaturity of chemical vapor deposition of Si still prevents to achieve high quality silicon films on top of graphene [145].

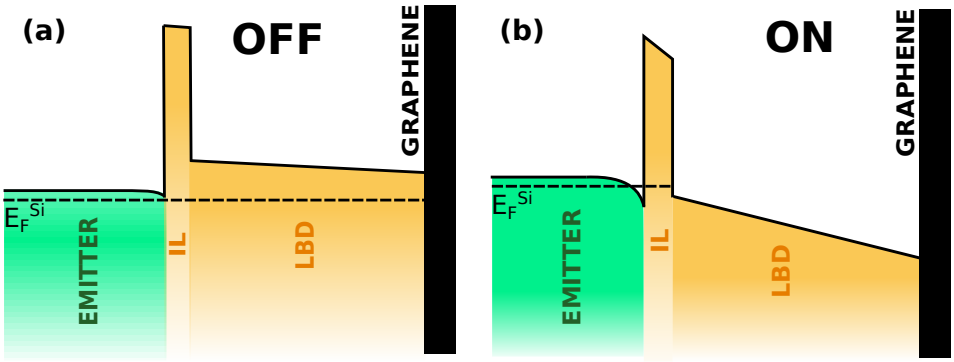

Figure 4.47: Conduction band diagram at the emitter/EBI interface during the OFF–sate (a) and ON–state (b). When V_{BE} is not sufficiently high, electrons from the injection level of the emitter (dashed line) face a very thick energy barrier due to both the IL and LBD (b), avoiding the electron tunneling. During the ON–state instead (a), the applied V_{BE} is such as to lower the LBD under the emitter injection level. Hence, injected electrons from the emitter face with the only very thin IL energy barrier, consequently increasing the collector current.

Thin thulium silicate (TmSiO) or SiO_2 (0.5 nm) films have been grown as IL. TmSiO is a high quality dielectric that ensures a good interface to the Si emitter [146]. As for the LBD, TiO_2 and Al_2O_3 have been used because of their large electron affinity (i.e. small tunnel barrier) and high relative permittivity (small electrical thickness) [147]. The Si/TmSiO/TiO_2/graphene stack has also been used to fabricate both Si/EBI/graphene capacitor (SIG) and a complete GBT structure by adding the amorphous Si layer as BCI [146]. As stated above, amorphous Si (a–Si) yields a very small tunnel barrier with respect to the emitter, thus favoring the electron transport. Table 4.5 summarizes the nominal structure parameters of the SIG, Si/Insulator/Metal (SIM) capacitors and GBT samples measured in [31]. All the samples and the corresponding electrical characteristics have been fabricated and done in KTH of Stockholm.

To calculate the I–V characteristics of the test structures, we improved the electrical model of Sec. 4.3. We extended the model to handle EBI stacks featuring two dielectric layers. In order to simulate the simple SIG structures, we just remove the contribution of the BCI section to the electrostatics and the current of the device. To simulate the SIM stacks, instead, we use the tunnel model for MOS structures of [148]. To have a complete overview of the performance of these alternative structures, we later calculate the α_F=I_C/I_E by means of the Monte Carlo simulator presented in Sec. 4.5. Concerning the transport in the BCI, this latter is modeled as crystalline silicon, accounting for scattering with inter–valley optical phonons and intra–valley acoustic phonons [149] and neglecting possible grain boundary related collisions. This assumption leads to underestimate the scattering rate, but the calculation is nevertheless useful because the final aim in the GBT fabrication is to grow a crystalline Si BCI, in order to minimize the backscattering and optimize the device structure [145]. The scattering rates in crystalline

Table 4.5: Dielectrics materials and their nominal thickness used in the fabricated test structures.

Label	Type	IL		LBD		BCI
		Material	t_{IL} [nm]	Material	t_{LBD} [nm]	t_{BCI} [nm]
SIG–1L	SIG	TmSiO	1.0	–	–	–
SIG–2L	SIG	TmSiO	1.0	TiO_2	5.5	–
SIM–A1	SIM	SiO_2	0.5	Al_2O_3	1.5	–
SIM–A2	SIM	SiO_2	0.5	Al_2O_3	3	–
SIM–T1	SIM	SiO_2	0.5	TiO_2	4	–
SIM–T2	SIM	SiO_2	0.5	TiO_2	8	–
GBT–E	GBT	TmSiO	1.0	TiO_2	5.5	60

Si are calculated as [149]:

$$S_{acu} = \left(\frac{2\pi k_B T D_{ac}^2 q^2}{\hbar \rho v_S^2}\right) \cdot \sqrt{\left(\frac{2m_{eff}}{\hbar}\right)^3} \cdot \frac{\sqrt{qE}}{4\pi^2} \tag{4.41}$$

$$S_{opt}^{abs} = \left(\frac{\pi D_{opt}^2 \hbar n_{opt}}{\rho E_{opt}}\right) \cdot \sqrt{\left(\frac{2qm_{eff}}{\hbar}\right)^3} \cdot \frac{\sqrt{E+E_{opt}}}{4\pi^2} \tag{4.42}$$

$$S_{opt}^{em} = \left(\frac{\pi D_{opt}^2 \hbar (n_{opt}+1)}{\rho E_{opt}}\right) \cdot \sqrt{\left(\frac{2qm_{eff}}{\hbar}\right)^3} \cdot \frac{\Re\{\sqrt{E-E_{opt}}\}}{4\pi^2}, \tag{4.43}$$

where $m_{eff} = m_0 \sqrt[3]{0.19^2 \cdot 0.916}$ kg is the electron effective mass, $D_{ac} = 9$ eV is the acoustic deformation potential, ρ=2329 kg/m^3 is the density, v_s=9040 m/s is the sound velocity, D_{opt}=1.1 $\times$ 10^{11} eV/m is the optical deformation potential, E_{opt}=63 meV is the optical phonon energy while $n_{opt} = 1/[\exp(qE_{opt}/(k_B T)) - 1]$ is the Bose–Einstein statistics. The electron wave–vector after the scattering event is determined considering the Vogt–Herring transformation for ellipsoidal bands:

$$k_x^f = |k^f| \cos(\phi) \sin(\theta) \sqrt{m_x/m_{eff}} \tag{4.44}$$

$$k_y^f = |k^f| \sin(\phi) \sin(\theta) \sqrt{m_y/m_{eff}} \tag{4.45}$$

$$k_z^f = |k^f| \cos(\theta) \sqrt{m_z/m_{eff}}, \tag{4.46}$$

where $|k^f| = \sqrt{2m_{eff} q E_f (1+\alpha E_f)}/\hbar$ is the final wave-vector after scattering, ϕ is the azimuth angle randomly taken in the range $[0 \div 2\pi]$ while θ is the polar angle.

To calibrate the tunnel model, we first study the current–voltage characteristics of the SIG structures. Figure 4.48 reports the measured current density (J, symbols) of the SIG capacitors with a TmSiO single layer dielectric (SIG–1L, (a)) and with a double layer TmSiO/TiO_2 stack (SIG–2L, (b)) for different temperatures. We see that, for low applied biases (V_{BE}<1.5 V), the LBD in the SIG–2L stack largely reduces the current with respect to the SIG–1L structure. At large voltage (V_{BE}>2 V), instead, the two samples show similar J values, thus confirming that in this regime the current is limited only by the thin IL, supporting the working principle of the dual layer tunnel barrier proposed in [61].

The SIG–1L data (Fig. 4.48(a)) is used to calibrate the model parameters for the TmSiO layer and a good agreement between the model and the experiments is achieved (also over

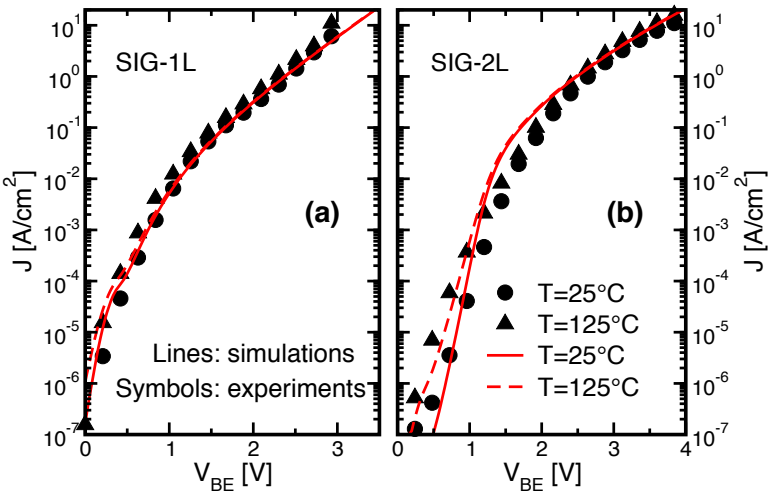

Figure 4.48: Measured and simulated J–V characteristics at different temperatures (T) of SIG structures with a TmSiO single layer (a) and a TmSiO/TiO_2 double layer stack (b) as dielectrics.

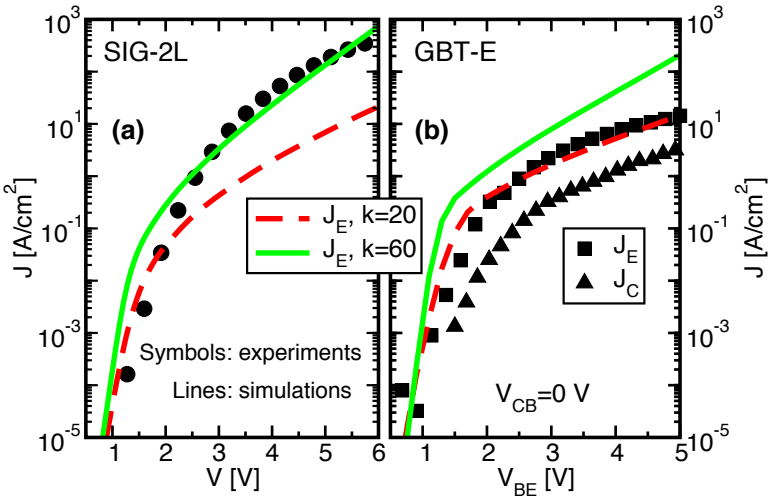

Figure 4.49: Measured and simulated J–V characteristics of the Si/TmSiO/TiO_2/graphene capacitor (a) and of the GBT fabricated starting from the very same SIG stack as EBI and by growing a 60 nm a–Si BCI on top (b). T=300 K.

temperature) by using an electron affinity of χ=1.1 eV, a tunnelling mass of m^T=m_0 (m_0 being the free electron mass) and a relative permittivity of k=12 [146]. A better fit of the experiments has been achieved by increasing the IL thickness to t_{IL}=1.2 nm with respect to a nominal thickness of 1 nm (see Tab. 4.5), which is compatible with the control limits of the deposition process.

Having obtained the TmSiO parameters, we extract the TiO_2 parameters by comparing the model with the SIG–2L measurements. Fig. 4.48(b) shows the good agreement between the model and the experiments when using a TiO_2 electron affinity of χ=3.8 eV and m^T=m_0 [150, 151]. The TiO_2 relative permittivity is set to k=60 [152]. The extracted parameters have been confirmed also by the comparison between the model and the measurement on a second SIG–2L sample (Fig. 4.49(a)). In particular, for k=60, the model (solid green line) reproduces correctly the slope of the experimental J–V curve (symbols).

After being measured, the very same SIG–2L structure in Fig. 4.49(a) was used to fabricate a

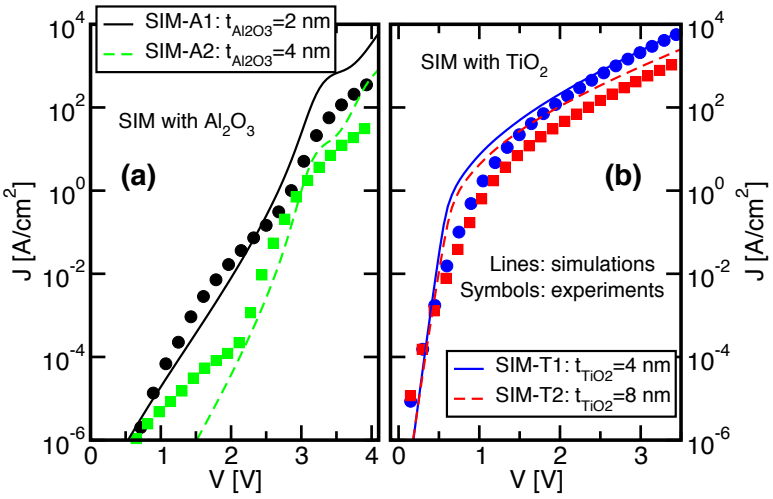

Figure 4.50: Comparison between experiments and simulations of SIM structures exploiting SiO_2 as interfacial dielectric. The reported thicknesses are those that allowed us to reproduce the experiments. The metal is Ti. T=300 K.

complete GBT, by growing, as BCI, a 60 nm a–Si layer on top of the graphene (GBT–E, Tab. 4.5) [61]. Fig. 4.49(b) shows the emitter and collector current densities (J_E and J_C, respectively) measured on the final device. The simulated J_E (dashed red line) reproduces well the experiment (squares) by reducing only the TiO_2 permittivity to k=20, while maintaining the other model parameters as extracted from Fig. 4.48. The model cannot reproduce the measurements by using a set of parameters that preserves the k=60 extracted in Fig. 4.49(a). Since the TiO_2 electrical characteristics are strongly process dependent [152], the TiO_2 permittivity reduction between the SIG–2L and the GBT structure may be ascribed to the additional deposition steps and thermal budget required to grow the a–Si BCI. Alternatively, this parameter variation may be representative of other physical/electrical phenomenon (e.g. additional series/sheet resistance due to the graphene degradation during the Si deposition process) that attenuates the voltage drop across the EBI, reducing consequently I_E. In summary, the a–Si deposition decreases the GBT current with respect to the SIG structure and, clearly, the BCI growth needs to be optimized to maintain the electrostatics that ensures large GBT currents (Fig. 4.49(b), green solid lines) [145, 153].

Nevertheless, it is also worth evaluating the potentialities of alternative dual layer EBI stacks that could further boost I_E. Fig. 4.50 compares experiments and simulations of SIM structures which integrate SiO_2 as interfacial layer, instead of TmSiO. The LBD is Al_2O_3 (Fig. 4.50(a)) or TiO_2 (b). The kinks in the J–V curves of Fig. 4.50 are typical of the dual layer tunnel barriers [143]. The simulations (lines) reproduce the experiments (symbols) by using t_{IL} values in the range 0.8–1.2 nm, once again slightly thicker than the nominal thickness (0.5 nm, Tab. 4.5). This result suggests an overgrowth of the IL during the fabrication of the LBD. Furthermore, the good agreement in Fig. 4.50(b) was obtained by using the same TiO_2 nominal thickness and model parameters calibrated on SIG samples. In Fig. 4.50(a) we extracted χ=1.7 eV and m^T=0.4m_0 for Al_2O_3, consistently with [147], and we used t_{Al2O3}=2 nm and t_{Al2O3}=4 nm for the Al_2O_3 thickness of SIM–A1 and SIM–A2, respectively, instead of the nominal thicknesses of 1.5 and 3 nm (see Tab 4.5).

The current values of the SIM structures in Fig. 4.50 are larger than those of the SIG samples, despite similar IL thicknesses. This is due to the smaller tunnel mass in SiO_2 (m^T=0.5m_0, [147]) than in TmSiO. Hence, also these stacks, and especially the SiO_2/TiO_2 one, are possible good

candidates for the EBI of high performance GBTs.

Fig. 4.49(b) shows that the experimental J_C is a small fraction of J_E, leading to α_F values around 0.2 at V_{CB}=0 V [61]. Although much larger than those measured in Sec. 4.7.1 and also reported in previous literature [30, 77] and not far from that of MoS_2 based transistors measured under similar bias conditions [154], this α_F value reveals that the base current is again very large. Since a possible contribution to the base current is the backscattering of electrons injected into the CB of the BCI, again we studied the electron transport through this GBT by means of the developed MC model of Sec. 4.5. TiO_2 optical phonon energies were set to $\hbar\omega_{LO1}$=108.6 meV and $\hbar\omega_{LO2}$=45.4 meV [155], while for the BCI, we used the standard phonon scattering parameters for bulk Si [149].

Figure 4.51 shows the average electron velocity (v_{avg}) along the transport direction (x, Fig. 4.46) of the GBT–E for a few V_{BE} values. x=0 marks the position of the graphene base. At V_{CB}=0 V (Fig. 4.51(a)), v_{avg} is essentially constant along the BCI (x>0) and rather independent on V_{BE}, with a value in the order of 10^7 cm/s (see Sec. 4.5 [156]), again very similar to the electron drift velocity assumed in the GBT electrical model of Sec. 4.3.4 when accounting for the space charge effects. Instead, for V_{CB}=4 V (Fig. 4.51(b)), v_{avg} shows an overshoot near the graphene/BCI interface at small V_{BE}, due to the BCI electric field that favors the electron motion. For large V_{BE}, no overshoot is seen because of the high energy and, thus, large collision rate of the electrons entering the BCI, that limit v_{avg}.

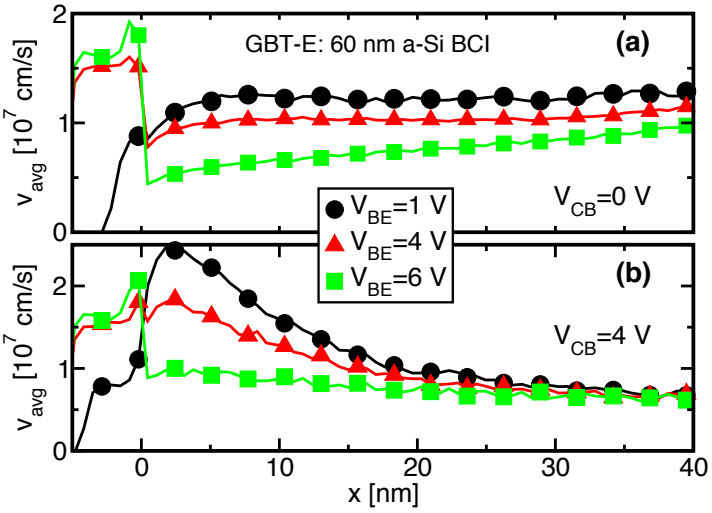

Figure 4.51: Monte Carlo simulation of the electron average velocity along the transport direction in the GBT with a 60 nm a–Si BCI for V_{CB}=0 V (a) and V_{CB}=4 V (b). x=0 is the position of the graphene base.

Figure 4.52 shows the α_F values (dashed line) calculated from the experiment of Fig. 4.49(b) and from the MC simulations (symbols). For low V_{BE}, the model (circles) cannot reproduce the experimental α_F, most probably because we are neglecting the direct capture of the electrons by the graphene base. At large V_{BE}, instead, that is when the electrons are injected with high energy in the BCI, the simulation matches the measurement. This trend suggests that, at *large electron energy*: i) backscattering is mostly responsible for the α_F degradation; ii) the direct capture of the electrons by the graphene layer is much smaller than that at low energy, consistently with the experiments in [157].

The common–base current gain is enhanced at large V_{CB} (Fig. 4.52, squares) [156, 154] and/or for reduced BCI thickness (triangles). Indeed, by increasing the BCI electric field, the electron drift towards the collector is favoured (Fig. 4.51) and by thinning the BCI, carriers suffer

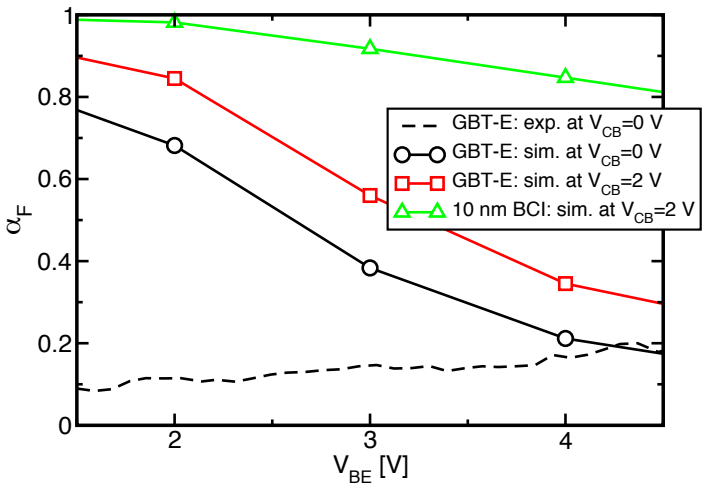

Figure 4.52: Comparison between the experimental α_F (dashed line) and the MC model at V_{CB}=0 V (circles). Simulations at $V_{CB} = 2V$ are also reported (squares). The triangles are simulations of a GBT similar to GBT–E but with a BCI thickness reduced to 10 nm.

Table 4.6: Model parameters used to simulate the considered GBT structures with bilayer EBI.

	EBI						**BCI**
	IL			**LBD**			
Label	Mat.	t_{IL} [nm]	χ [eV]	Mat.	t_{LBD} [nm]	χ [eV]	t_{BCI} [nm]
GBT–E	TmSiO	1.2	1.1	TiO_2	5.5	3.8	60
GBT–A	SiO_2	1.0	0.95	Al_2O_3	2	1.7	10
GBT–T	SiO_2	1.2	0.95	TiO_2	4	3.8	10
GBT–O1	TmSiO	0.8	1.1	TiO_2	3	3.8	10
GBT–O2	SiO_2	0.5	0.95	TiO_2	4	3.8	10

less scattering events before reaching the collector, thus reducing the backscattering probability (see also Fig. 4.34(b)). This creates an opportunity to optimize the GBT structure/bias to limit backscattering in BCI and thus to reach competitive α_F values above 0.9 [154].

After the calibration of the material parameters in Figs. 4.48, 4.49 and 4.50, we simulated the RF performance of the GBT–E. Fig. 4.53 shows the f_T versus J_C curves of the GBT–E for two V_{CB} values (open and filled circles). To calculate J_C we used the experimental α_F values of Fig. 4.52. As it can be seen, the device reaches f_T values up to at most one MHz, because of the very limited emitter current J_E and the small α_F value, that reduces the collector current.

To improve J_C and, hence f_T, we designed and simulated template GBT structures with optimized bilayer EBI stacks and BCI layer. Tab. 4.6 reports the layer thicknesses and the model parameters (from Figs. 4.49 and 4.50) used to simulate the RF performance. Note that the BCI thickness of these devices is 10 nm, much thinner than that of GBT–E, in order to improve the α_F value. We simulated these GBTs by considering $\alpha_F \simeq 1$, that is close to the simulations of Fig. 4.52 (triangles).

The optimized GBT–A and GBT–T feature SiO_2/Al_2O_3 and SiO_2/TiO_2 tunnel barriers, respectively (see Tab. 4.6), because the SIM samples fabricated with these materials show very large tunnel currents. As shown in Fig. 4.53, GBT–A and GBT–T reach much larger f_T values than GBT–E and, in particular, GBT–T exhibits a cutoff frequency up to 10 GHz (filled

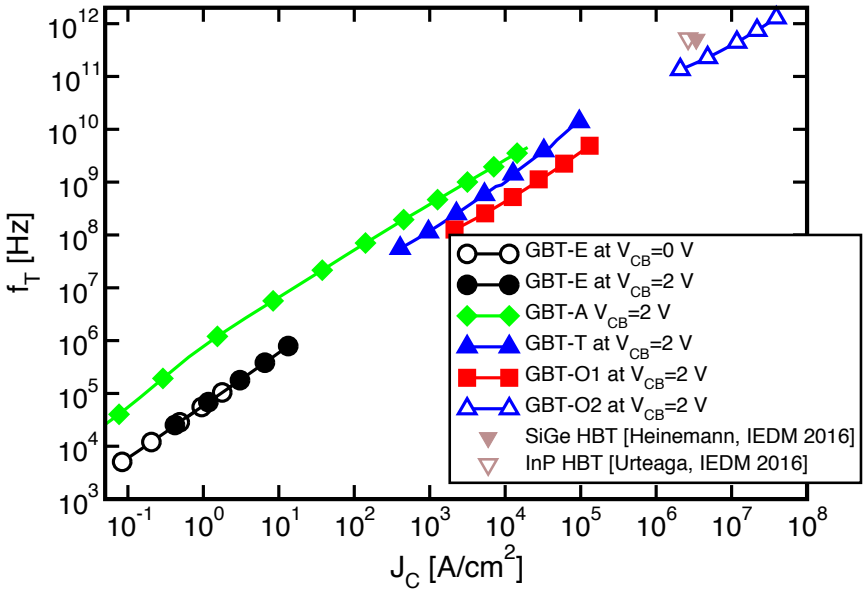

Figure 4.53: Cutoff frequency as a function of J_C for the GBT configurations listed in Tab. 4.6. Experimental data of maximum cutoff frequency achievable by recent HBT devices [158, 159] are also reported for comparison.

triangles).

To thoroughly evaluate the potential of GBTs based on the TmSiO/TiO_2 EBI, we simulated also an optimized template GBT with a TmSiO IL scaled to a realistic thickness of 0.8 nm [146] (GBT–O1, Tab 4.6). GBT–O1 shows f_T values of the same order of magnitude as GBT–T, but the cutoff frequency does not overcome the 10 GHz limit (Fig. 4.53, squares).

Finally, we also designed a GBT with an optimized EBI stack with a SiO_2 IL scaled to an aggressive value of 0.5 nm (GBT–O2, Tab 4.6). The model (Fig. 4.53, open triangles) shows that the GBT–O2 structure can achieve very large J_C and f_T values and, in particular, the cutoff frequency reaches one THz, demonstrating the great potentialities of GBTs based on this optimized EBI stack. It is worth nothing that, the f_T roll–off typical of space charge effects is not visible in the range explored by the simulations of Fig. 4.53 because of the relatively low permittivity of the Si BCI, that limits the effect of the travelling charge (see Sec. 4.3.5). This also contributes in obtaining large f_T values.

From the trend of f_T as a function of J_C shown in Fig. 4.53, it is clear that very high current values are required to reach the THz range. However the GBT characteristics are comparable with those of recent HBT devices (down triangles in Fig. 4.53 [158, 159]), which actually require collector currents in the order of tens of mA/μm^2 to achieve $f_T \simeq$0.5 THz (see also Fig. 4.18). Therefore, from this observation, we can predict that GBTs will show requirements in terms of current similar to those of competing devices to reach the THz operation, while showing much smaller space charge related effects.

4.8 Conclusion

In this chapter we introduced the structure and the operation principle of the vertical Graphene–Base–Transistor (GBT). We then moved to illustrate the developed electrical model of GBT devices, implementing silicon as well as metal emitter devices and estimating DC and RF performance. We initially gave first guidelines for the choice of the dielectric permittivity (k) of

the emitter–base insulator (EBI). In fact, low–k materials are preferred for metal emitter GBTs, while high–k materials lead to better performance in silicon emitter case.
We later integrated the model taking into account the effect of the high space charge effects, occurring at high current levels and limiting the maximum achievable cutoff frequency (f_T). The f_T calculation shows that high current effects are not very critical for GBTs, mainly for the reduced thickness of the base–collector insulator (BCI), and Terahertz (THz) operation are anyway achievable by the intrinsic device. The effect of the graphene/metal contact resistance, strongly impacting the RF performance in graphene–based devices, has been also included, investigating on its influence on the unity power gain of the GBT.
The developed model has been compared with a simulator based on Non–Equilibrium Green Function developed at the University of Bologna. In spite of the significant differences between the two modelling approaches, the agreement is satisfactory, validating our simulator.
Furthermore, we developed a Monte Carlo simulator to investigate on the electron scattering inside the dielectrics of GBT devices, verifying that the electron drift velocity is rather constant inside the BCI and in the order of 10^7 cm/s, validating the important assumption previously made in modelling high current effects.
The electrical model has been used to explore the design space of the GBT, assuming realistic dielectric parameters. In particular, in order to have the best combination among the considered RF figures of merit, we optimize the GBT structure by combining a silicon emitter and a high–k EBI to favor the electron tunneling. At the same time, we used a low–k BCI to achieve low output conductance and, consequently, high intrinsic voltage gain.
The last section of the chapter is instead devoted to the benchmarking of our simulators against experimental measurements. First, concerning the comparison with conventional GBT prototypes, the electrical model gives reasonably good agreement with the experimental emitter current. Since the huge measured base current, the developed Monte Carlo model has been used to investigate on the impact of the electron backscattering by the BCI on the formation of the base current. Even accounting for the uncertainties on material scattering parameters, it is not possible to reconcile simulations with experiments, indicating that other physical mechanisms are responsible of the formation of the base current, but demonstrating the strong impact of the electron backscattering on the common–base current gain (α_F).
Advanced GBT devices exploiting bilayer dielectric stack as EBI have been also simulated by means of both the electrical model and the Monte Carlo simulator. Simulations of the common–base current gains pointed out how at large base–emitter biasing the electron backscattering becomes the main limiting factor for the α_F. Finally, simulations of optimized GBTs exploiting engineered tunneling barriers and based on realistic technology have been performed, confirming that the achievement of THz roperation is feasible for GBTs.

Conclusion and Future Work

Because of its outstanding properties, graphene has caught the attention of the scientific community. In particular, the high carrier mobility observed in suspended monolayer graphene is very interesting for nanoelectronic devices [36]. Graphene–Field–Effect–Transistors (GFETs) have been extensively investigated for high–performance RF applications, enabling the achievement of cutoff frequencies (f_T) exceeding 400 GHz within a few years [11, 12]. Despite this incredible quick progress, the absence of an energy bandgap in graphene limits their RF performance, because of the non–saturated trend of the device output characteristics. A further major drawback of GFETs is represented by the source (S) and drain (D) contact resistance, which severely reduces the extrinsic transconductance due to the non–ideal metal/graphene contact [16, 81]. The latter, because of the technological issues in chemically doping the graphene [95], is normally used to control the polarity of S/D regions via electrostatic doping [96]. Hence, it is fundamental to account for these peculiarities of metal/graphene contact in the GFET simulation tools, in order to provide reliable predictions of the device performance.
For this reason, we extended the Monte Carlo transport simulator for GFETs developed at the University of Udine [29], first implementing the effect of the metal/graphene Schottky contact on the GFET electrostatics. A one–dimensional physics–based model has been developed to describe the metal/graphene stack, also introducing an insulating layer to model the phenomena occurring at the interface between the two materials. The Monte Carlo (MC) simulations predict similar values of current for chemically and electrostatically doped GFETs, providing for the performance of the GFETs using metal S/D contacts on top of undoped graphene.
We included the effect of the series resistance directly in the MC self–consistent loop, by means of an efficient implementation that allows to save time with respect to previous used approaches, which are based on the construction of the look–up tables through a large simulation set [88]. Instability issues, related to the mutual dependence between the transport simulation and the electrostatics solver, have been tackled by the introduction of a damping algorithm in order to limit the variation of the current at every iteration of the MC simulator.
To calibrate the simulation tools, reliable characterization technique to estimate the metal/graphene contact resistance are needed. We investigated the so–called end–contact resistance method, based on the commonly used transmission line model [105, 106]. Transfer length method (TLM) structures, fabricated at the University of Siegen and inclusive of back–gated GFETs implementing different metal contacts [81], have been measured, pointing out how the transmission line model fails to fairly describe the metal/graphene contact in a specified back–gate voltage (V_{BG}) range. A possible explanation about this failure, is the p–p^+ junction resistance induced near the contact and not considered in the model. Anyway, the extraction method has proved to be reliable for very large and negative V_{BG} values, when the junction resistance becomes negligible.
In future, the MC simulator dedicated to GFETs will be further improved, with the inclusion of a model able to fairly estimate the metal/graphene contact resistance through an in–depth investigation of the physical mechanisms correlated to the metal/graphene interface. The studied characterization technique will be fundamental for the development of such a model, that will

allow the simulation of GFETs including realistic extrinsic series resistances and the prediction of the RF device operation. The band–to–band tunneling (BBT) will also be included in the case of electrostatic doped GFETs, since it is essential to reproduce the ambipolar behavior of graphene in the output characteristics of these devices.

Vertical graphene transistors are considered as a valid alternative to the conventional and more investigated GFETs. Among the different concepts and device architectures, the Graphene–Base–Transistor (GBT [22]) is one of the most interesting for high–frequency application. Due to the early–stage technology, also for GBTs the development of physical–based models and simulators is of prime importance in the understanding of the real RF potentialities. In fact, despite the proof–of–principle of DC operation has been already demonstrated by the first fabricated GBT prototypes [30, 77], no experimental RF data are available yet.
In this thesis we have developed an electrical model for GBTs, capable of estimating both the DC and the RF operation. It has been initially used to extract guidelines for the design of the emitter material and the emitter–base–insulator (EBI). Simulations pointed out that low–k materials for EBI are better when a metal emitter is used; in contrast, EBI featuring high–k material results in higher tunneling currents combined with a silicon (Si) emitter. The structure showing the best trade–off between different RF figures of merit features a Si–emitter combined with a high–k EBI, to maximize the electron tunneling from the emitter, and a low–k base–collector insulator (BCI), in order to maintain a limited output conductance.
By extending the electrical model with the detrimental effect of space charge phenomena occurring at high current levels and affecting the maximum achievable f_T, we verified that TeraHertz (THz) operation is feasible for a wide design space. Furthermore, just like for GFETs, we have investigated on the impact of the graphene/metal contact resistance on the unity–power–gain (f_{max}) of the GBT, showing that also for this device a low access resistance is essential to obtain high f_{max}.
Moreover, we developed a single–particle Monte Carlo simulator in order to investigate the electron transport in the GBT devices. This allowed to confirm the value of the drift velocity of the carriers moving in the dielectrics of the GBT, assumed to be constant and in the order of 10^7 cm/s when accounting for the space charge effects in the electrical model.
The developed models have been used to simulate GBTs fabricated at the Royal Institute of Technology of Stockholm (KTH) [30]. The electrical model shows current values that are in a reasonable good agreement with the experimental current–voltage (IV) measurements. The MC simulator has been instead used to assess the contribution of the electron backscattering in the BCI to the formation of the base current, that is very high in experiments and largely limits the value of the common–base–current–gain (α_F). Anyway, it was not possible to well reproduce the experimental values of α_F, even accounting for the uncertainties of the material scattering parameters. This indicates that other physical mechanisms are responsible for the very large experimental base current; the major contribution is certainly the direct capture by the graphene base of forwarding moving electrons, that has been neglected in this work since the lack of a consolidated theoretical framework to describe the perpendicular transport across a graphene monolayer. Therefore, it is also important to fully understand and model the perpendicular carrier transport across the monolayer graphene, in order to investigate the possible impact of this mechanisms on the device performance and how to improve the operation of vertical graphene device concepts. Nevertheless, MC simulations pointed out that electron backscattering severely limits the α_F, suggesting that particular care must be taken in the choice of the BCI in order to keep this mechanisms limited.
Advanced GBT devices featuring bilayer dielectric stacks as EBI have been also investigated by KTH [31]. In this case, MC simulations have shown how the electron backscattering becomes the most important contribution to the base current at high base–emitter voltages. After the

calibration of the electrical model with IV measurements, we simulated optimized GBT configurations exploiting engineered tunneling barriers and based on realistic technology, giving reliable guidelines for future samples fabrication and confirming the potential of this device to reach the THz range operation.
However, the potential of the GBT remains to be demonstrated experimentally and the major effort should be spent to improve and optimize the dielectric fabrication processes. An additional option could be the exploitation of the GBHT device concept [79], for which the formation of ultra–thin dielectrics on top of graphene is not required [80].

Thanks to the huge effort made to investigate the graphene–based devices (both theoretically and experimentally), it starts to be clear that graphene cannot fully satisfy the initial expectations. For this reason, the scientific community is intensively investigating other two–dimensional (2D) materials (from metallic to insulating) beyond graphene, i.e. Transition Metal Dichalcogenide (TMD) materials, phosphorene, silicene, germanene, etc [66, 160, 161, 162]. Even though it is still complicated to understand the real potential of these novel materials in nanoelectronics, it is clear that they have very promising perspective in several industrial fields. The fundamental role of this thesis is to have built–up a set of simulation tools that must be necessary extended to other 2D materials. Indeed, graphene has opened literally a new world being the pioneer of 2D materials. The research on 2D materials has just started!

"*Graphene is dead, long live graphene*", Andre Geim.

Bibliography

[1] G. E. Moore, "Progress in Digital Integrated Electronics," *IEEE International Electron Devices Meeting (IEDM), Technical Digest*, pp. 11–13, 1975.

[2] Y. Taur and T. H. Ning, "Fundamentals of Modern VLSI Devices," *Cambridge University Press*, 2013.

[3] D. Esseni, P. Palestri, and L. Selmi, "Nanoscale MOS Transistors: Semi–Classical Transport and Applications," *Cambridge University Press*, 2011.

[4] J. Welser, J. L. Hoyt, and J. F. Gibbons, "Electron Mobility Enhancement in Strained–Si n–type Metal–Oxide–Semiconductor Field–Effect Transistors," *IEEE Electron Device Letters*, vol. 15, no. 3, pp. 100–102, 1994.

[5] Y. Kamata, "High–k/Ge MOSFETs for Future Nanoelectronics," *Materials Today*, vol. 11, no. 1-2, pp. 30–38, 2008.

[6] K. S. Novoselov, A. K. Geim, S. V. Morozov, D. Jiang, Y. Zhang, S. V. Dubonos, I. V. Grigorieva, and A. A. Firsov, "Electric Field Effect in Atomically Thin Carbon Films," *Science*, vol. 306, no. 5696, pp. 666–669, 2004.

[7] C. Berger, Z. Song, T. Li, X. Li, A. Y. Ogbazghi, R. Feng, Z. Dai, A. N. Marchenkov, E. H. Conrad, P. N. First, and W. A. de Heer, "Ultrathin Epitaxial Graphite: 2D Electron Gas Properties and a Route Toward Graphene–Based Nanoelectronics," *The Journal of Physical Chemistry B*, vol. 108, no. 52, pp. 19912–19916, 2004.

[8] A. K. Geim and K. S. Novoselov, "The Rise of Graphene," *Nature Materials*, vol. 6, pp. 183–191, 2007.

[9] A. K. Geim, "Graphene: Status and Prospects," *Science*, vol. 324, no. 5934, pp. 1530–1534, 2009.

[10] A. Geim, "Graphene Update," *Bulletin of the American Physical Society*, vol. 55, 2010.

[11] R. Cheng, J. Bai, L. Liao, H. Zhou, Y. Chen, L. Liu, Y.-C. Lin, S. Jiang, Y. Huang, and X. Duan, "High–Frequency Self–Aligned Graphene Transistors with Transferred Gate Stacks," *Proceedings of the National Academy of Sciences*, vol. 109, no. 29, pp. 11588–11592, 2012.

[12] F. Schwierz, "Graphene Transistors: Status, Prospects, and Problems," *Proceedings of the IEEE*, vol. 101, no. 7, pp. 1567–1584, 2013.

[13] A. C. Ferrari et al., "Science and Technology Roadmap for Graphene, Related Two–Dimensional Crystals, and Hybrid Systems," *Nanoscale*, vol. 7, pp. 4598–4810, 2015.

[14] F. Xia, V. Perebeinos, Y.-M. Lin, Y. Wu, and P. Avouris, "The Origins and Limits of Metal–Graphene Junction Resistance," *Nature Nanotechnology*, vol. 6, pp. 179–184, 2011.

[15] A. Gahoi, V. Passi, S. Kataria, S. Wagner, A. Bablich, and M. C. Lemme, "Systematic Comparison of Metal Contacts on CVD Graphene," *Proceedings of the European Solid–State Device Research Conference (ESSDERC)*, pp. 184–187, 2015.

[16] V. Passi, A. Gahoi, J. Ruhkopf, S. Kataria, F. Vaurette, E. Pallecchi, H. Happy, and M. C. Lemme, "Contact Resistance Study of "Edge–Contacted" Metal–Graphene Interfaces," *Proceedings of the European Solid-State Device Research Conference (ESSDERC)*, pp. 236–239, 2016.

[17] M. Bresciani, P. Palestri, D. Esseni, and L. Selmi, "Simple and Efficient Modeling of the E-k Relationship and Low–Field Mobility in Graphene Nano–Ribbons," *Solid–State Electronics*, vol. 54, no. 9, pp. 1015–1021, 2010.

[18] M. Bresciani, A. Paussa, P. Palestri, D. Esseni, and L. Selmi, "Low–Field Mobility and High–Field Drift Velocity in Graphene Nanoribbons and Graphene Bilayers," *IEEE International Electron Devices Meeting (IEDM), Technical Digest*, pp. 32.1.1–32.1.4, 2010.

[19] M. Poljak, K. L. Wang, and T. Suligoj, "Variability of Bandgap and Carrier Mobility Caused by Edge Defects in Ultra–Narrow Graphene Nanoribbons," *Solid–State Electronics*, vol. 108, pp. 67–74, 2015.

[20] G. Fiori, D. Neumaier, B. N. Szafranek, and G. Iannaccone, "Bilayer Graphene Transistors for Analog Electronics," *IEEE Transactions on Electron Devices*, vol. 61, no. 3, pp. 729–733, 2014.

[21] H. Pandey, S. Kataria, V. Passi, M. Iannazzo, E. Alarcon, and M. C. Lemme, "Improved Voltage Gain in Mechanically Stacked Bilayer Graphene Field Effect Transistors," *Joint International EUROSOI Workshop and International Conference on Ultimate Integration on Silicon (EUROSOI-ULIS)*, pp. 143–146, 2016.

[22] W. Mehr, J. Dabrowski, J. Christoph Scheytt, G. Lippert, Y.-H. Xie, M. C. Lemme, M. Östling, and G. Lupina, "Vertical Graphene Base Transistor'," *IEEE Electron Device Letters*, vol. 33, no. 5, pp. 691–693, 2012.

[23] F. Driussi, P. Palestri, and L. Selmi, "Modeling, Simulation and Design of the Vertical Graphene Base Transistor," *Microelectronic Engineering*, vol. 109, pp. 338–341, 2013.

[24] V. Di Lecce, R. Grassi, A. Gnudi, E. Gnani, S. Reggiani, and G. Baccarani, "Graphene Base Transistors: A Simulation Study of DC and Small–Signal Operation'," *IEEE Transactions on Electron Devices*, vol. 60, no. 10, pp. 3584–3591, 2013.

[25] V. D. Lecce, R. Grassi, A. Gnudi, E. Gnani, S. Reggiani, and G. Baccarani, "DC and Small–Signal Numerical Simulation of Graphene–Base–Transistor for Terahertz Operation," *Proceedings of the European Solid State Device Research Conference (ESSDERC)*, p. 314, 2013.

[26] S. Venica, F. Driussi, P. Palestri, D. Esseni, S. Vaziri, and L. Selmi, "Simulation of DC and RF Performance of the Graphene Base Transistor," *IEEE Transactions on Electron Devices*, vol. 61, no. 7, pp. 2570–2576, 2014.

[27] G. Iannaccone, G. Fiori, M. Macucci, P. Michetti, M. Cheli, A. Betti, and P. Marconcini, "Perspectives of Graphene Nanoelectronics: Probing Technological Options with Modeling," *IEEE International Electron Devices Meeting (IEDM), Technical Digest*, pp. 1–4, 2009.

[28] G. Fiori and G. Iannaccone, "Multiscale Modeling for Graphene–Based Nanoscale Transistors," *Proceedings of the IEEE*, vol. 101, no. 7, pp. 1653–1669, 2013.

[29] A. Paussa, G. Fiori, P. Palestri, M. Geromel, D. Esseni, G. Iannaccone, and L. Selmi, "Simulation of the Performance of Graphene FETs with a Semiclassical Model, Including Band–to–Band Tunneling," *IEEE Transactions on Electron Devices*, vol. 61, no. 5, pp. 1567–1574, 2014.

[30] S. Vaziri, G. Lupina, C. Henkel, A. D. Smith, M. Östling, J. Dabrowski, G. Lippert, W. Mehr, and M. C. Lemme, "A Graphene–Based Hot Electron Transistor'," *Nano Letters*, vol. 13, no. 4, pp. 1435–1439, 2013.

[31] S. Vaziri, M. Belete, E. Dentoni Litta, A. D. Smith, G. Lupina, M. C. Lemme, and M. Ostling, "Bilayer Insulator Tunnel Barriers for Graphene–Based Vertical Hot–Electron Transistors," *Nanoscale*, vol. 7, pp. 13096–13104, 2015.

[32] C. Kittel, "Quantum theory of solids," *John Wiley & Sons Inc.*, 1987.

[33] A. Paussa, "Numerical Simulation of Advanced CMOS and Beyond CMOS Nanoscale Transistor," *PhD Thesis*, 2013.

[34] H.-S. P. Wong and D. Akinwande, "Carbon Nanotube and Graphene Device Physics," *Cambrige University Press*, 2011.

[35] I. Gierz, C. Riedl, U. Starke, C. R. Ast, and K. Kern, "Atomic Hole Doping of Graphene," *Nano Letters*, vol. 8, no. 12, pp. 4603–4607, 2008.

[36] A. H. Castro Neto, F. Guinea, N. M. R. Peres, K. S. Novoselov, and A. K. Geim, "The Electronic Properties of Graphene," *Reviews of Modern Physics*, vol. 81, pp. 109–162, 2009.

[37] T. Fang, A. Konar, H. Xing, and D. Jena, "Carrier Statistics and Quantum Capacitance of Graphene Sheets and Ribbons," *Applied Physics Letters*, vol. 91, no. 9, p. 092109, 2007.

[38] J. S. Moon and D. K. Gaskill, "Graphene: Its Fundamentals to Future Applications," *IEEE Transactions on Microwave Theory and Techniques*, vol. 59, no. 10, pp. 2702–2708, 2011.

[39] V. E. Dorgan, M.-H. Bae, and E. Pop, "Mobility and Saturation Velocity in Graphene on SiO_2," *Applied Physics Letters*, vol. 97, no. 8, p. 082112, 2010.

[40] M. Poljak, T. Suligoj, and K. L. Wang, "Influence of Substrate Type and Quality on Carrier Mobility in Graphene Nanoribbons," *Journal of Applied Physics*, vol. 114, no. 5, p. 053701, 2013.

[41] S. Kataria, S. Wagner, J. Ruhkopf, A. Gahoi, H. Pandey, R. Bornemann, S. Vaziri, A. D. Smith, M. Ostling, and M. C. Lemme, "Chemical Vapor Deposited Graphene: From Synthesis to Applications," *Physica Status Solidi A*, vol. 211, no. 11, 2014.

[42] Y. Wang, B. C. Huang, M. Zhang, C. Miao, Y. H. Xie, and J. C. S. Woo, "High Performance Graphene FETs with Self–Aligned Buried Gates Fabricated on Scalable Patterned Ni–Catalyzed Graphene," *Symposium on VLSI Technology - Digest of Technical Papers*, pp. 116–117, 2011.

[43] A. Akturk and N. Goldsman, "Electron Transport and Full–Band Electron–Phonon Interactions in Graphene," *Journal of Applied Physics*, vol. 103, no. 5, p. 053702, 2008.

[44] R. R. Nair, P. Blake, A. N. Grigorenko, K. S. Novoselov, T. J. Booth, T. Stauber, N. M. R. Peres, and A. K. Geim, "Fine Structure Constant Defines Visual Transparency of Graphene," *Science*, vol. 320, no. 5881, pp. 1308–1308, 2008.

[45] G. Anagnostopoulos, P.-N. Pappas, Z. Li, I. A. Kinloch, R. J. Young, K. S. Novoselov, C. Y. Lu, N. Pugno, J. Parthenios, C. Galiotis, and K. Papagelis, "Mechanical Stability of Flexible Graphene–Based Displays," *ACS Applied Materials & Interfaces*, vol. 8, no. 34, pp. 22605–22614, 2016.

[46] F. Withers, O. Del Pozo-Zamudio, A. Mishchenko, A. P. Rooney, A. Gholinia, K. Watanabe, T. Taniguchi, S. J. Haigh, A. K. Geim, A. I. Tartakovskii, and K. S. Novoselov, "Light–Emitting Diodes by Band–Structure Engineering in van der Waals Heterostructures," *Nature Materials*, vol. 14, pp. 301–306, 2015.

[47] D. S. Schneider, A. Bablich, and M. C. Lemme, "Graphene/a–Si:H Multispectral Photodetectors," *Proceedings of the European Solid State Device Research Conference (ESSDERC)*, pp. 287–290, 2016.

[48] A. Bablich, S. Kataria, and M. C. Lemme, "Graphene and Two–Dimensional Materials for Optoelectronic Applications," *Electronics*, vol. 5, no. 1, p. 13, 2016.

[49] H. Tomori, A. Kanda, H. Goto, Y. Ootuka, K. Tsukagoshi, S. Moriyama, E. Watanabe, and D. Tsuya, "Introducing Nonuniform Strain to Graphene Using Dielectric Nanopillars," *Applied Physics Express*, vol. 4, no. 7, p. 075102, 2011.

[50] S. Wagner, C. Weisenstein, A. Smith, M. Östling, S. Kataria, and M. C. Lemme, "Graphene Transfer Methods for the Fabrication of Membrane–Based NEMS Devices," *Microelectronic Engineering*, vol. 159, pp. 108–113, 2016.

[51] N. Petrone, I. Meric, T. Chari, K. L. Shepard, and J. Hone, "Graphene Field–Effect Transistors for Radio–Frequency Flexible Electronics," *IEEE Journal of the Electron Devices Society*, vol. 3, no. 1, pp. 44–48, 2015.

[52] A. A. Balandin, S. Ghosh, W. Bao, I. Calizo, D. Teweldebrhan, F. Miao, and C. N. Lau, "Superior Thermal Conductivity of Single–Layer Graphene," *Nano Letters*, vol. 8, no. 3, pp. 902–907, 2008.

[53] M. C. Lemme, L.-J. Li, T. Palacios, and F. Schwierz, "Two–Dimensional Materials for Electronic Applications," *MRS Bulletin*, vol. 39, no. 8, pp. 711–718, 2014.

[54] P. C. Feijoo, D. Jiménez, and X. Cartoixà, "Short Channel Effects in Graphene–Based Field Effect Transistors Targeting Radio–Frequency Applications," *2D Materials*, vol. 3, no. 2, p. 025036, 2016.

[55] M. C. Lemme, T. J. Echtermeyer, M. Baus, and H. Kurz, "A Graphene Field–Effect Device," *IEEE Electron Device Letters*, vol. 28, no. 4, pp. 282–284, 2007.

[56] I. Meric, N. Baklitskaya, P. Kim, and K. L. Shepard, "RF Performance of Top–Gated, Zero–Bandgap Graphene Field–Effect Transistors," *International Electron Devices Meeting (IEDM), Technical Digest*, pp. 1–4, 2008.

[57] J. S. Moon, D. Curtis, M. Hu, D. Wong, C. McGuire, P. M. Campbell, G. Jernigan, J. L. Tedesco, B. VanMil, R. Myers-Ward, C. Eddy, and D. K. Gaskill, "Epitaxial–Graphene RF Field–Effect Transistors on Si-Face 6H-SiC Substrates," *IEEE Electron Device Letters*, vol. 30, no. 6, pp. 650–652, 2009.

[58] Y. M. Lin, H. Y. Chiu, K. A. Jenkins, D. B. Farmer, P. Avouris, and A. Valdes-Garcia, "Dual–Gate Graphene FETs with f_t of 50 GHz," *IEEE Electron Device Letters*, vol. 31, no. 1, pp. 68–70, 2010.

[59] L. Liao, Y.-C. Lin, M. Bao, R. Cheng, J. Bai, Y. Liu, Y. Qu, K. L. Wang, Y. Huang, and X. Duan, "High–Speed Graphene Transistors with a Self–Aligned Nanowire Gate," *Nature*, vol. 467, pp. 305–308, 2010.

[60] J. Y. Tan, A. Avsar, J. Balakrishnan, G. K. W. Koon, T. Taychatanapat, E. C. T. O'Farrell, K. Watanabe, T. Taniguchi, G. Eda, A. H. C. Neto, and B. Özyilmaz, "Electronic Transport in Graphene–Based Heterostructures," *Applied Physics Letters*, vol. 104, no. 18, p. 183504, 2014.

[61] S. Vaziri, A. Smith, M. stling, G. Lupina, J. Dabrowski, G. Lippert, W. Mehr, F. Driussi, S. Venica, V. D. Lecce, A. Gnudi, M. Knig, G. Ruhl, M. Belete, and M. Lemme, "Going Ballistic: Graphene Hot Electron Transistors," *Solid State Communications*, vol. 224, pp. 64–75, 2015.

[62] Y. M. Lin, K. Jenkins, D. Farmer, A. Valdes-Garcia, P. Avouris, C. Y. Sung, H. Y. Chiu, and B. Ek, "Development of Graphene FETs for High Frequency Electronics," *International Electron Devices Meeting (IEDM), Technical Digest*, pp. 1–4, 2009.

[63] Y. M. Lin, D. B. Farmer, K. A. Jenkins, Y. Wu, J. L. Tedesco, R. L. Myers-Ward, C. R. Myers-Ward, D. K. Gaskill, C. Dimitrakopoulos, and P. Avouris, "Enhanced Performance in Epitaxial Graphene FETs with Optimized Channel Morphology," *IEEE Electron Device Letters*, vol. 32, no. 10, pp. 1343–1345, 2011.

[64] J. Lee, H.-J. Chung, J. Lee, H. Shin, J. Heo, H. Yang, S.-H. Lee, S. Seo, J. Shin, U. in Chung, I. Yoo, and K. Kim, "RF Performance of Pre–Patterned Locally–Embedded–Back–Gate Graphene Device," *International Electron Devices Meeting (IEDM), Technical Digest*, pp. 23.5.1–23.5.4, 2010.

[65] S. Sarkozy, M. Vukovic, J. G. Padilla, J. Chang, G. Tseng, P. Tran, P. Yocom, W. Yamasaki, K. M. K. H. Leong, and W. Lee, "Demonstration of a G–Band Transceiver for Future Space Crosslinks," *IEEE Transactions on Terahertz Science and Technology*, vol. 3, no. 5, pp. 675–681, 2013.

[66] M. Houssa, A. Dimoulas, and A. Molle, "2D Materials for Nanoelectronics," *CRC Press*, 2016.

[67] Z. H. Feng, C. Yu, J. Li, Q. B. Liu, Z. Z. He, X. B. Song, J. J. Wang, and S. J. Cai, "An Ultra Clean Self–Aligned Process for High Maximum Oscillation Frequency Graphene Transistors," *Carbon*, vol. 75, pp. 249–254, 2014.

[68] M. Poljak and T. Suligoj, "Quantum Transport Analysis of Conductance Variability in Graphene Nanoribbons with Edge Defects," *IEEE Transactions on Electron Devices*, vol. 63, no. 2, pp. 537–543, 2016.

[69] G. Fiori and G. Iannaccone, "Simulation of Graphene Nanoribbon Field–Effect Transistors," *IEEE Electron Device Letters*, vol. 28, no. 8, pp. 760–762, 2007.

[70] C. Si, Z. Sun, and F. Liu, "Strain Engineering of Graphene: a Review," *Nanoscale*, vol. 8, pp. 3207–3217, 2016.

[71] H. Yang, J. Heo, S. Park, H. J. Song, D. H. Seo, K.-E. Byun, P. Kim, I. Yoo, H.-J. Chung, and K. Kim, "Graphene Barristor, a Triode Device with a Gate–Controlled Schottky Barrier," *Science*, vol. 336, no. 6085, pp. 1140–1143, 2012.

[72] L. Britnell, R. V. Gorbachev, R. Jalil, B. D. Belle, F. Schedin, M. I. Katsnelson, L. Eaves, S. V. Morozov, A. S. Mayorov, N. M. R. Peres, A. H. Castro Neto, J. Leist, A. K. Geim, L. A. Ponomarenko, and K. S. Novoselov, "Electron Tunneling through Ultrathin Boron Nitride Crystalline Barriers," *Nano Letters*, vol. 12, no. 3, pp. 1707–1710, 2012.

[73] L. Britnell, R. V. Gorbachev, R. Jalil, B. D. Belle, F. Schedin, A. Mishchenko, T. Georgiou, M. I. Katsnelson, L. Eaves, S. V. Morozov, N. M. R. Peres, J. Leist, A. K. Geim, K. S. Novoselov, and L. A. Ponomarenko, "Field–Effect Tunneling Transistor Based on Vertical Graphene Heterostructures," vol. 335, no. 6071, pp. 947–950, 2012.

[74] S. B. Kumar, G. Seol, and J. Guo, "Modeling of a Vertical Tunneling Graphene Heterojunction Field–Effect Transistor," *Applied Physics Letters*, vol. 101, no. 3, p. 033503, 2012.

[75] M. Heiblum, "Tunneling Hot Electron Transfer Amplifiers (theta): Amplifiers Operating up to the Infrared," *Solid–State Electronics*, vol. 24, no. 4, pp. 343–366, 1981.

[76] M. Heiblum and M. V. Fischetti, "Ballistic Hot–Electron Transistors," *IBM Journal of Research and Development*, vol. 34, no. 4, pp. 530–549, 1990.

[77] C. Zeng, E. B. Song, M. Wang, S. Lee, C. M. Torres, J. Tang, B. H. Weiller, and K. L. Wang, "Vertical Graphene–Base Hot–Electron Transistor," *Nano Letters*, vol. 13, no. 6, pp. 2370–2375, 2013.

[78] S. Venica, F. Driussi, P. Palestri, and L. Selmi, "Graphene Base Transistors with Optimized Emitter and Dielectrics," *International Convention on Information and Communication Technology, Electronics and Microelectronics (MIPRO)*, pp. 33–38, 2014.

[79] V. D. Lecce, R. Grassi, A. Gnudi, E. Gnani, S. Reggiani, and G. Baccarani, "Graphene–Base Heterojunction Transistor: An Attractive Device for Terahertz Operation," *IEEE Transactions on Electron Devices*, vol. 60, no. 12, 2013.

[80] V. D. Lecce, A. Gnudi, E. Gnani, S. Reggiani, and G. Baccarani, "Graphene–Base Heterojunction Transistors for Post–CMOS High–Speed Applications: Hopes and Challenges," *Annual Device Research Conference (DRC)*, pp. 91–92, 2015.

[81] A. Gahoi, S. Wagner, A. Bablich, S. Kataria, V. Passi, and M. C. Lemme, "Contact Resistance Study of Various Metal Electrodes with CVD Graphene," *Solid–State Electronics*, vol. 125, pp. 234–239, 2016.

[82] S. M. Koh, E. Y. J. Kong, B. Liu, C. M. Ng, G. S. Samudra, and Y. C. Yeo, "Contact–Resistance Reduction for Strained n–FinFETs with Silicon–Carbon Source/Drain and Platinum–Based Silicide Contacts Featuring Tellurium Implantation and Segregation," *IEEE Transactions on Electron Devices*, vol. 58, no. 11, pp. 3852–3862, 2011.

[83] A. R. Alt and C. R. Bolognesi, "Temperature Dependence of Annealed and Nonannealed HEMT Ohmic Contacts Between 5 and 350 K," *IEEE Transactions on Electron Devices*, vol. 60, no. 2, pp. 787–792, 2013.

[84] H. Zhong, Z. Zhang, B. Chen, H. Xu, D. Yu, L. Huang, and L. Peng, "Realization of Low Contact Resistance Close to Theoretical Limit in Graphene Transistors," *Nano Research*, vol. 8, no. 5, pp. 1669–1679, 2015.

[85] A. Meersha, H. B. Variar, K. Bhardwaj, A. Mishra, S. Raghavan, N. Bhat, and M. Shrivastava, "Record Low Metal–(CVD) Graphene Contact Resistance Using Atomic Orbital Overlap Engineering," *International Electron Devices Meeting (IEDM), Technical Digest*, pp. 5.3.1–5.3.4, 2016.

[86] W. S. Leong, H. Gong, and J. T. L. Thong, "Low–Contact–Resistance Graphene Devices with Nickel–Etched–Graphene Contacts," *ACS Nano*, vol. 8, no. 1, pp. 994–1001, 2014.

[87] J. S. Moon, M. Antcliffe, H. C. Seo, D. Curtis, S. Lin, A. Schmitz, I. Milosavljevic, A. A. Kiselev, R. S. Ross, D. K. Gaskill, P. M. Campbell, R. C. Fitch, K.-M. Lee, and P. Asbeck, "Ultra–Low Resistance Ohmic Contacts in Graphene Field Effect Transistors," *Applied Physics Letters*, vol. 100, no. 20, p. 203512, 2012.

[88] S. Babiker, A. Asenov, N. Cameron, and S. P. Beaumont, "Simple Approach to Include External Resistances in the Monte Carlo Simulation of MESFETs and HEMTs," *IEEE Transactions on Electron Devices*, vol. 43, no. 11, pp. 2032–2034, 1996.

[89] A. Paussa, M. Geromel, P. Palestri, M. Bresciani, D. Esseni, and L. Selmi, "Simulation of Graphene Nanoscale RF Transistors Including Scattering and Generation/Recombination Mechanisms," *International Electron Devices Meeting (IEDM), Technical Digest*, pp. 11.7.1–11.7.4, 2011.

[90] D. Finkenstadt, G. Pennington, and M. J. Mehl, "From Graphene to Graphite: A General Tight–Binding Approach for Nanoribbon Carrier Transport," *Physical Review B*, vol. 76, p. 121405, 2007.

[91] G. Pennington and N. Goldsman, "Low–Field Semiclassical Carrier Transport in Semiconducting Carbon Nanotubes," *Phyical Review B*, vol. 71, p. 205318, 2005.

[92] R. S. Shishir, F. Chen, J. Xia, N. J. Tao, and D. K. Ferry, "Room Temperature Carrier Transport in Graphene," *Journal of Computational Electronics*, vol. 8, no. 2, pp. 43–50, 2009.

[93] F. Rana, P. A. George, J. H. Strait, J. Dawlaty, S. Shivaraman, M. Chandrashekhar, and M. G. Spencer, "Carrier Recombination and Generation Rates for Intravalley and Intervalley Phonon Scattering in Graphene," *Physical Review B*, vol. 79, p. 115447, 2009.

[94] H. Liu, Y. Liu, and D. Zhu, "Chemical Doping of Graphene," *Journal of Materials Chemistry*, vol. 21, pp. 3335–3345, 2011.

[95] A. Narita, X.-Y. Wang, X. Feng, and K. Mullen, "New Advances in Nanographene Chemistry," *Chemical Society Review*, vol. 44, pp. 6616–6643, 2015.

[96] T. Cusati, G. Fiori, A. Gahoi, V. Passi, A. Fortunelli, M. Lemme, and G. Iannaccone, "Understanding the Nature of Metal–Graphene Contacts: A Theoretical and Experimental Study," *IEEE International Electron Devices Meeting (IEDM), Technical Digest*, pp. 12.7.1–12.7.4, 2015.

[97] J. Knoch, Z. Chen, and J. Appenzeller, "Properties of Metal–Graphene Contacts," *IEEE Transactions on Nanotechnology*, vol. 11, no. 3, pp. 513–519, 2012.

[98] D. Berdebes, T. Low, Y. Sui, J. Appenzeller, and M. S. Lundstrom, "Substrate Gating of Contact Resistance in Graphene Transistors," *IEEE Transactions on Electron Devices*, vol. 58, no. 11, pp. 3925–3932, 2011.

[99] G. Giovannetti, P. A. Khomyakov, G. Brocks, V. M. Karpan, J. van den Brink, and P. J. Kelly, "Doping Graphene with Metal Contacts," *Physical Review Letters*, vol. 101, p. 026803, 2008.

[100] K. Nagashio, T. Nishimura, K. Kita, and A. Toriumi, "Contact Resistivity and Current Flow Path at Metal/Graphene Contact," *Applied Physics Letters*, vol. 97, no. 14, p. 143514, 2010.

[101] F. A. Chaves, D. Jiménez, A. A. Sagade, W. Kim, J. Riikonen, H. Lipsanen, and D. Neumaier, "A Physics–Based Model of Gate–Tunable Metal-Graphene Contact Resistance Benchmarked Against Eexperimental Data," *2D Materials*, vol. 2, no. 2, p. 025006, 2015.

[102] R. M. Feenstra, D. Jena, and G. Gu, "Single–Particle Tunneling in Doped Graphene–Insulator–Graphene Junctions," *Journal of Applied Physics*, vol. 111, no. 4, p. 043711, 2012.

[103] G. K. Reeves and H. B. Harrison, "Obtaining the Specific Contact Resistance from Transmission Line Model Measurements," *IEEE Electron Device Letters*, vol. 3, no. 5, pp. 111–113, 1982.

[104] M. Hajlasz, J. J. T. M. Donkers, S. J. Sque, S. B. S. Heil, D. J. Gravesteijn, F. J. R. Rietveld, and J. Schmitz, "Sheet Resistance Under Ohmic Contacts to AlGaN/GaN Heterostructures," *Applied Physics Letters*, vol. 104, no. 24, p. 242109, 2014.

[105] S. Wang, D. Mao, Z. Jin, S. Peng, D. Zhang, J. Shi, and X. Wang, "A More Reliable Measurement Method for Metal/Graphene Contact Resistance," *Nanotechnology*, vol. 26, no. 40, p. 405706, 2015.

[106] S. Wang, D. Mao, A. Muhammad, S. Peng, D. Zhang, J. Shi, and Z. Jin, "Characterization of the Quality of Metal–Graphene Contact with Contact End Resistance Measurement," *Applied Physics A*, vol. 122, no. 7, p. 643, 2016.

[107] H. H. Berger, "Models for Contacts to Planar Devices," *Solid–State Electronics*, vol. 15, no. 2, pp. 145–158, 1972.

[108] D. K. Schroder, "Semiconductor Material and Device Characterization," *Wiley–IEEE Press*, 2015.

[109] H. B. Michaelson, "The Work Function of the Elements and its Periodicity," *Journal of Applied Physics*, vol. 48, no. 11, pp. 4729–4733, 1977.

[110] T. Mueller, F. Xia, M. Freitag, J. Tsang, and P. Avouris, "Role of Contacts in Graphene Transistors: a Scanning Photocurrent Study," *Physical Review B*, vol. 79, p. 245430, 2009.

[111] A. D. Smith, K. Elgammal, F. Niklaus, A. Delin, A. C. Fischer, S. Vaziri, F. Forsberg, M. Rå sander, H. Hugosson, L. Bergqvist, S. Schröder, S. Kataria, M. Östling, and M. C. Lemme, "Resistive Graphene Humidity Sensors with Rapid and Direct Electrical Readout," *Nanoscale*, vol. 7, pp. 19099–19109, 2015.

[112] A. Piazza, F. Giannazzo, G. Buscarino, G. Fisichella, A. L. Magna, F. Roccaforte, M. Cannas, F. M. Gelardi, and S. Agnello, "Effect of Air on Oxygen p–Doped Graphene on SiO_2," *Physica Status Solidi A*, vol. 213, pp. 2341–2344, 2016.

[113] V. D. Lecce, A. Gnudi, E. Gnani, S. Reggiani, and G. Baccarani, "Simulation of Graphene Base Transistors with Bilayer Tunnel Oxide Barrier: Model Calibration and Performance Projection," *IEEE Electron Device Letters*, vol. 37, no. 11, pp. 1489–1492, 2016.

[114] S. Frégonèse, S. Venica, F. Driussi, and T. Zimmer, "Electrical Compact Modeling of Graphene Base Transistors," *Electronics*, vol. 4, no. 4, p. 969, 2015.

[115] Q. Zhang, G. Fiori, and G. Iannaccone, "On Transport in Vertical Graphene Heterostructures," *IEEE Electron Device Letters*, vol. 35, no. 9, pp. 966–968, 2014.

[116] S. Bruzzone, D. Logoteta, G. Fiori, and G. Iannaccone, "Vertical Transport in Graphene–Hexagonal Boron Nitride Heterostructure Devices," *Scientific Reports*, vol. 5, p. 14519, 2015.

[117] J. S. Blakemore, "Approximations for Fermi–Dirac Integrals, Especially the Function $\mathcal{F}_{1/2}(\eta)$ Used to Describe Electron Density in a Semiconductor," *Solid–State Electronics*, vol. 25, no. 11, pp. 1067–1076, 1982.

[118] E. H. Nicollian and J. R. Brews, "MOS (Metal Oxide Semiconductor) Physics and Technology," *Wiley Classics Library*, 2002.

[119] S. Takagi, N. Yasuda, and A. Toriumi, "A New I–V Model for Stress–Induced Leakage Current Including Inelastic Tunneling," *IEEE Transactions on Electron Devices*, vol. 46, no. 2, pp. 348–354, 1999.

[120] J. Suñé, P. Olivo, and B. Riccó, "Quantum–Mechanical Modeling of Accumulation Layers in MOS Structure," *IEEE Transactions on Electron Devices*, vol. 39, no. 7, pp. 1732–1739, 1992.

[121] R. G. Meyer and R. S. Muller, "Charge–Control Analysis of the Collector–Base Space–Charge–Region Contribution to Bipolar–Transistor Time Constant τ_t," *IEEE Transactions on Electron Devices*, vol. 34, no. 2, pp. 450–452, 1987.

[122] S. M. Sze and K. N. Kwok, "Physics of Semiconductor Devices," *Wiley–Interscience*, 2006.

[123] P. Palestri, L. Selmi, E. Sangiorgi, M. Pavesi, and F. Widdershoven, "Cathode Hot Electrons and Anode Hot Holes in Tunneling MOS Capacitors," *Proceedings of the European Solid State Device Research Conference (ESSDERC)*, pp. 296–299, 2000.

[124] B. Heinemann, R. Barth, D. Bolze, J. Drews, G. G. Fischer, A. Fox, O. Fursenko, T. Grabolla, U. Haak, D. Knoll, R. Kurps, M. Lisker, S. Marschmeyer, H. Rcker, D. Schmidt, J. Schmidt, M. A. Schubert, B. Tillack, C. Wipf, D. Wolansky, and Y. Yamamoto, "SiGe HBT Technology with f_t/f_{max} of 300 GHz/500 GHz and 2.0 ps CML Gate Delay," *International Electron Devices Meeting (IEDM), Technical Digest*, pp. 30.5.1–30.5.4, 2010.

[125] B. Geynet, P. Chevalier, B. Vandelle, F. Brossard, N. Zerounian, M. Buczko, D. Gloria, F. Aniel, G. Dambrine, F. Danneville, D. Dutartre, and A. Chantre, "SiGe HBTs featuring $f_t \gg 400$ GHz at Room Temperature," *IEEE Bipolar/BiCMOS Circuits and Technology Meeting*, pp. 121–124, 2008.

[126] S. Lombardo, J. H. Stathis, B. P. Linder, K. L. Pey, F. Palumbo, and C. H. Tung, "Dielectric Breakdown Mechanisms in Gate Oxides," *Journal of Applied Physics*, vol. 98, no. 12, p. 121301, 2005.

[127] J. Lee, L. Tao, Y. Hao, R. S. Ruoff, and D. Akinwande, "Embedded–Gate Graphene Transistors for High–Mobility Detachable Flexible Nanoelectronics," *Applied Physics Letters*, vol. 100, no. 15, p. 152104, 2012.

[128] A. Hsu, H. Wang, K. K. Kim, J. Kong, and T. Palacios, "Impact of Graphene Interface Quality on Contact Resistance and RF Device Performance," *IEEE Electron Device Letters*, vol. 32, no. 8, pp. 1008–1010, 2011.

[129] M. V. Fischetti, D. J. DiMaria, S. D. Brorson, T. N. Theis, and J. R. Kirtley, "Theory of High–Field Electron Transport in Silicon Dioxide," *Physical Review B*, vol. 31, pp. 8124–8142, 1985.

[130] P. Palestri, L. Selmi, M. Pavesi, F. Widdershoven, and E. Sangiorgi, "Coupled Monte Carlo Simulation of Si and SiO_2 Transport in MOS Capacitors," *Proceedings of SISPAD*, pp. 38–41, 2000.

[131] S. Spiga, F. Driussi, A. Lamperti, G. Congedo, and O. Salicio, "Effects of Thermal Treatments on the Trapping Properties of HfO_2 Films for Charge Trap Memories," *Applied Physics Express*, vol. 5, no. 2, p. 021102, 2012.

[132] M. V. Fischetti, D. A. Neumayer, and E. A. Cartier, "Effective Electron Mobility in Si Inversion Layers in Metal–Oxide–Semiconductor Systems with a High–k Insulator: The Role of Remote Phonon Scattering," *Journal of Applied Physics*, vol. 90, no. 9, pp. 4587–4608, 2001.

[133] J. Shan, F. Wang, E. Knoesel, M. Bonn, and T. F. Heinz, "Measurement of the Frequency–Dependent Conductivity in Sapphire," *Physical Review Letters*, vol. 90, p. 247401, 2003.

[134] P. Palestri, E. Caruso, F. Driussi, D. Esseni, D. Lizzit, P. Osgnach, S. Venica, and L. Selmi, "State–of–the–Art Semi–Classical Monte Carlo Method for Carrier Transport in Nanoscale Transistors," *International Convention on Information and Communication Technology, Electronics and Microelectronics (MIPRO)*, pp. 1–8, 2015.

[135] A. Shanware, H. Z. Massoud, E. Vogel, K. Henson, J. R. Hauser, and J. . Wortman, "Modeling the Trends in Valence–Band Eectron Tunneling in NMOSFETs with Ultrathin SiO_2 and SiO_2/Ta_2O_5 Dielectrics with Oxide Scaling," *Microelectronic Engineering*, vol. 48, no. 1, pp. 295–298, 1999.

[136] B. C. Lai, N. Kung, and J. Y. Lee, "A Study on the Capacitance-Voltage Characteristics of Metal–Ta_2O_5–Silicon Capacitors for Very Large Scale Integration Metal–Oxide–Semiconductor Gate Oxide Applications," *Journal of Applied Physics*, vol. 85, no. 8, pp. 4087–4090, 1999.

[137] T. Devoivre, F. Martin, C. Papadas, and M. Setton, "Silicon Nitridation by Nitric Oxide (NO) for Ta_2O_5 Gate Dielectric Application in MOS Devices," *European Solid–State Device Research Conference*, vol. 1, pp. 420–423, 1999.

[138] C. Guedj, E. Martinez, C. Licitra, G. Imbert, J. P. Barnes, D. Lafond, A. Toffoli, V. Arnal, and L. Anaud, "Bulk and Interface Band Diagrams of Advanced Intermetal Dielectrics," *International Electron Devices Meeting (IEDM), Technical Digest*, pp. 977–980, 2007.

[139] J. Robertson, "Band Offsets of Wide–Band–Gap Oxides and Implications for Future Electronic Devices," *Journal of Vacuum Science & Technology B: Microelectronics and Nanometer Structures Processing, Measurement, and Phenomena*, vol. 18, no. 3, pp. 1785–1791, 2000.

[140] Y. T. Hou, M. F. Li, H. Y. Yu, and D. L. Kwong, "Modeling of Tunneling Currents Through HfO_2 and $(HfO_2)_x(Al_2O_3)_{1-x}$ Gate Stacks," *IEEE Electron Device Letters*, vol. 24, no. 2, pp. 96–98, 2003.

[141] S. Spiga, G. Congedo, U. Russo, A. Lamperti, O. Salicio, F. Driussi, and E. Vianello, "Experimental and Simulation Study of the Program Efficiency of HfO_2 Based Charge Trapping Memories," *Proceedings of the European Solid State Device Research Conference (ESSDERC)*, pp. 408–411, 2010.

[142] V. G. Kravets, "Polaron Interpretation of the Magnetoreflectance Effect in Insulating α–Al_2O_3," *Physical Review B*, vol. 72, p. 064303, 2005.

[143] F. Driussi, S. Marcuzzi, P. Palestri, and L. Selmi, "Gate Current in Stacked Dielectrics for Advanced FLASH EEPROM Cells," *Proceedings of European Solid–State Device Research Conference (ESSDERC)*, pp. 317–320, 2005.

[144] B. Govoreanu, P. Blomme, M. Rosmeulen, J. V. Houdt, and K. D. Meyer, "VARIOT: A Novel Multilayer Tunnel Barrier Concept for Low–Voltage Nonvolatile Memory Devices," *IEEE Electron Device Letters*, vol. 24, no. 2, pp. 99–101, 2003.

[145] G. Lupina, J. Kitzmann, M. Lukosius, J. Dabrowski, A. Wolff, and W. Mehr, "Deposition of Thin Silicon Layers on Transferred Large Area Graphene," *Applied Physics Letters*, vol. 103, no. 26, p. 263101, 2013.

[146] E. Dentoni Litta, P. E. Hellström, C. Henkel, and M. Östling, "Thulium Silicate Interfacial Layer for Scalable High–k/Metal Gate Stacks," *IEEE Transactions on Electron Devices*, vol. 60, no. 10, pp. 3271–3276, 2013.

[147] F. Driussi, S. Spiga, A. Lamperti, G. Congedo, and A. Gambi, "Simulation Study of the Trapping Properties of HfO_2–Based Charge–Trap Memory Cells," *IEEE Transactions on Electron Devices*, vol. 61, no. 6, pp. 2056–2063, 2014.

[148] F. Driussi, R. Iob, D. Esseni, L. Selmi, R. van Schaijk, and F. Widdershoven, "Investigation of the Energy Distribution of Stress–Induced Oxide Traps by Numerical Analysis of the TAT of HEs," *IEEE Transactions on Electron Devices*, vol. 51, no. 10, pp. 1570–1576, 2004.

[149] M. Lundstrom, "Fundamentals of Carrier Transport," *Cambrige University Press*, 2000.

[150] A. Hamad, L. Li, Z. Liu, X. L. Zhong, and T. Wang, "Picosecond Laser Generation of Ag–TiO_2 Nanoparticles with Reduced Energy Gap by Ablation in Ice Water and their Antibacterial Activities," *Applied Physics A*, vol. 119, no. 4, pp. 1387–1396, 2015.

[151] H. Tang, K. Prasad, R. Sanjinès, P. E. Schmid, and F. Lévy, "Electrical and Optical Properties of TiO_2 Anatase Thin Films," *Journal of Applied Physics*, vol. 75, no. 4, pp. 2042–2047, 1994.

[152] S. A. Campbell, D. C. Gilmer, X.-C. Wang, M.-T. Hsieh, H.-S. Kim, W. L. Gladfelter, and J. Yan, "MOSFET Transistors Fabricated with High Permitivity TiO_2 Dielectrics," *IEEE Transactions on Electron Devices*, vol. 44, no. 1, pp. 104–109, 1997.

[153] G. Lupina, C. Strobel, J. Dabrowski, G. Lippert, J. Kitzmann, H. M. Krause, C. Wenger, M. Lukosius, A. Wolff, M. Albert, and J. W. Bartha, "Plasma–Enhanced Chemical Vapor Deposition of Amorphous Si on Graphene," *Applied Physics Letters*, vol. 108, no. 19, p. 193105, 2016.

[154] C. M. Torres, Y.-W. Lan, C. Zeng, J.-H. Chen, X. Kou, A. Navabi, J. Tang, M. Montazeri, J. R. Adleman, M. B. Lerner, Y.-L. Zhong, L.-J. Li, C.-D. Chen, and K. L. Wang, "High–Current Gain Two–Dimensional MoS_2–Base Hot–Electron Transistors," *Nano Letters*, vol. 15, no. 12, pp. 7905–7912, 2015.

[155] R. J. Gonzalez and R. Zallen, "Infrared Reflectivity and Lattice Fundamentals in Anatase TiO_2," *Physical Review B*, vol. 55, pp. 7014–7017, 1997.

[156] S. Venica, F. Driussi, P. Palestri, and L. Selmi, "Backscattering and Common–Base Current Gain of the Graphene Base Transistor (GBT)," *Microelectronic Engineering*, vol. 147, pp. 192–195, 2015.

[157] G. Hassink, R. Wanke, I. Rastegar, W. Braun, C. Stephanos, P. Herlinger, J. H. Smet, and J. Mannhart, "Transparency of Graphene for Low–Energy Electrons Measured in a Vacuum–Triode Setup," *APL Materials*, vol. 3, no. 7, p. 076106, 2015.

[158] B. Heinemann, H. Rücker, R. Barth, F. Bärwolf, J. Drews, G. G. Fischer, A. Fox, O. Fursenko, T. Grabolla, F. Herzel, J. Katzer, J. Korn, A. Krüger, P. Kulse, T. Lenke, M. Lisker, S. Marschmeyer, A. Scheit, D. Schmidt, J. Schmidt, M. A. Schubert, A. Trusch, C. Wipf, and D. Wolansky, "SiGe HBT with f_x/f_{max} of 505 GHz/720 GHz," *IEEE International Electron Devices Meeting (IEDM), Technical Digest*, pp. 3.1.1–3.1.4, 2016.

[159] M. Urteaga, J. Hacker, Z. Griffith, A. Young, R. Pierson, P. Rowell, M. Seo, and M. J. W. Rodwell, "A 130 nm InP HBT Integrated Circuit Technology for THz Electronics," *IEEE International Electron Devices Meeting (IEDM), Technical Digest*, pp. 29.2.1–29.2.4, 2016.

[160] G. Fiori, F. Bonaccorso, G. Iannaccone, T. Palacios, D. Neumaier, A. Seabaugh, S. K. Banerjee, and L. Colombo, "Electronics Based on Two–Dimensional Materials," *Nature Nanotechnology*, vol. 9, pp. 768–779, 2014.

[161] F. Schwierz, J. Pezoldt, and R. Granzner, "Two–Dimensional Materials and Their Prospects in Transistor Electronics," *Nanoscale*, vol. 7, pp. 8261–8283, 2015.

[162] Z. Geng, W. Kinberger, R. Granzner, J. Pezoldt, and F. Schwierz, "2d Electronics – Opportunities and Limitations," *Proceedings of the European Solid–State Device Research Conference (ESSDERC)*, pp. 230–235, 2016.

Publications of the Author

Publications on International Journals

- S. Venica, F. Driussi, P. Palestri, D. Esseni, S. Vaziri and L. Selmi, "**Simulation of DC and RF Performance of the Graphene Base Transistor**", in *IEEE Transactions on Electron Devices*, vol. 61, no. 7, pp. 2570–2576, July 2014.

  Abstract - We examined the DC and RF performance of the graphene base transistor (GBT) in the ideal limit of unity common base current gain. To this purpose, we developed a model to calculate the current-voltage characteristics of GBTs with semiconductor or metal emitter taking into account space charge effects in the emitter-base and base-collector dielectrics that distort the potential profile and limit the upper value of f_T. Model predictions are compared with available experiments. We show that, in spite of space charge high current effects, optimized GBT designs still hold the promise to achieve intrinsic cutoff frequency in the terahertz region, provided that an appropriate set of dielectric and emitter materials is chosen.

- S. Venica, F. Driussi, P. Palestri and L. Selmi "**Backscattering and Common–Base Current Gain of the Graphene Base Transistor (GBT)**", in *Microelectronic Engineering*, vol. 147, pp. 192–195, November 2015.

  Abstract - In this paper, we investigate electron transport and electron scattering in the insulators of the Graphene Base Transistor (GBT) by means of a Monte Carlo transport model. We focus on electron backscattering in the base-collector insulator as the possible root cause of the large experimental base current and small measured common-base current gain (α_F) of GBTs. Different GBT structures have been simulated and the impact of the scattering parameters on the base current is analyzed. Simulated backscattering–limited α_F values are found to be much higher than available experimental data, suggesting that state-of-the-art technology is still far from being optimized. However, those simulated α_F values can be low enough to limit the maximum achievable GBT performance.

- S. Vaziri, A. D. Smith, M. Östling, G. Lupina, J. Dabrowski, G. Lippert, W. Mehr, F. Driussi, S. Venica, V. Di Lecce, A. Gnudi, M. König, G. Ruhl, M. Belete and M. C. Lemme, "**Going Ballistic: Graphene Hot Electron Transistors**", *Solid State Communications*, vol. 224, pp. 64–75, December 2015.

  Abstract - This paper reviews the experimental and theoretical state of the art in ballistic hot electron transistors that utilize two-dimensional base contacts made from graphene, i.e. graphene base transistors (GBTs). Early performance predictions that indicated potential for THz operation still hold true today, even with improved models that take non–idealities into account. Experimental results clearly demonstrate the basic functionality, with on/off

current switching over several orders of magnitude, but further developments are required to exploit the full potential of the GBT device family. In particular, interfaces between graphene and semiconductors or dielectrics are far from perfect and thus limit experimental device integrity, reliability and performance.

- S. Frégonèse, S. Venica, F. Driussi and T. Zimmer, "**Electrical Compact Modeling of Graphene Base Transistors**", in *Electronics*, vol. 4, no. 4, p. 969, 2015.

  Abstract - Following the recent development of the Graphene Base Transistor (GBT), a new electrical compact model for GBT devices is proposed. The transistor model includes the quantum capacitance model to obtain a self-consistent base potential. It also uses a versatile transfer current equation to be compatible with the different possible GBT configurations and it account for high injection conditions thanks to a transit time based charge model. Finally, the developed large signal model has been implemented in Verilog–A code and can be used for simulation in a standard circuit design environment such as Cadence or ADS. This model has been verified using advanced numerical simulation.

- Venica S. F. Driussi, S. Vaziri, P. Palestri and L. Selmi, "**Graphene Base Transistor with Bilayer Tunnel Barriers: Performance Evaluation and Design Guidelines**", in *IEEE Transactions on Electron Devices*, vol. 64, no. 2, pp. 593–598, February 2017.

  Abstract - Graphene based capacitors and Graphene base transistors (GBT) featuring innovative engineered tunnel barriers are characterized in DC and the data are thoroughly analyzed by means of an electrical model and a Monte Carlo transport simulator. Following model calibration on experiments, we then propose strategies to improve the DC common-base current gain and the cutoff frequency of GBTs. The DC and RF performance of optimized GBT structures based on realistic technology data are analyzed in detail to highlight advantages and potential limits of this device concept.

Publications on International Conferences

- S. Venica, F. Driussi, P. Palestri and L. Selmi, "**Graphene Base Transistors with Optimized Emitter and Dielectrics**", *International Convention on Information and Communication Technology, Electronics and Microelectronics (MIPRO)*, pp. 33–38, 2014.

  Abstract - The Graphene Base Transistor (GBT) is a very promising device concept for analog applications. The device operates similar to the hot electron transistor and exploits the high carrier mobility of graphene to reduce the base resistance that limits the unity power gain frequency (f_{max}) and the noise figure (NF) of RF devices. Although the DC functionality of the GBT has been experimentally demonstrated, at present RF performance can be investigated by simulations only. In this paper, we predict the DC current and the cutoff frequency of different GBT designs (including dimensions and various materials), with the aim to optimize the GBT structure and to achieve THz operation. In particular, optimized emitter/dielectrics combinations are proposed to maximize RF figures of merit.

- S. Venica, F. Driussi, P. Palestri and L. Selmi, "**Backscattering and Common–Base Current Gain of the Graphene Base Transistor (GBT)**", *Book of Abstract of Insulating Films on Semiconductors (INFOS)*, pp. 229–230, 2015.

Abstract - In this paper, we investigate electron transport and backscattering in the EBI and BCI as possible root causes of the base current and of the common–base current gain degradation in GBTs by means of a Monte Carlo (MC) transport model. Backscattering limited α_F values are found to be much higher than experiments, suggesting that state–of–the–art technology is still far from being optimized, but they are low enough to limit the maximum achievable performance.

- P. Palestri, E. Caruso, F. Driussi, D. Esseni, D. Lizzit, P. Osgnach, S. Venica and L. Selmi, "**State–of–the–Art Semi–Classical Monte Carlo Method for Carrier Transport in Nanoscale Transistors**", *International Convention on Information and Communication Technology, Electronics and Microelectronics (MIPRO)*, pp. 1–8, 2015.

  Abstract - We review the Monte Carlo method to model semi-classical carrier transport in advanced semiconductor devices. We report examples of the use of the Multi–Subband Monte Carlo method to simulate MOSFETs with III–V compound semiconductor channel. Monte Carlo transport modeling of graphene–based transistors is also addressed.

- S. Venica, M. Zanato, F. Driussi, P. Palestri and L. Selmi, "**Modeling Electrostatic Doping and Series Resistance in Graphene–FETs**", *Proceedings of International Conference on Simulation of Semiconductor Processes and Devices (SISPAD)*, pp. 357–360, 2016.

  Abstract - We model the source/drain series resistance and the electrostatic doping effects associated to the source and drain metals in graphene FETs using a Monte Carlo transport simulator. We compare the new model to simulations assuming chemical doping in the source/drain regions. A procedure to include the series resistance as part of the self-consistent Monte Carlo loop is proposed and verified against the widely employed method based on look–up tables.

- S. Venica, F. Driussi, P. Palestri, L. Selmi, A. Gahoi, V. Passi and M. C. Lemme, "**Detailed Characterization and Critical Discussion of Series Resistance in Graphene-Metal Contacts**", accepted for *International Conference on Microelectronic Test Structures (ICMTS) 2017*.

  Abstract - The contact-end resistance method is applied to TLM measurements to characterize the graphene-metal contact resistance. The experiments show that the commonly used transmission line model fails to describe the graphene-metal contact under specific biasing. This is due to the additional resistance of the junction induced in graphene near the contact.